Recalibration of the MEPED Proton Detectors Onboard NOAA POES Satellites

Master Thesis in Space Physics

by

Linn-Kristine Glesnes Ødegaard

May, 2013

Department of Physics and Technology

University of Bergen Norway

Abstract

In this thesis we have calibrated energetic proton data from the solid state detectors of the MEPED instrument onboard the satellites NOAA 15, 16, 17, 18, and MetOp 02. All these satellites are part of the NOAA/POES program, they fly in polar orbits in 800-850 km altitude, and they carry a suite of almost identical instrumentation. For over 30 years the NOAA/POES satellites have collected valuable information about the particle environment in the Earth's magnetosphere and ionosphere. However, with time these solid state detectors suffer from radiation damage due to energetic particles, which leads to increasing energy thresholds and increasing underestimation of particle fluxes. Data from different satellites must therefore be inter-calibrated in order to be used for quantitative studies. In this thesis we have developed two statistical methods for calibration of the energetic proton data from MEPED instrument onboard the NOAA satellites. The first method is used for calibration when two spacecraft are in the same magnetic local time sector. This method is applied to data from NOAA 16 in 2005, NOAA 17 in 2007, and NOAA 18 in 2009, when these satellites were fortunate to share the orbit with a newly launched satellite. We compare energy spectra based on daily averaged fluxes and estimate the increased energy thresholds of the MEPED instrument in these years. The second method is used to calibrate satellite data at different magnetic local times. Average maps of the flux of energetic protons as a function of magnetic local time and invariant latitude were constructed for different levels of magnetic activity given by the Kp index. By determining the local time dependence of the fluxes in the isotropic zone, these maps were used to calibrate old satellites that were separated in magnetic local time relative to new satellites. This method allows for a better estimation of the temporal evolution of the energy thresholds of the MEPED instruments.

Acknowledgements

I would like to thank my supervisor Kjellmar Oksavik for the opportunity to work on this master project. He has always shown great interest in my work, and his guidance and support has been much appreciated. I would also like to thank Finn Søraas, Hilde Nesse Tyssøy, Johan Stadsnes and Nikolai Østgaard for helpful discussions and support.

The time as a master student would not have been the same without all the people in the Space Physics group in Bergen. When sharing office with Paul, Alexander, Jone, Tonje, Hulda, Christer, Annet Ewa, Lindis and Christine, every day is a an opportunity to wear party-hats. I owe Paul an extra thanks for making me realize that Space Physics was the way to go. I thank him also for teaching me MATLAB, helping me out with LaTeX, proofreading, and lots of cups of coffee. Alexander, thank you for sharing my really bad sense of humor. Tonje and Hulda, thank you for the office exercises, for the long lunches, and for lots of fun. I also want to thank my friends, especially Yngve for proofreading, and Sondre for programming help and support. Last, Mammo and my brothers deserve an extra large thanks for always supporting and believing in me.

For the data used in this thesis I acknowledge:
The Space Physics Data Facility CDAWeb providing the Dst and Kp index data
NOAA's National Geophysical Data Center (NGDC) for providing the NOAA particle data

Linn-Kristine Glesnes Ødegaard
Bergen, May 2013

Table of Contents

Chapter 1

Introduction

In the scientific community there is debate about the role of varying solar activity for climate on Earth [*Lockwood et al.*, 1999]. *Carrington* [1859] was one of the first to connect activity on the Sun with magnetic disturbance and aurora on the Earth. Since then a lot of effort has been put into monitoring the activity on the Sun (e.g. SOHO [*Domingo et al.*, 1995; *Fleck et al.*, 2006]), the solar wind (e.g ACE and WIND [*Stone et al.*, 1998; *Harten and Clark*, 1995]) and the magnetosphere-ionosphere system (e.g. Cluster [*Escoubet et al.*, 1997]).

However, a challenge for understanding the long-term effects in the atmosphere is the long-term variability in the Earth's radiation belts and the radiation environment that spacecrafts are exposed to [*Bourdarie and Xapsos*, 2008; *Li et al.*, 2001; *Miyoshi et al.*, 2000]. The NOAA POES spacecraft carry instruments for measuring energetic particles in the near-Earth environment [*Evans and Greer*, 2004]. The data set consists of measurements that could be useful for research on long-term variabilities in the radiation belts and ultimately their potential effects on climate. A substantial challenge is that the proton detectors are impaired by the very particles they measure, and the energy thresholds of the instruments increase with time. This leads to an underestimate of both the particle energy and flux with time.

NOAA POES is unique because several satellites with almost identical instrumentation have orbited the Earth in the same manner for 35 years [*Davis*, 2007; *Evans and Greer*, 2004; *Raben et al.*, 1995]. This opens for the possibility to recalibrate degraded particle detectors onboard older satellites by comparing the damaged detector to a healthy detector on a new satellite. *Asikainen and Mursula* [2011] made an attempt at presenting quantified estimates of the degree of radiation damage for all NOAA POES satellites. Their method involved identifying conjunctions between two orbiting satellites, one of which was less than 5 months old, and comparing the integral flux of the new satellite with the integral flux of the older satellite.

The criteria *Asikainen and Mursula* [2011] used for choosing satellite conjunctions are rather strict and the identified conjunctions are few, which limit the usable data to a small fraction of the total available data. Half way through this thesis project, *Asikainen et al.* [2012] published an article using a statistical approach to improve results obtained

by *Asikainen and Mursula* [2011]. However, the statistical approach was only used on two of the 14 existing NOAA satellites.

The degradation of the particle detectors is dependent on the level of radiation the detector is exposed to. The flux of particles decreases with increasing energy, and the lower energy channels are expected to degrade faster than the higher energy channels of the detector. The results presented by *Asikainen and Mursula* [2011] and *Asikainen et al.* [2012] do not meet these expectations. This was the motivation for developing an alternative method for calibration of the NOAA POES proton data.

The objective of this thesis is therefore to develop a statistical method for calibration of the MEPED proton detectors onboard NOAA 15, 16, 17, 18, and MetOp 02. Our goal is to use a larger part of the NOAA dataset, and in this way determine the degradation of the detectors more robustly.

The thesis is organized as follows: Chapter 2 gives an overview of relevant space physics theory. Chapter 3 gives an introduction to the NOAA instrumentation and data. A brief description of the MEPED instrument is given, and solid-state detectors and degradation are discussed. Chapter 4 presents previous work on calibration of the NOAA satellites, and a method for calibration of satellites that fly in the same MLT sector. The method will be applied to data from NOAA satellites, and the results are presented and discussed. Finally, we present a method for calibration using a satellite located at a different MLT. The method is applied to data, and the results will be discussed. In Chapter 5 we discuss our results in comparison to previous work. Summary and conclusion follows in Chapter 6, and Chapter 7 lists ideas for future work.

Chapter 2

Background and Theory

The goal of this thesis is to develop a method that can be used to calibrate the polar orbiting NOAA satellites. In this chapter we will introduce theory to get an understanding of the environment that the NOAA satellites operate in. To understand the radiation environment on Earth, we need to start with the Sun. The Sun is central in space physics because it drives all the dynamics observed in the near Earth space. We will therefore first give a short introduction on how energy is produced in the Sun. Next, we will discuss some mechanisms that transports energy away form the Sun. This includes different types of solar eruptions, and the never-ending stream called the solar wind. To better understand how the solar wind interacts with the Earth, we present theory on the Earth's magnetic field. We then discuss the effects of the solar wind interaction with the magnetosphere. Finally, we move down to satellite altitude to look at particle precipitation regions in the high-latitude ionosphere.

2.1 The Sun and Solar Activity

A simple overview of the structure of the Sun and the energy transportation inside the Sun will be given in this section. Sunspots and their relationship with the solar cycle is introduced, and the most important forms of solar activity are presented.

2.1.1 The Sun

The Sun is the Earth's ultimate energy source and it drives all dynamics in the near Earth space. The energy produced in the Sun's core is a result of fusion processes, and the released energy is transported outward as radiation. The layer inside the Sun where the energy transport is mainly carried by radiation is called the radiative zone. As photons are absorbed and re-emitted, they loose energy, and wavelengths decrease from gamma radiation down to the visible wavelengths we see when we look at the Sun's surface. The layers closer to the surface of the Sun are dominated by convective heat transport, and is thus called the convection zone. In the convection zone, warm plasma elements rise upward and cold plasma elements sink. The phenomenon is often referred

to as the "boiling" on the surface of the Sun. The convective motion of the plasma is also what creates the Sun's magnetic field [*Yoshimura*, 2000; *Priest*, 1995].

Figure 2.1 is an illustration of our Sun. The figure shows the inner core, the radiative zone and the convection zone which makes up most of the Sun's volume. The top of the convection zone is called the photosphere and is the region where sunspots are visible as black areas in white light images. At greater altitudes the chromosphere can be revealed by the use of camera filters. The outermost layer of the Sun, the corona, can be viewed in white-light if the solar disk is blocked out. X-ray images of the corona has among other things revealed coronal holes. Here, the Sun's magnetic field is open and solar wind can flow freely out into the interplanetary medium [*Webb*, 2000; *Heber et al.*, 1999; *Axford*, 1985]. Bright areas in the chromosphere are called "active regions" and are found in the vicinity of sunspots in the photosphere [*Priest*, 1995]. Prominences are thin plasma structures that rise above the chromosphere. As sunspots, they look darker than their surroundings because they have much lower temperatures [*Mackay et al.*, 2010].

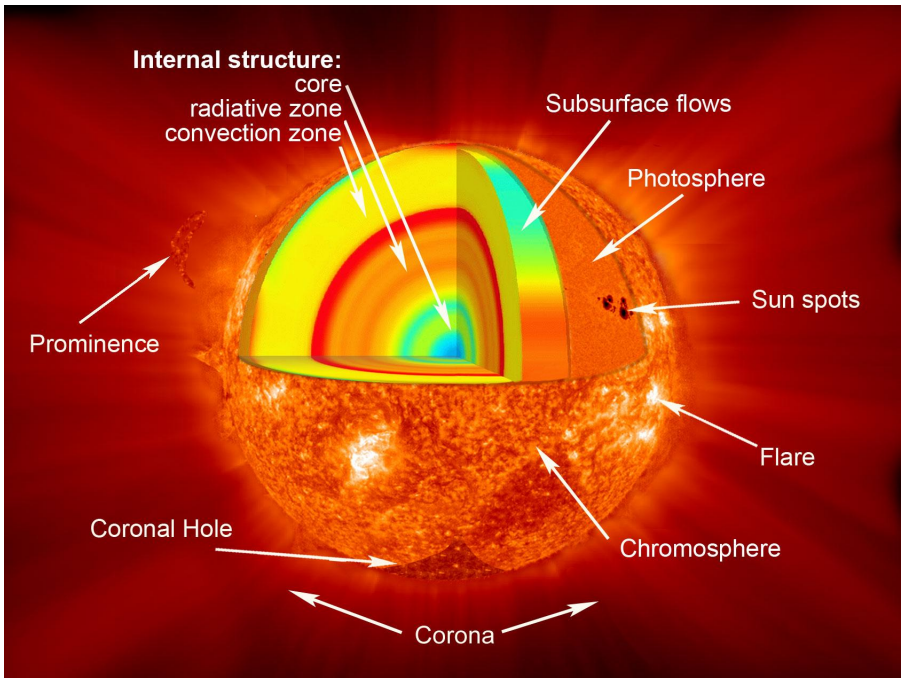

Figure 2.1: Illustration of the layers of the Sun. See text for a description [`http://www.nasa.gov/topics/solarsystem/sunearthsystem/main/Helio-facts.html`].

2.1.2 Sunspots

In the late 16th and early 17th century, Galileo Galilei was one of the first to study sunspots and their movement across the Sun's surface. Since then, it has been established that the number of sunspots increase and decrease on an irregular cycle of 11 years.

The formation of sunspots is connected to the emerging of magnetic flux tubes through the solar surface. The magnetic flux inhibits convection, and when heat is prevented from rising to the surface, the spot will get colder than its surroundings and look darker. Sunspots are 1000-1900 K colder than the quiet sun. They vary in size from 2500-60000 km in diameter and can exist from hours to months. Other forms of solar activity also exhibit a periodic fluctuation between minimum and maximum, and the 11 year cycle seems to be fundamental to our Sun [*Kane*, 2006; *Solanki*, 2003; *Stix*, 2002; *Ruzmaikin*, 2001; *Yoshimura*, 2000; *Feminella and Storini*, 1997; *Priest*, 1995; *Berry*, 1987].

The annual mean number of sunspots is shown is Figure 2.2. The 11-year cycle in activity is evident. However, there is also a significant variability from cycle to cycle. For example, the maximum number of sunspots was low around 1800, and large around 1960.

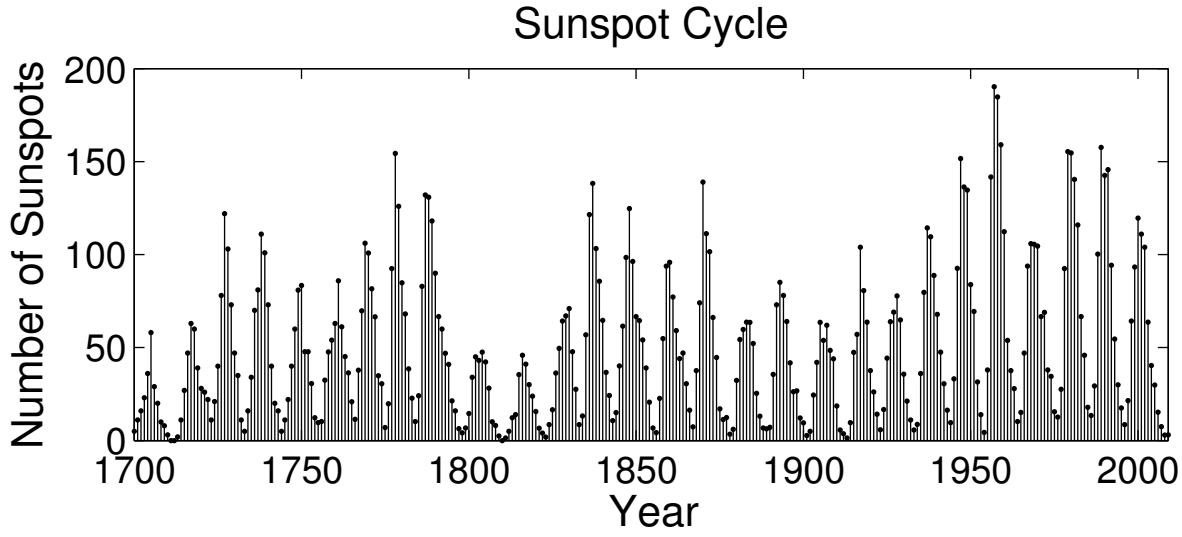

Figure 2.2: The yearly mean number of sunspots from 1700 to 2009 (data obtained from [`http://www.ngdc.noaa.gov/nndc/struts/results?t=102827&s=5&d=8,430,9`]).

2.1.3 Solar Eruptions

In addition to the steady radiation and flow of solar wind from the Sun, violent eruptions also occur. Two types of eruptions, called solar flares and coronal mass ejections (CME), are both major sources of geomagnetic activity.

A solar flare can be observed as an intense, short-lived brightening of active regions on the sun. In a flare the released electromagnetic radiation is many times larger than normal levels from the quiet Sun. Particles are heated and accelerated in the eruption [*Schrijver*, 2009; *Priest*, 1995; *Gosling*, 1993].

A coronal mass ejection is a sudden release of large amounts of mass and magnetic

fields into the heliosphere [*Webb*, 2000]. An image of a large CME caught by the SOHO satellite is shown in Figure 2.3. The SOHO satellite carries several instruments designed for monitoring the Sun. The image in Figure 2.3 was registered on a coronagraph. The large CME that was flung into the interplanetary space on 04 November 2003 is clearly visible to the right in the image. To be able to study the solar corona and CME's, the solar disk is blocked from the view of the coronagraph.

The connection between CMEs and solar flares is still a widely discussed and unsolved topic of solar physics (see e.g. *Gosling* [1993] and *Hudson et al.* [1995]). One of the fundamental questions is what triggers eruptions from the Sun. A review on the driving of solar eruptions by *Schrijver* [2009] claims that both solar flares and CMEs can be observed following an unstable configuration of the coronal magnetic field. Several factors determine what such an unstable magnetic configuration evolve into; the scale of the structure, the available energy, and the twist of the magnetic field.

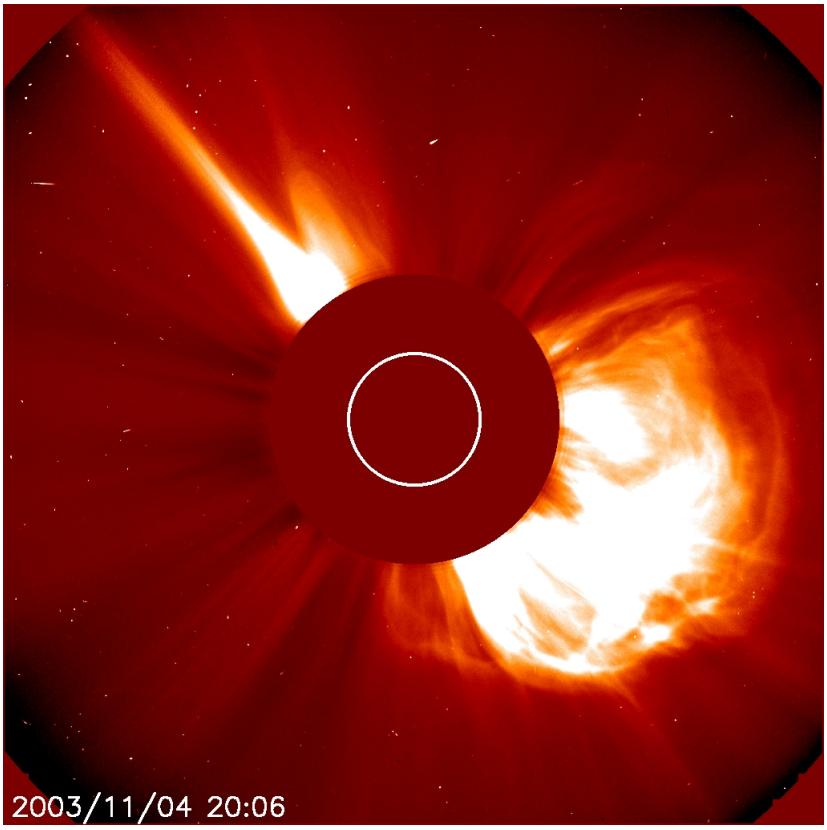

Figure 2.3: An image from the satellite SOHO showing a huge CME on 04 November 2003 [`http://sohowww.nascom.nasa.gov/hotshots/2003_11_04/`]

2.2 The Solar Wind

We have now briefly discussed how the Sun produces energy, and how solar eruptions suddenly fling large amounts of radiation and mass into interplanetary space. However, there is always a steady flow of highly conducting plasma from the Sun. This plasma is what we call the solar wind, and it consists mainly of an equal amount of electrons and Hydrogen ions, and a small fraction of heavier ions. An important characteristic of the solar wind is that it carries the magnetic field of the Sun as it propagates. The frozen-in magnetic field in the solar wind is called the Interplanetary Magnetic Field (IMF). Near Earth the average solar wind speed is approximately 450 km/s [*Hundhausen*, 1995]. The solar wind speed is divided in two categories, slow (approximately 300-500 km/s) and fast (approximately 600-800 km/s). The fast solar wind flows from coronal holes, while the slow solar wind is an extension of the solar corona into interplanetary space [*Breen et al.*, 1997; *Balogh et al.*, 1999; *Tsurutani et al.*, 2006; *Axford*, 1985]. Table 2.1 gives some typical solar wind parameters [*Ebert et al.*, 2009; *Balogh et al.*, 1999; *Axford*, 1985]. Compared to the fast solar wind, the slow solar wind is cooler and denser, while the magnetic field strength is approximately the same.

Table 2.1: Typical Solar Wind Parameters [*Ebert et al.*, 2009; *Balogh et al.*, 1999; *Axford*, 1985].

Type	V $[km/s]$	B [nT]	N_p [particles cm^{-3}]	Proton E_K [eV]
Slow	$\sim 300 - 500$	5	8	1000
Fast	$\sim 600 - 800$	4	3	4000

When the fast solar wind interacts with the slow solar wind, regions of intense magnetic field can be created. Such regions are called Corotating Interaction Regions (CIR). CIRs are also an important source of geomagnetic activity [*Balogh et al.*, 1999; *Heber et al.*, 1999; *Tsurutani et al.*, 2006; *Borovsky and Denton*, 2006].

2.3 The Earth's Magnetic field

We have established that the energy produced in the Sun is carried outwards by the solar wind and by solar eruptions. Fortunately for life on Earth, our planet is shielded from most of the dangerous radiation by a magnetic field. The rotational plasma motion of the Earth's liquid outer core induces electric currents, and is the dominating contributor to the magnetic field around the Earth [*Russell*, 1993a,b]. In this section we will first describe the terrestrial magnetic field close to the surface of the Earth by a dipole approximation. Based on this approximation, we introduce a magnetic coordinate system that will be used later in the thesis to describe the location of the NOAA satellites. We will also explain why the magnetic field in reality is not a perfect dipole a few earth radii from the surface of the Earth. Finally, we will address how particles group into regions within the magnetic field, and present some of these regions more closely.

Close to Earth, the terrestrial magnetic field can be approximated to a dipole field. The strength of a dipole magnetic field decreases as $1/r^3$, where r represents the radial distance from the center of the Earth. The field is strongest at the magnetic poles and weakest at the magnetic equator [*Russell*, 1993a; *Baumjohann and Treumann*, 1996]. Figure 2.4 illustrates the Earth surrounded by a dipole field. The distance between field lines indicates the strength of the field at a given distance from the center.

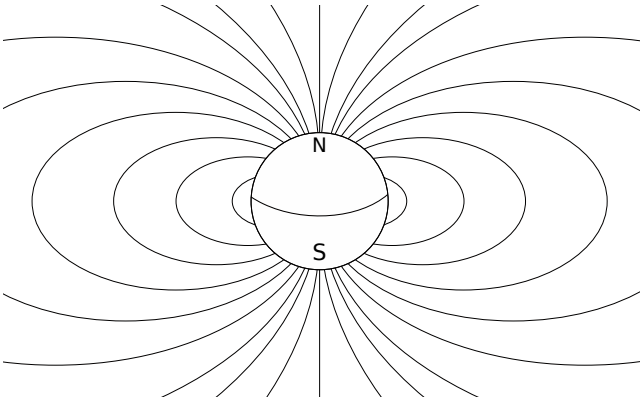

Figure 2.4: Illustration of the dipole magnetic field close to Earth. The direction of the magnetic field lines is out from the south pole and into the north pole.

When we measure the magnetic field on the surface of the Earth, we find that the dipole approximation holds fairly well. This is illustrated in Figure 2.5, which is a map of the measured field strength on Earth's surface[1]. The extra weak field strength seen above the South American continent is called the "South Atlantic Anomaly" (SAA) and is a consequence of the magnetic dipole axis being tilted relative to the Earth's spin axis [*Pinto et al.*, 1992].

[1] [`http://gravmag.ou.edu/mag_earth/mag_earth.html`]

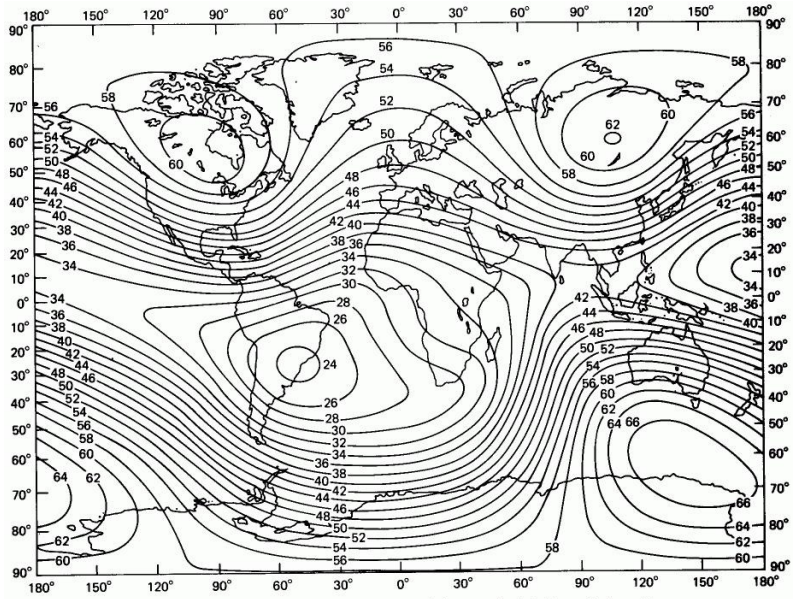

Figure 2.5: Map of the magnetic field strength at the Earth's surface (given in μT) [`http://gravmag.ou.edu/mag_earth/mag_earth.html`].

When we move further away from the Earth, the actual shape of the Earth's magnetic field is not dipolar. On the dayside, the magnetic field is compressed by the pressure of the solar wind. On the nightside is stretched towards a long tail-like configuration [*Russell*, 1986]. The magnetopause is the boundary separating the magnetic field frozen to the solar wind plasma from the Earth's magnetic field. The region within the magnetopause is called the magnetosphere. The magnetosphere is an efficient shield, and only $\sim 1\%$ of the available solar wind energy penetrates the boundary, while the rest is deflected [*Stern*, 1984]. The illustration in Figure 2.6 depicts a CME heading towards the Earth. The purple lines drawn around the Earth is a representation of the magnetic field. The shape is clearly compressed on the dayside and stretched on the nightside. The parabolic Shadow-like structure in front of the magnetosphere is the bow shock. The bow shock is a result of the interaction of the supersonic solar wind with the magnetosphere. The physics of plasma shocks can be reviewed in e.g. *Kivelson* [1995] and *Baumjohann and Treumann* [1996].

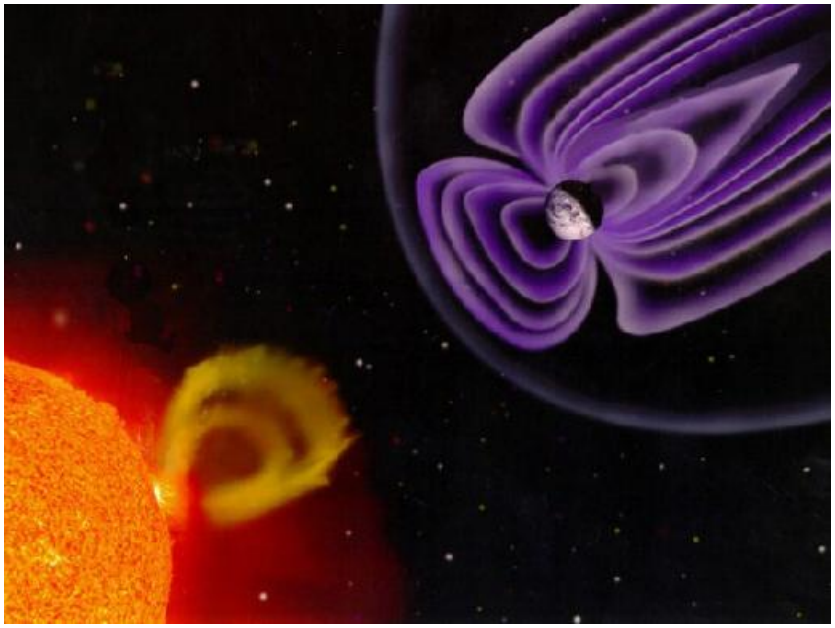

Figure 2.6: NASA illustration of the Sun and the Earth's magnetosphere [`http://www.nasa.gov/mission_pages/rbsp/multimedia/rbsp-coronalmass.html`]

2.3.1 Magnetic Coordinates

This thesis concerns satellites in orbit close to the Earth and well inside the dipolar magnetic field. It is therefore convenient to use a coordinate system that is fixed about the Earth's dipole moment. A point on a particular dipolar magnetic field line can be described in polar coordinates by an angle and the distance to the point. In Figure 2.7 this corresponds to the parameters λ and R. The parameter λ is called the Magnetic Latitude (MLAT), and is given by

$$\lambda = cos^{-1}\left(\sqrt{R/r_{eq}}\right) \tag{2.1}$$

where r_{eq} is the distance of the field line in the equatorial plane from the Earth's center.

The invariant Latitude (ILAT) Λ is the angle describing where a particular magnetic field line with a given r_{eq} will intersect the surface of Earth. The distance r_{eq} is commonly normalized by the Earth radii R_E. The resulting parameter is called the L-value of the magnetic field line, where $L = r_{eq}/R_E$. Λ is thus given by

$$\Lambda = cos^{-1}\left(\sqrt{1/L}\right) \tag{2.2}$$

As can be seen from Figure 2.7, in a dipole field approximation the invariant latitude equals the magnetic latitude on the surface of the Earth.

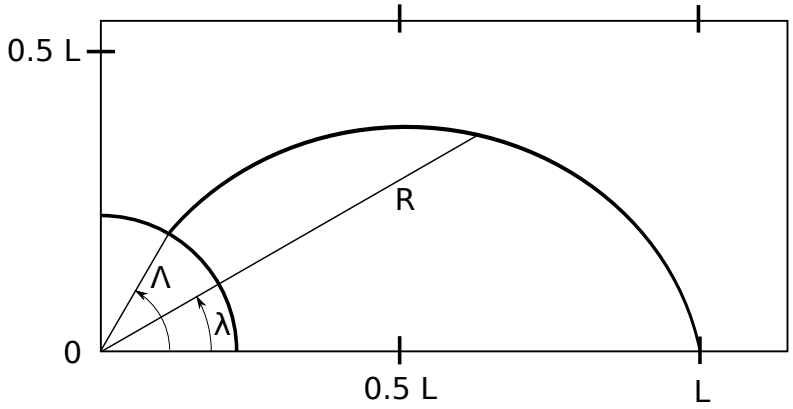

Figure 2.7: Illustration of magnetic and invariant latitude (adapted from *Kivelson* [1995]). This coordinate system is fixed about the dipole moment of the Earth.

Figure 2.8 illustrates another useful parameter called the Magnetic Local Time (MLT). The hemisphere is divided into meridians, and concentric circles that represent longitude. The Earth rotates under this coordinate system, and the geographical location of magnetic noon therefore changes through the day. Magnetic noon is always found where the universal time is noon.

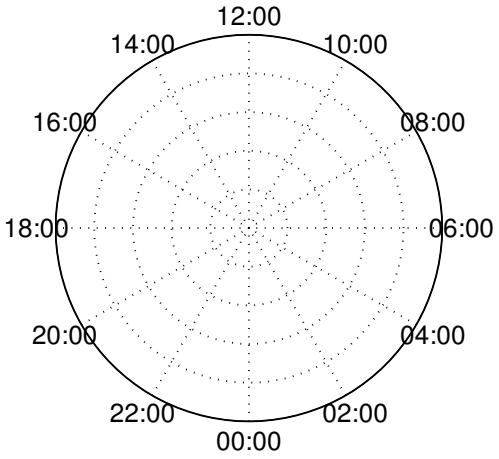

Figure 2.8: Magnetic local time grid in one hemisphere.

2.3.2 Regions Within the Magnetosphere

The magnetosphere is divided into regions based on characteristics of the particle populations found there. Figure 2.9 is an illustration featuring the most important regions.

We will not comment on all of the regions, but present the plasmasphere, the radiation belts, and the magnetotail.

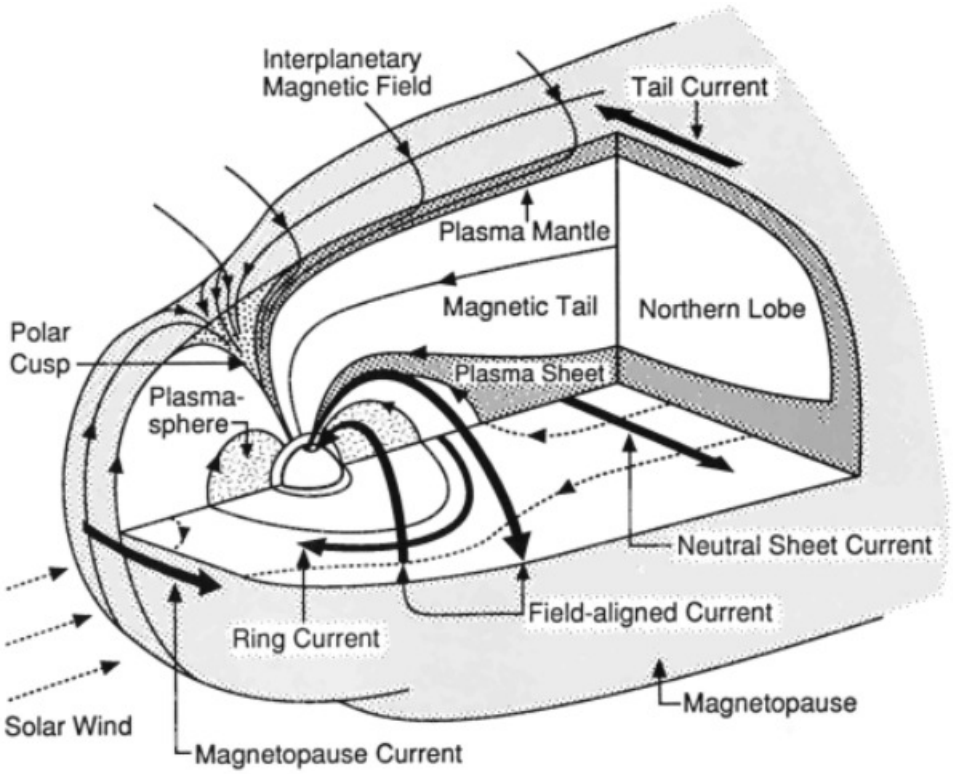

Figure 2.9: Illustration of Earth's magnetosphere with important particle populations and currents shown [*Russell*, 1993a].

The Plasmasphere

The plasmasphere consists of cold plasma with particle energies in the magnitude of electron volt (eV) and high densities ($\sim 10^3/cm^3$ [*Baumjohann and Treumann*, 1996]). The plasmaspheric environment is characterized by magnetic field lines that are nearly dipolar in shape, illustrated in Figures 2.9 and 2.10. Ions that flow out from the ionosphere at high latitudes are trapped in the magnetic field and bounce back and forth due to magnetic mirroring in the converging dipole field. The eastward rotation of the Earth contributes to the torus-like shape of the plasmasphere [*Ganguli et al.*, 2000; *Singh et al.*, 2010; *Chapell*, 1972; *Baumjohann and Treumann*, 1996].

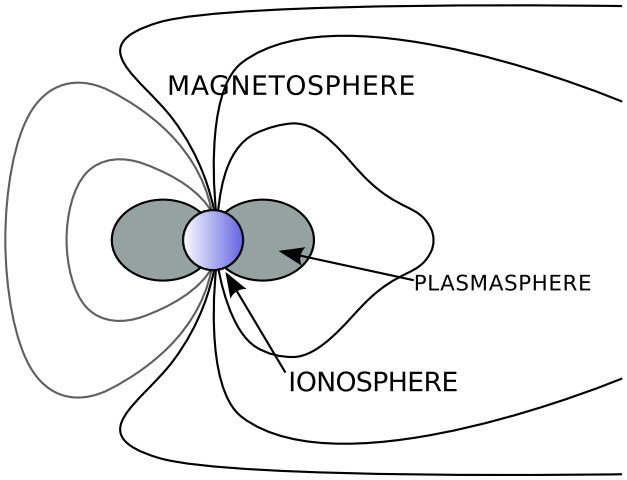

Figure 2.10: A closer look at the plasmasphere (adapted from *Chapell* [1972]).

The plasmapause is characterized by a sharp density gradient, and was first observed in work by *Gringauz* [1963] and *Carpenter* [1963]. The position of the plasmapause vary with MLT and magnetic activity. During quiet periods, the plasmapause can extend beyond geosynchronous orbit ($\sim$ 42000 km) near the equator, and when conditions are disturbed the boundary moves closer to Earth [*Pedatella and Larson*, 2010; *Darrouzet and De Keyser*, 2012]. *Doe et al.* [1992] found that the plasmapause could move from $L = 3$ to $L = 7$.

The Radiation Belts

Before 2013 it was believed that the Earth was surrounded by two radiation belts. Recent discoveries have shown that a third belt can exist [*Baker et al.*, 2013]. The third belt was discovered by the Van Allen probe, and was observed to be stable for more than 4 weeks.

The radiation belts coexists with the cold plasmasphere, and are found between altitudes of $\sim$ 700 km above the surface of the Earth and L-values of about 8 [*Van Allen*, 1966]. However, the region swells and shrinks in response to changes in solar wind.

A gap is found at $2.8 \leq L \geq 3.2$, separating the inner and outer radiation belts [*Tverskoy*, 1971]. The gap is formed due to instabilities that allow radiation to escape. The newly discovered third radiation belt was isolated from the inner and outer belts, observed at 3 to $\sim$ 3.5 Earth radii [*Baker et al.*, 2013].

The hot plasma in the radiation belts are trapped due to magnetic mirroring of charged particles in a converging magnetic field. The trapped particles will also drift across the magnetic field [*Daly*, 1994; *Baumjohann and Treumann*, 1996; *Kivelson*, 1995]. The result is a torus shaped volume [*Van Allen*, 1966]. The inner radiation

belt is often called the Van Allen belt to honor its discoverer, and contains both electrons and positive ions. The outer belt is mainly populated by electrons.

The electrons in the radiation belts can have energies up to MeV, protons can reach several hundreds of MeV [*Vette*, 1970; *Daly*, 1994; *Tverskaya*, 2010]. Particles with such high energies pose a great threat to instruments on board spacecrafts and humans on manned space missions. The Van Allen probe was launched by NASA to help increase our understanding of the mechanisms behind particle acceleration, and transport and loss inside the belts [*Baker et al.*, 2013].

The Magnetotail

Most of the plasma in the magnetotail is concentrated in the plasma sheet, which has a typical thickness of 6 R_E close to Earth [*Baumjohann and Paschmann*, 1990]. The magnetic field of the near Earth plasma sheet is connected to the ionosphere at high latitudes [*Hughes*, 1995; *Baumjohann and Treumann*, 1996]. In Figure 2.9 the plasma sheet is indicated, and the connection to the high-latitude ionosphere can also be seen.

The region above and below the plasma sheet contains a thin plasm, and is called the magnetotail lobes. The magnetic field in the tail lobes are open with one foot point in the solar wind and one in the region in the ionosphere called the polar cap [*McPherron*, 1995].

2.4 Magnetospheric Response to Varying Solar Wind Conditions

2.4.1 The Geomagnetic Storm

A geomagnetic storm is defined by *Gonzalez et al.* [1994] as

> "an interval of time when a sufficiently intense and long-lasting interplanetary convection electric field leads, trough a substantial energization in the magnetosphere-ionosphere system, to an intensified ring current sufficiently strong to exceed some key threshold of the quantifying storm time Dst index".

The geomagnetic storm is thus closely related to the ring current and the Dst index, which will be presented shortly.

During a storm, energy is transferred from the solar wind to the magnetosphere. The primary mechanism for energy transfer is called magnetic reconnection, or magnetic merging. Figure 2.11 illustrates the process.

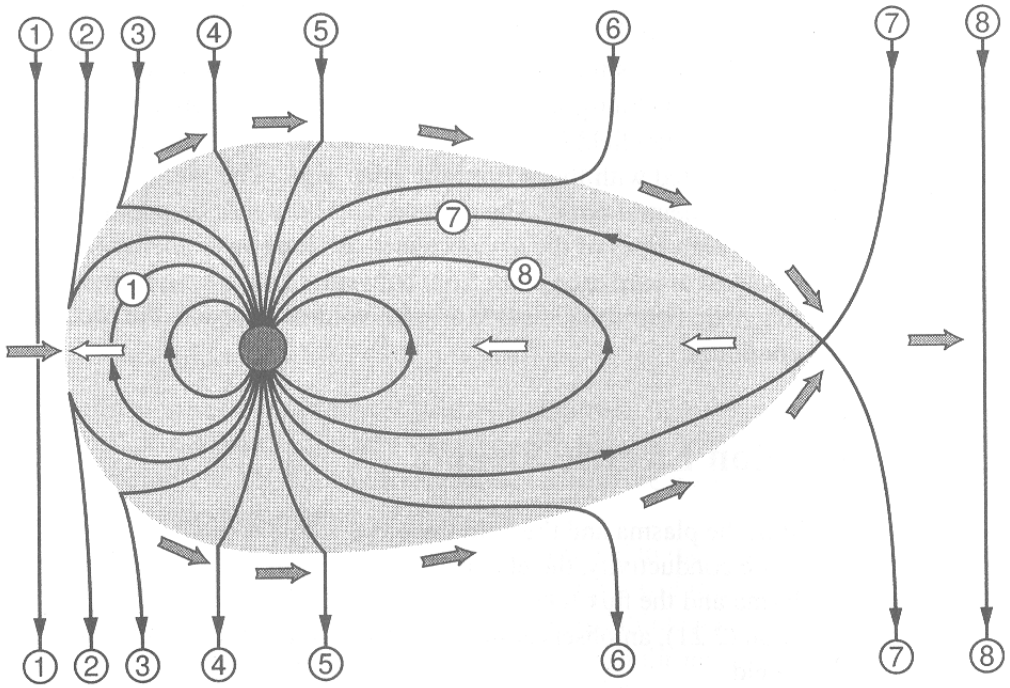

Figure 2.11: Magnetic flux transport in the Dungey cycle. 1) Reconnection, 2-6) Anti-sunward transport of field lines with the solar wind, 7) Nightside reconnection, and 8) Transport of reconnected flux sunward and anti-sunward [*Baumjohann and Treumann*, 1996].

In lose terms, reconnection is defined as a region where plasma from different field lines diffuse trough a neutral point where the magnetic strength is annihilated [*Baumjohann and Treumann*, 1996]. As a result of dayside reconnection energy is transferred from the solar wind to the magnetosphere system, and a newly opened field line undergoes the steps shown in Figure 2.11. This way of describing the reconnection process is often called the Dungey cycle. *Dungey* [1961] applied the theory of magnetic merging to the Earth's magnetosphere. He was one of the first to describe this idea of how the solar wind couples its energy to the magnetosphere, and how it drives the convection of magnetic flux within the magnetosphere.

The Ring Current and Activity Indexes

The ring current is usually found between 2-7 R_E, and is formed by ions and electrons with energies in the range between 10-300 keV [*Gonzalez et al.*, 1994]. The energetic ions drift westward and the electrons eastward in the geomagnetic field. This results in a net westward current. The ring current produces a measurable magnetic field at the Earth's surface which, due to the westward direction of the current, is directed opposite

of the terrestrial field. When the current is enhanced, the magnetic field depression at the Earth increases. During the main phase of a geomagnetic storm, magnetic flux and particles are released from the magnetotail. Particles are transported earthward where they are injected into the ring current. This phase of the storm can last from hours to days. Decay of the ring current is dependent on slower processes, e.g. charge exchange and Coulomb collisions, and the recovery phase can last for several days [*Chen et al.*, 1997; *Kamide et al.*, 1997; *McPherron*, 1997].

The Dst index is the most commonly used index to monitor the magnetic storm level. It is based on magnetometer measurements of the horizontal component of the magnetic field at four low-latitude observatories[2]. In Figure 2.12, these observatories are indicated by black dots spread out in longitude and lies close to, but not directly at, the magnetic equator. The placement is chosen to minimize the influence of other current systems, like auroral and equatorial electrojets. The Dst-index is derived as the average deviation of the H component of the magnetic field from the quiet day baseline. The magnetic latitude of the observatories are also taken into account [*McPherron*, 1997]. Recently, *Newell and Gjerloev* [2012] have proposed a more advanced index based on data from 98 mid and low latitude stations in the SuperMAG network. This index is divided into 4 sectors, to better describe the local time charactheristics of the ring current. However, we will use the Dst in this thesis.

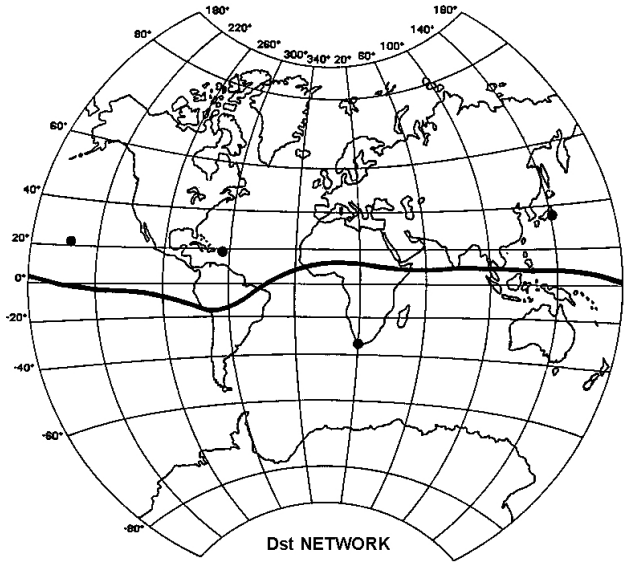

Figure 2.12: The Dst network [`http://wdc.kugi.kyoto-u.ac.jp/dstdir/dst2/onDstindex.html`]

Two distinct phases of a geomagnetic storm can clearly be seen in the Dst index; the main phase as a rapid decrease, and the recovery phase as a slower return back to

[2]Hermanus (South Africa), Kakioka (Japan), Honolulu (Hawaii) and San Juan (Puerto Rico)

normal levels. Panel a) of Figure 2.13 shows the Dst index for a geomagnetic storm in 2005 as an example. In panel b) another activity index called the Kp index is shown for the same period. The 3-hourly Kp index is derived by calculating the weighted average of the K-index from a network of geomagnetic observatories. The K-index is a number from 0-9 given to the maximum deviation of the horizontal component of the magnetic field from quiet day levels[3]. Kp$>$ 5 is classified as storm time [*Rangarajan and Iyemori*, 1997]. The Kp index will also be used in this thesis.

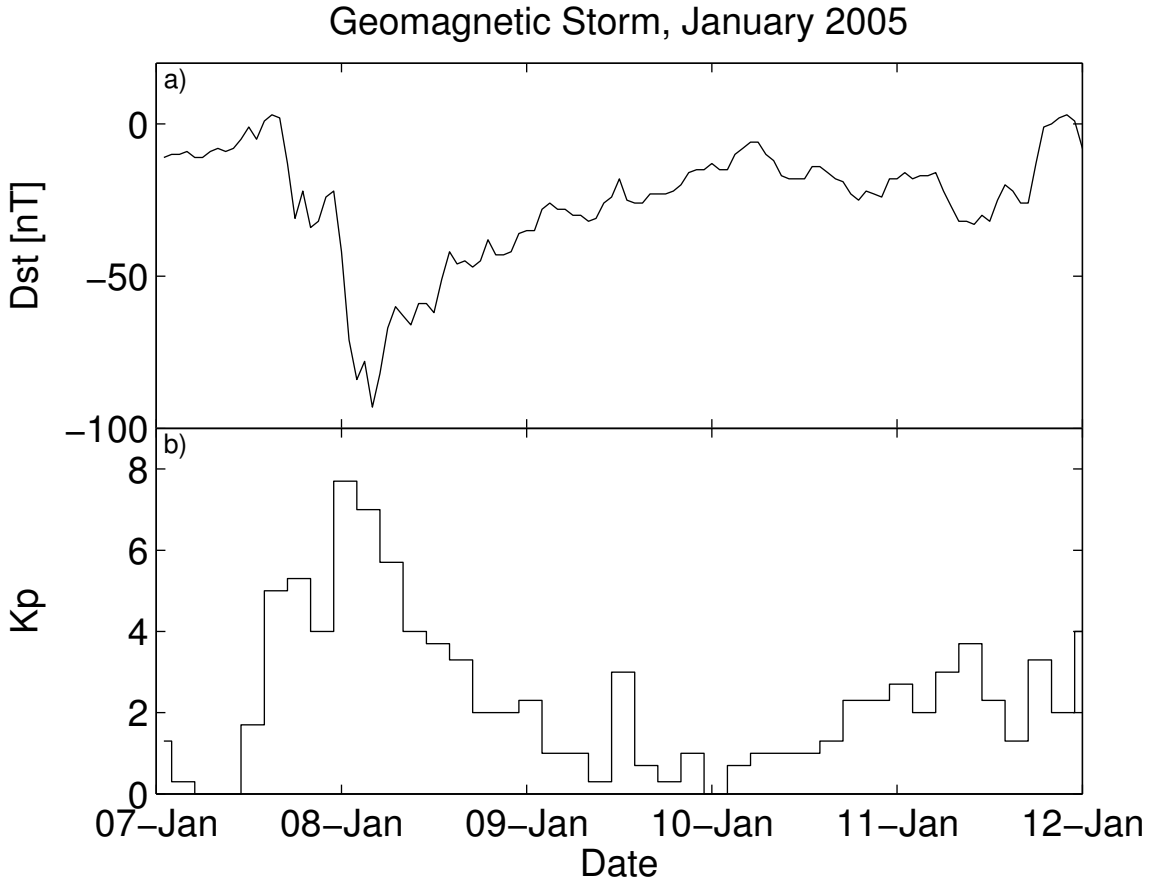

Figure 2.13: A geomagnetic storm in January 2005. a) The Dst drops from $\sim$ 0 nT to $\sim$ -100 nT late on 7 January 2005. The recovery back to quiet levels takes several days. b) The Kp index increases to $\sim$ 8 during the main phase of the storm.

[3][http://www.swpc.noaa.gov/info/Kindex.html]

2.4.2 Substorms

McPherron [1979] defines a substorm as a

> "transient process initiated on the night side of the earth, in which a significant amount of energy derived from the solar wind-magnetosphere interaction is deposited in the auroral ionosphere and magnetosphere".

A substorm is recognized by the increase in energy dissipation in the high-latitude ionosphere during a timescale of $\sim$ 1-3 hours [*Elphinstone*, 1996; *McPherron*, 1997]. Substorms can occur at any time, but are more frequent and stronger during the main phase of a storm. However, a correlation between decreasing Dst index and substorm onset does not seem to exist [*McPherron*, 1997].

2.5 The Ionosphere

The Earth's atmosphere is primarily comprised of neutral gas. Gravitation, and the magnetic field which shields the Earth from the solar wind keep the atmosphere in place. By early 1900 the postulation that the upper atmosphere was not neutral but partly ionized was made by several scientists [*Waynick*, 1974]. One indicator of ionization was that transmitted radio waves could be received beyond the horizon with higher intensities than expected from diffraction theory, meaning the radio waves were reflected in the atmosphere. Others speculated on the existence of electrical currents in the upper atmosphere, also implying ionization (e.g. [*Birkeland*, 1908]).

In 1924 and 1925 Appleton and Barnett proved the existence of a reflective layer in about 90 km height [*Barnett*, 1974]. Later, both ground and rocket measurements determined that in fact three (sometimes four) ionized layers exist. These are called the D, E, and F layers (where the F layer sometimes exhibits two peaks in electron density and is called F1 and F2) [*Waynick*, 1974]. The E layer was named after the electric fields discovered there, and when more layers were discovered they were named alphabetically [*Kelley*, 2009].

UV radiation from the sun has enough energy to ionize the neutral gas in the atmosphere. During daytime, this is the main ion production mechanism in the ionosphere. Since the density of the atmosphere increases with decreasing altitude, and photons are absorbed by photoionization, the ionization is more intense at high altitudes. The plasma density is highest in the F layer, usually located between 150-500 km. The E layer is located at 90-150 km altitude, and the D layer at below 90 km. The combination of altitude dependent absorption, recombination and neutral density gives the ionosphere its distinct layer-profile. Due to the absence of sunlight, ionization is lower at night, and the D layer often disappears completely. At higher latitudes, particle precipitation is also an important ionization factor [*Kelley*, 2009; *Baumjohann and Treumann*, 1996].

2.6 Precipitation Maps

The energy and pitch angle of individual precipitating particles decides how deep they will penetrate into the ionosphere. The pitch angle (often denoted α) of a charged particle is the angle between the magnetic field vector and the velocity vector of the particle (see e.g. *Baumjohann and Treumann* [1996]). Particles that have pitch angles close to 0° as they approach the atmosphere are likely to collide with other particles and lose their energy (precipitate). Because the high-latitude ionosphere is connected to most of the magnetosphere through magnetic field lines, the particles that precipitate in the ionosphere can be traced back to a location in the magnetosphere.

Maps of precipitation regions and their connection to the magnetosphere have been constructed by *Newell* [2004], one map from the article is included here as Figure 2.14. Because the configuration of the magnetosphere is different during quiet and storm condition, so is the location of the precipitation in the high-latitude ionosphere. Precipitation of ions is dependent on both ring current strength and substorm activity [*Hauge and Søraas*, 1975; *Hardy et al.*, 1989]. The precipitation shifts equatorward with decreasing Dst. *Hauge and Søraas* [1975] also found that the precipitation sometimes occurs in two separate zones, at ILAT $\approx 65^\circ$ and ILAT $\approx 75^\circ$. The poleward zone was found to have an isotropic distribution of particle pitch angles, which persisted also during quiet conditions. In the course of a substorm the zone was observed to shift slightly equatorward, with a following poleward expansion.

Figure 2.14 shows how the statistical ionospheric precipitation pattern looks like for typical storm conditions, with negative IMF B_z and B_y (that is, the z and y component of the IMF).

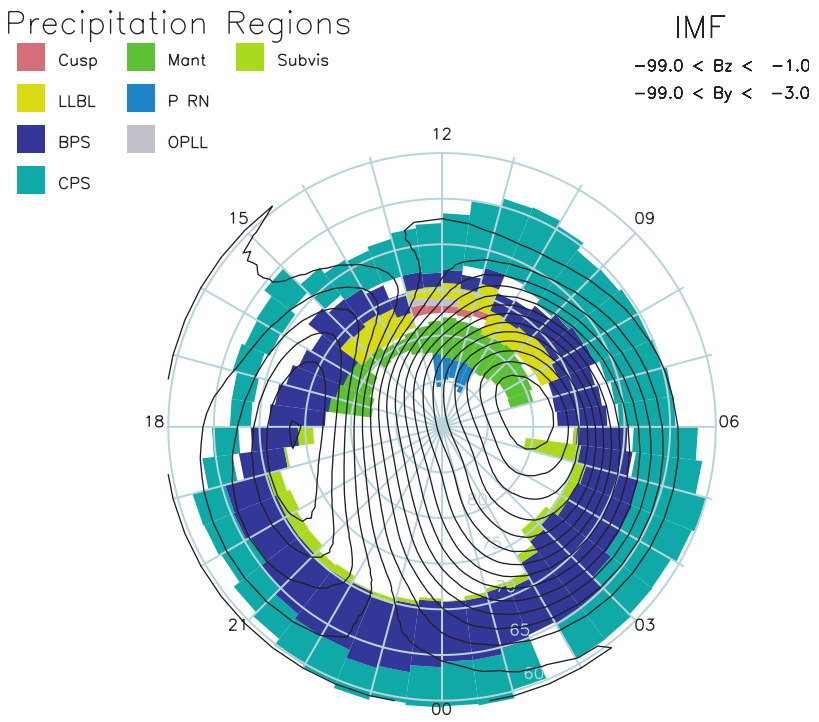

Figure 2.14: Figure showing how different particle population regions in the magnetosphere map down to the ionosphere. Colors; Pink = Cusp. Yellow = Low Latitude Boundary Layer. Dark Blue = Boundary Plasma Sheet. Turquoise = Central Plasma Sheet. Dark Green = Plasma Mantle. Light Blue = Polar Rain. Grey = Open Low Latitude Boundary Layer. Light Green = Subvisual Region. The black contours indicate the average convection pattern. For a thorough explanation of precipitation regions and the construction of the maps, see *Newell* [2004].

Hardy et al. [1985, 1989] have mapped the statistical distribution of particle flux and energy for electrons with energies 50 eV to 20 keV, and ions with energies 30 eV to 30 keV. They showed that precipitation generally occurs in a well-ordered pattern in magnetic local time. For all levels of magnetic activity, *Hardy et al.* [1989] found that the higher levels of precipitating integral energy flux occurred in a C-shaped region symmetric about a premidnight-prenoon meridian. They also found that the maximum value of the integral energy flux was located premidnight and independent of the activity level. This will be highly relevant for the calibration method we are developing in this thesis. The satellite's location in MLT will affect how much, and how energetic, radiation the satellite is exposed to, and thus how fast and how much the proton detector degrades. When we calibrate the NOAA satellites, the general approach is to compare the degraded satellite to a new satellite. However, if the two satellites are located in different region, we need to take into consideration that the two satellites are sampling different particle

populations.

To illustrate how the average particle flux vary for different levels of activity, Figure 2.15 shows the broadening and equatorward movement of the oval with increasing magnetic activity. The C-shaped region of higher integral energy flux is clearly visible in Figure 2.16. Both figures are from the *Hardy et al.* [1989] article. Figure 2.15 shows color spectrograms of the average integral number flux for Kp 0 (upper left), 1 (lower left), 2 (upper right), and 3 (lower right). The spectrograms are plotted in an MLT-corrected geomagnetic latitude coordinate system. The scale of the colorbar is logarithmic with four color division per decade in the number flux ranging from $10^4 - 10^8$ ions/cm^2 s sr. Figure 2.16 shows the average integral energy flux of protons for Kp 4 (upper left), 5 (lower left), and ≥ 6 (right). The scale is the same as in Figure 2.15. Midnight is at the bottom, and dawn is to the left in both figures.

Both *Newell* [2004] and *Hardy et al.* [1989] used satellites from the Defense Meteorological Satellite Program (DMSP) to construct average precipitation maps. The use of DMSP limits the ion energy range to 30 eV - 30 keV. NOAA satellites measure ions with energies ranging from 30 keV to several MeV, and NOAA data will be used to construct similar maps for different activity levels in this thesis. However, the goal of constructing maps of average precipitation maps with NOAA data is to use them as part of the calibration. The NOAA precipitation maps will therefore not perfectly cover all MLT sectors, but the coverage is satisfactory for the purpose of recalibration. Because of the lower ion energies of the *Newell* [2004] and the *Hardy et al.* [1989] precipitation maps, these are not suited to recalibrate NOAA data.

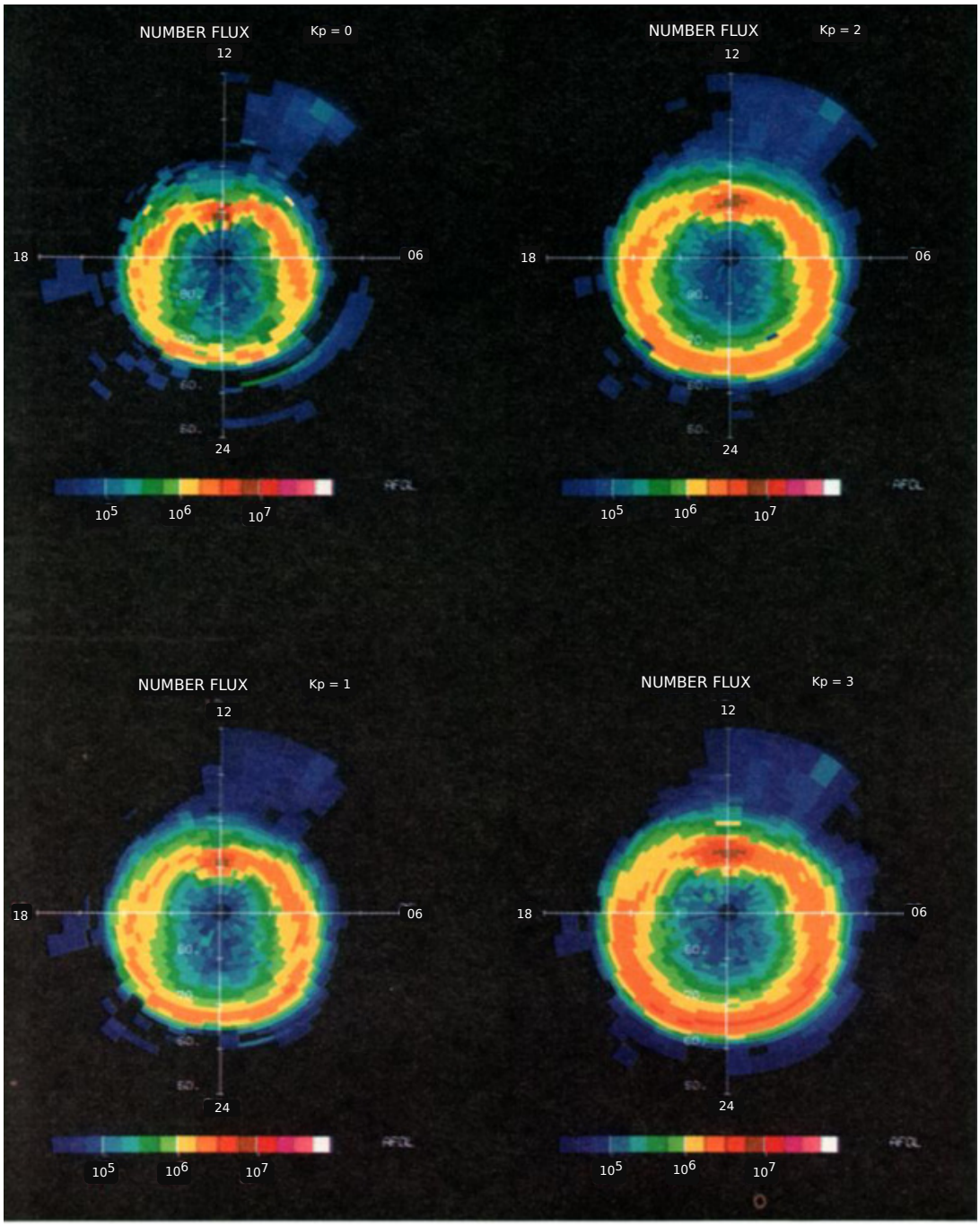

Figure 2.15: Color spectrograms of the average integral number flux for Kp 0 (upper left), 1 (lower left), 2 (upper right), and 3 (lower right). The spectrograms are plotted in a MLT-corrected geomagnetic latitude coordinate system. The scale is logarithmic with four color division per decade change in the number flux ranging from $10^4 - 10^8$ ions/cm^2 sr s. See *Hardy et al.* [1989] for the complete figure.

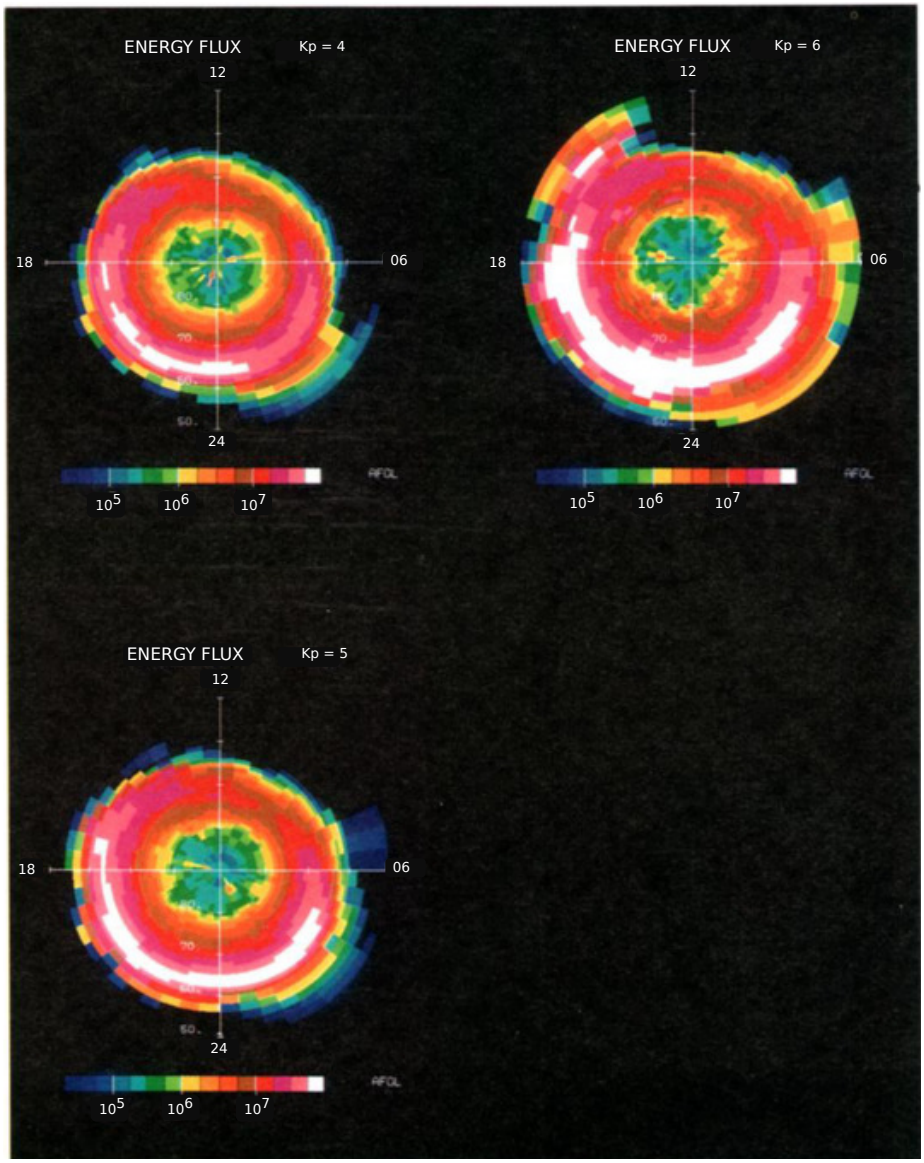

Figure 2.16: Color spectrograms of the average integral energy flux for Kp 4 (upper left), 5 (lower left), and ≥ 6 (right). The spectrograms are plotted in a MLT-corrected geomagnetic latitude coordinate system. The scale is logarithmic with four color division per decade change in the number flux ranging from $10^4 - 10^8$ keV/cm^2 sr s. See *Hardy et al.* [1989] for the complete figure.

Chapter 3

National Oceanic and Atmospheric Administration Satellite Programs

The previous chapter provided some insight to relevant space physics theory. In this chapter we will present the NOAA program, and the NOAA satellites that we will later calibrate. The MEPED instrument will be described, and a general introduction on solid-state detectors is given. How the solid-state detectors are degraded by particle radiation is also discussed. A short presentation of the NOAA dataset will follow, before we look closer on the time evolution of uncalibrated NOAA data.

3.1 NOAA POES Satellite Program

The National Oceanic and Atmospheric Administration (NOAA) is a science-based federal agency in the USA, which has its primary focus on monitoring the oceans and the atmosphere. Geostationary Operational Environmental Satellites (GOES) and Polar Operational Environmental Satellites (POES) orbit the Earth several times a day and provide a continuous stream of data for many applications. When we in this thesis refer to NOAA satellites, we generally mean NOAA/POES. GOES satellites are not discussed further.

The first weather satellite was launched in 1960. In 1978 TIROS-N[1] was launched as the first satellite in the "NOAA" series of operational satellites. TIROS-N was greatly improved in comparison to earlier weather satellites, and it marked the start of a new generation of satellites.

Since NOAA 18, NOAA has cooperated with the European Organization for the Exploitation of Meteorological Satellites (EUMETSAT) on the Initial Joint Polar-Orbiting Operational Satellite System (IJPS), with one NOAA and one MetOp polar-orbiting

[1]Television Infra-Red Obsevation Satellite

satellite working in constellation. The spacecrafts are provided by NASA and ESA[2]. In total 12 NOAA series satellites have been launched into polar orbit since 1978 [*Davis*, 2007]. In addition, two MetOp-satellites have been launched into polar orbit by EUMETSAT[3].

Besides instruments for weather forecasts and climate analysis, the NOAA satellites carry equipment for studies of the environment in space. Data from NOAA satellites have been used in space science research to for example make an estimate of the ring current injection rate [*Søraas et al.*, 2002], to study the storm time equatorial belt [*Søraas et al.*, 2003], to study the behavior of the radiation belt protons during large magnetic storms [*Zou et al.*, 2011], and to study the effect of energetic particle precipitation on the mesosphere [*Daae et al.*, 2012; *Codrescu et al.*, 1997].

Figure 3.1 shows the lifetime of all the NOAA satellites. The sunspot number is also shown as the dashed curve in the figure to emphasize that NOAA satellites have been operational for almost three full solar cycles.

[2] `http://www.nesdis.noaa.gov/SatInformation.html,http://www.eumetsat.int/Home/Main/Satellites/Metop/index.htm)`

[3] `http://www.eumetsat.int/Home/Main/Satellites/Metop/MissionOverview/index.htm?l=en`

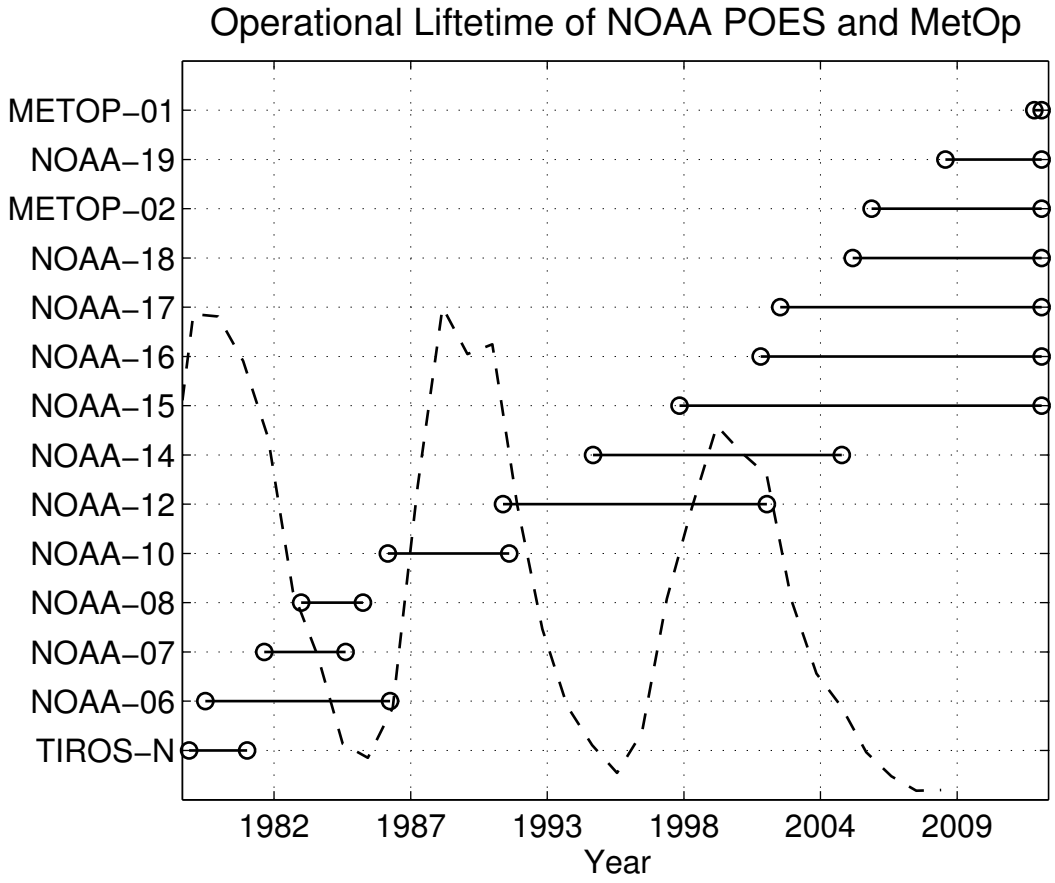

Figure 3.1: The operational lifetime of all NOAA POES satellites, including MetOp-02 and MetOp-01. The sunspot number is shown as a dashed curve.

This thesis will concentrate on satellites of the newest generation, starting with NOAA 15. Table 3.1 presents the approximate coverage in MLT for the new generation of satellites. The first range indicates where the satellite entered the evening/night sector in the Northern Hemisphere, the second range where it left the morning/day sector in the same hemisphere. The MLT coverage is given for each year when a new satellite is launched. Both NOAA 15 and NOAA 16 have rotated out of the launch-plane during the satellites' lifetimes. Another important feature presented in Table 3.1 is that on three occasions a new satellite was launched into almost the same plane as an old satellite. These are NOAA 18 and NOAA 16 in 2005, MetOp 02 and NOAA 17 in 2006 and NOAA 19 and NOAA 18 in 2009. Figure 3.2 shows the footprints of all six satellites in 2009.

Table 3.1: MLT coverage in the launch years of NOAA and MetOp satellites

Sat.	1998	2001	2002	2005	2006	2009
N 15	18-19 / 7-9	18-19 / 7-9	18-19 / 7-9	17-18 / 5-7	17-18 / 5-7	16-17 / 4-6
N 16	-	2-4 / 12-14	2-4 / 12-14	2-5 / 14-16	3-5 / 14-16	16-18 / 5-8
N 17	-	-	20-22 / 10-12	21-22 / 10-12	21-22 / 10-12	20-22 / 8-10
N 18	-	-	-	2-4 / 12-14	2-4 / 12-14	2-4 / 12-14
M 02	-	-	-	-	20-22 / 9-11	20-22 / 9-11
N 19	-	-	-	-	-	2-4 / 12-14

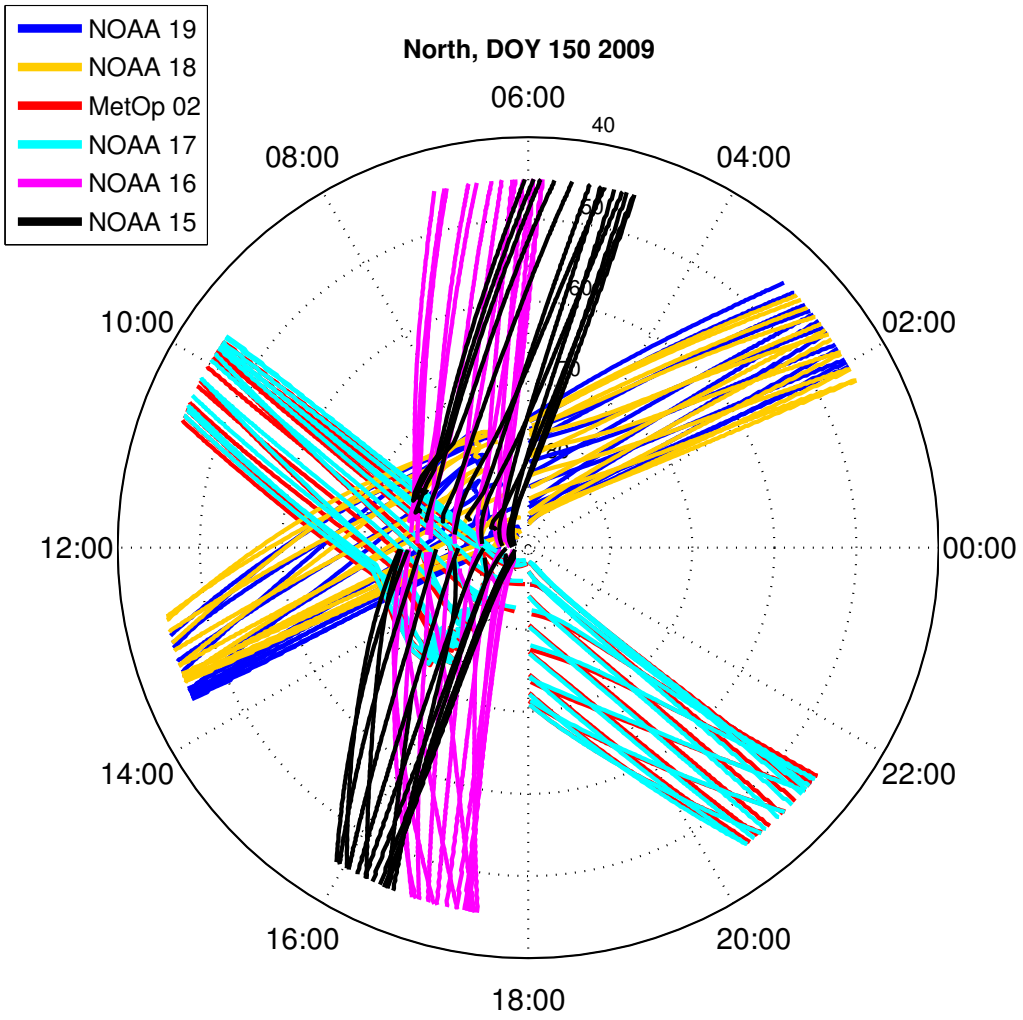

Figure 3.2: The footprints of NOAA 15 (black), NOAA 16 (pink), NOAA 17 (light blue), NOAA 18 (mustard), NOAA 19 (dark blue) and MetOp 02 (red, very close to NOAA 17) in 2009. The plot is in MLT/ILAT coordinates in the Northern Hemisphere. Noon is to the left, dawn is at the top of the plot. The perimeter is ILAT= 40 and each circle is 10° apart.

Because of the Earth's counterclockwise rotation under the satellites, the satellites will pass over slightly different locations for every orbit. The geographical coverage on a random day is displayed in Figure 3.3. The figure shows the location of NOAA 18 as white tracks across a geographical map. A red box indicates the satellites position at the beginning of the day, and a red triangle indicates the end of the day. Displayed as different colors along the track is the comparison of precipitating protons with energies

30-80 keV to the median response of the detector over the last year. Close to the poles the auroral regions are visible. Over the South American continent we see the South Atlantic Anomaly as an elevated flux of precipitating protons.

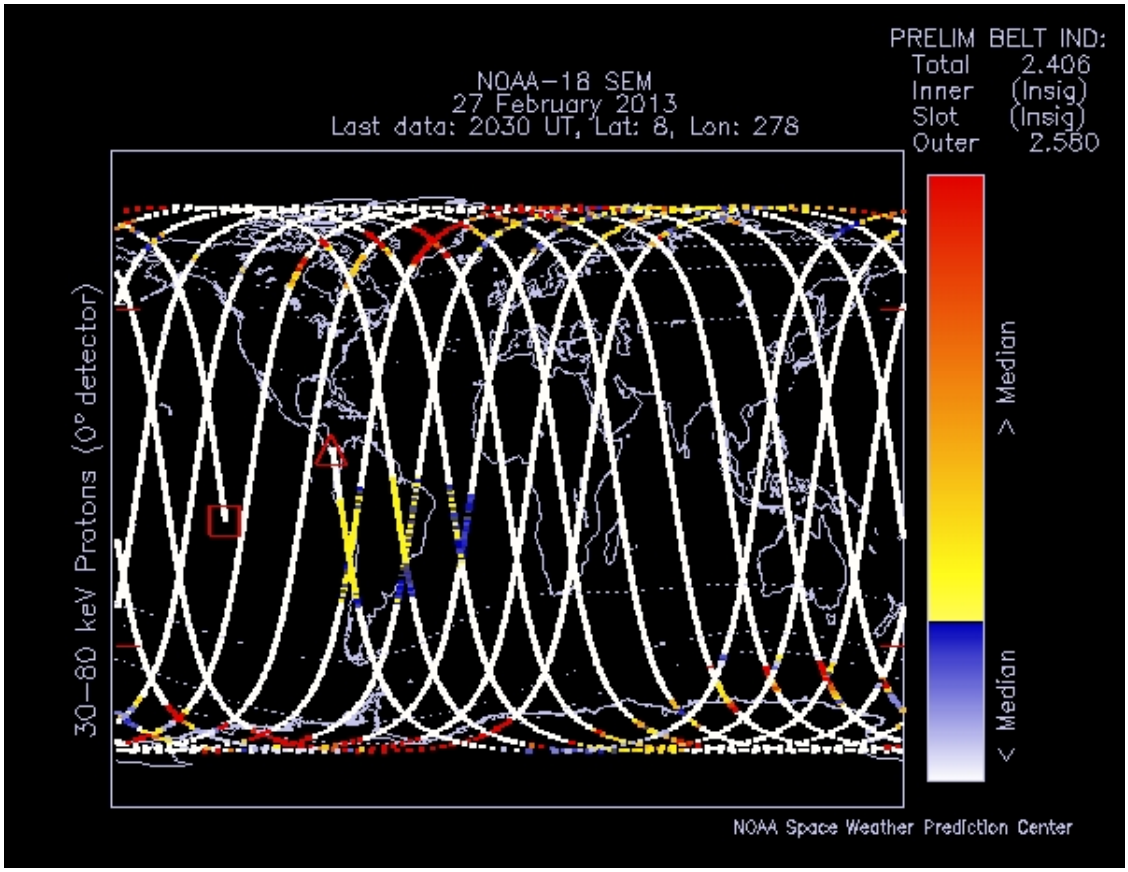

Figure 3.3: The geographical coverage of NOAA 18 on 27 February 2013. The red box in the plot shows the location of the beginning of the satellite track for the day. The red triangle indicates the location of the end of the day [`http://www.swpc.noaa.gov/tiger/`].

3.2 Instrumentation Onboard the POES Spacecraft

The NOAA/POES spacecraft is illustrated in Figure 3.4 from *Raben et al.* [1995]. The newest generation of NOAA satellites has a mass of 1475 kg in orbit and are 4.2 m long $\times$ 1.88 m in diameter. The designed lifetime is 12 years[4]. The orbits of the satellites are sun-synchronous, and a full orbit takes approximately 100 minutes, which entails 14-15 orbits per day. The orbital altitude is about 800-850 km. The MEPED detector is part

[4][`http://www.tbs-satellite.com/cgi-bin/wwwwais`]

of the Space Environment Monitor instrument package carried by all NOAA spacecrafts.

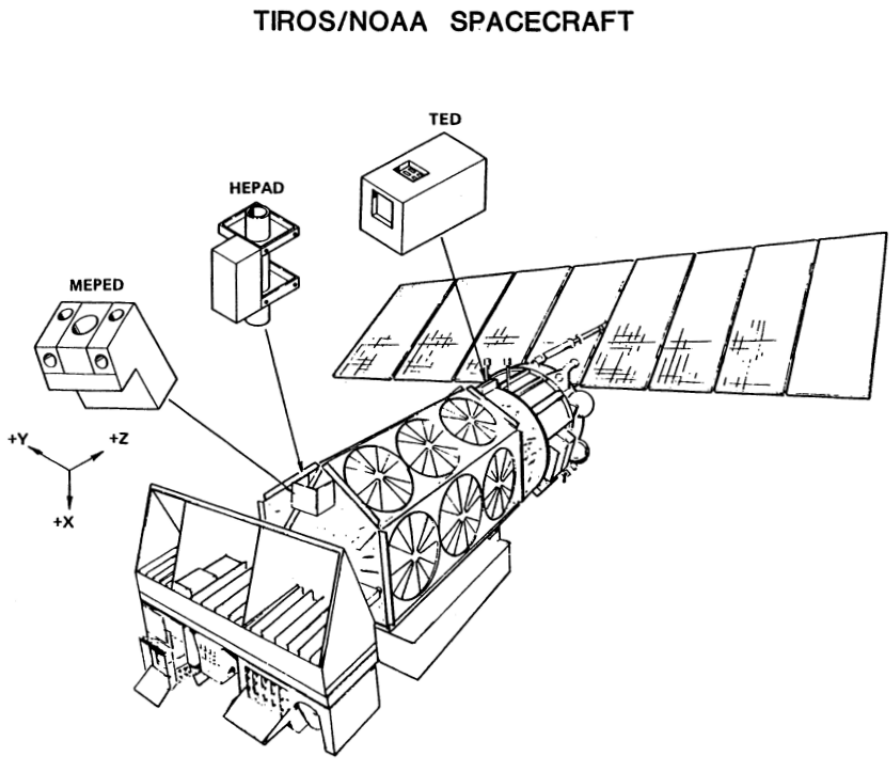

Figure 3.4: A cartoon of the NOAA spacecraft. The positions of the MEPED, HEPAD, and TED instruments are indicated. The satellites move in the -Y direction. The cartoon is adopted from *Raben et al.* [1995].

3.2.1 The Space Environment Monitor (SEM)

The NOAA/POES satellites carries a Space Environment Monitor (SEM) instrument package for detection of protons and electrons. The SEM package was modernized in the late 1990's [*Evans and Greer*, 2004] and starting from NOAA 15 the satellites carried the SEM-2, while the old version was called the SEM-1. The SEM package measures charged particles with three different instruments, the Total Energy Detector (TED), the High Energy Proton and Alpha Detector (HEPAD), and the Medium Energy Proton Electron Detector (MEPED). In Figure 3.4 the position of MEPED, TED and HEPAD are indicated [*Raben et al.*, 1995]. The TED and HEPAD will not be discussed further in this thesis.

The Medium Energy Proton Electron Detector

The MEPED instrument is designed to measure energetic protons and electrons, and there are two detectors for each charge type [*Evans and Greer*, 2004; *Galand and Evans*, 2000]. The two proton detectors have a nearly orthogonal field of view, with one detector pointing radially outward along the Earth-satellite vector (hereafter called the 0° detector because it measures mainly protons with pitch-angles of 0°), and one pointing in the anti-parallel direction of the spacecraft velocity vector (hereafter called the 90° detector because it measures mainly protons with pitch-angles of 90°). With reference to Figure 3.4 this will be in the -X and +Y directions respectively (the satellite move in the -Y direction). To ensure the detectors have a clear field of view, the detectors are tilted 9° away from the vectors described. Protons are measured by MEPED in six (five in SEM-1) differential energy channels with ranges provided in Table 3.2.

Table 3.2: Nominal energy ranges of the proton detectors of the MEPED SEM instruments [*Evans and Greer*, 2004; *Galand and Evans*, 2000].

Energy Channel	SEM-2 (keV)	SEM-1 (keV)
P1	30-80	30-80
P2	80-240	80-250
P3	240-800	250-800
P4	800-2500	800-2500
P5	2500-6900	2500-6900
P6	> 6900	N/A

Figure 3.5 shows a cross-sectional schematics of a MEPED proton detector by *Evans and Greer* [2004]. A magnetic field is applied to prevent electrons up to about 1000 keV from entering through the collimator. As additional protection, the detectors are protected by shielding made of aluminum and tungsten. There are two solid-state detectors stacked on top of each other behind the collimator. The collimator has an opening of 30 steradians (sr). A steradian can be defined as $\Omega = A/r^2$, where Ω is the solid angle subtended at the center of a sphere with radius r, and A is the area on the surface of the sphere limited by Ω. Particles that enter the first detector are sorted into five energy bands according to their energy loss in the detector. If a particle penetrate to the second detector the particle is sorted into the sixth energy band. An electronic pulse height analyzer is used to determine the energy of the particles [*Evans and Greer*, 2004].

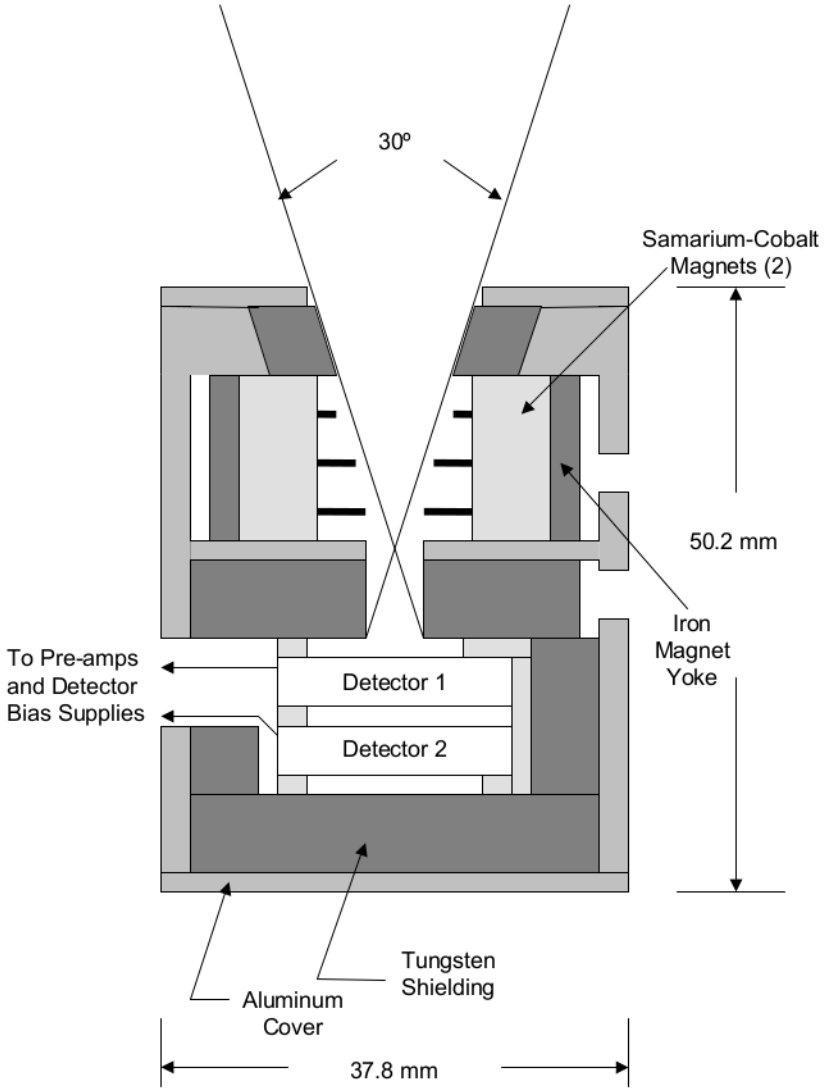

Figure 3.5: Cross-section schematics of the MEPED proton solid-state detector. Protons enter through the collimator. Particles that are stopped in the first detector are sorted according to their energy loss in the detector. Particles with great enough energy to penetrate to the second detector are sorted into the highest energy channel. Electronic pulse height analysis is used to determine the energy of a particle. Electrons are stopped by the magnetic field applied over the collimator and by the shielding around the detector [*Evans and Greer*, 2004]. The collimator has an opening of 30 sr.

3.2.2 Solid-State Detectors

The MEPED proton detectors were reported to show signs of degradation by e.g. *Galand and Evans* [2000] and *Wüest et al.* [2007]. To understand how the detector gets degraded, we first present some general features of a silicon solid-state detector.

Silicon solid-state detectors (SSD) are built using ultra pure silicon crystals. Silicon has chemical properties that allow its atoms to form tight covalent bonds by sharing its four valence electrons with four surrounding atoms, filling up the valence band of all the atoms and forming a crystal structure. A pure silicon crystal can conduct only a small amount of current. To make a good semiconductor from the silicon crystal, an impurity is introduced (called "doping"). The impurity has a slightly different structure than silicon, but can be combined with silicon to maintain a crystal form. The dopant introduces charge carriers to the crystal which makes it easier for electrons to be excited into the conducting band of the material, i.e. it becomes conducting. When silicon is doped with an atom that has five electrons in its valence band, the crystal becomes n-doped (n for extra negative charge introduced). If the dopant has only three valence electrons, the silicon crystal becomes p-doped (p for extra positive charge introduced).

In an SSD, a so-called p-n-junction is created by putting together a p-doped and an n-doped piece of silicon. In the boundary layer between the p-doped and the n-doped material, some of the electrons and holes will recombine, creating a region called a space-charge region. The recombined electron and hole leave behind a positively and negatively charged nucleus separated by the space-charge region created, resulting in an electric field between these charges. An external electric field can be applied to decrease or increase the internal electric field in the p-n-junction. In an SSD the electric field is increased, and it will operate as a reverse biased diode (see Figure 3.6).

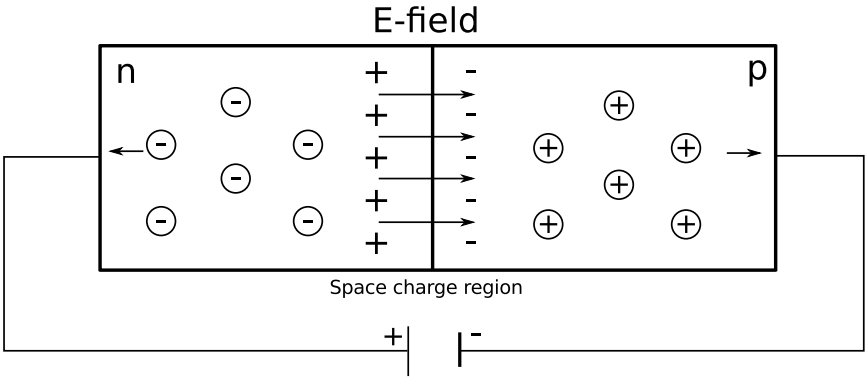

Figure 3.6: An externally applied electric field will separate the extra charges of the p and n doped material. Electrons will move opposite to the applied electric field, while positive holes move in the direction of the applied field. The result is a region at the intersection of the p doped and n doped material where an internal electric field is created due to the removal of excess charge. This region is called the space charge region. The minuses and pluses drawn inside a ring represents electrons and holes respectively. The plus and minus signs without a circle represents the remaining positively and negatively charged nuclei of the dopant after recombination in the space charge region.

We want the space-charge region of the p-n-junction to be as large as possible, meaning that the electric field in the material is large. When a charged particle enters a solid-state detector, it will interact with the valence band electrons and excite them to the conducting band. When an electron leaves the valence band, a hole is created in its place. If this electron-hole pair is created inside the space-charge region of the p-n-junction, the electron and hole (which behave as a positive charge) will move in response to the electric field. The external electric field prevents the electron-hole pair from recombining, and electrodes collect the released charge. The collected charge is proportional to the energy lost by the incoming particle [*Cutnell and Johnson*, 2013; *Wüest et al.*, 2007; *Evans and Greer*, 2004]

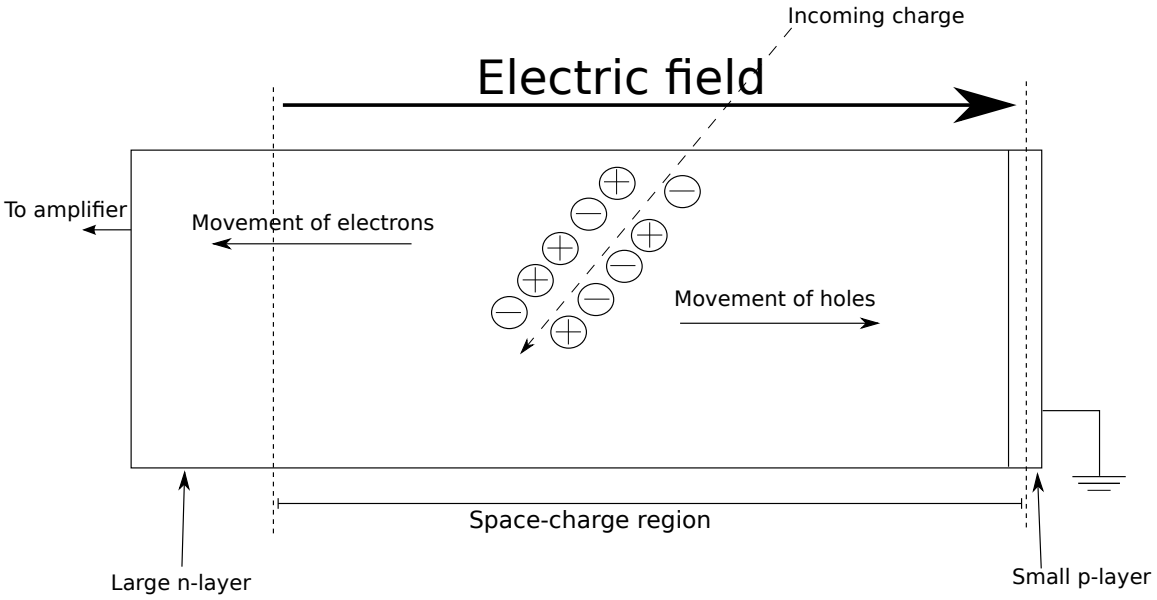

Figure 3.7: A sketch of an SSD showing the creation of electron-hole pairs by an incoming particle.

In MEPED a pre-amplifier converts the collected charge into a voltage pulse. This is fed to a linear amplifier which produces a slightly different kind of pulse that has an amplitude proportional to the collected charge. By counting the number of pulses and their height each second, the energy distribution of incoming particles is obtained [*Raben et al.*, 1995]. The pulses are sorted into energy channels with energy thresholds given in Table 3.2.

Degradation

Particles hitting a solid state detector can impair the crystal structure mainly in two ways.

1. *A dead layer forms on the surface of the detector.* A dead layer is a part of the detector crystal that lacks an electric field, thus charge carriers produced in this layer are not collected. However, an incident particle does loose some of its energy in this layer, and the particle's energy is therefore underestimated in the detector.

2. *Atoms in the crystal structure of the detector can be displaced from its position by incoming ions.* This will decrease the mobility of the free charges released in the detector. When the mobility of the free charges is reduced, they are not all collected by the amplifier. This will lead to an underestimation of the energy of the detected particle.

When the energies of incoming particles are underestimated, this effectively means that the energy threshold of the detector channels are increased. A 30 keV particle would

initially be registered as one count in the lowest energy channel, but in a degraded detector it will look like a particle with lower energy and hence not be registered as a count. Consequently, the effective energy threshold has increased.

At the same time the incoming flux will be underestimated, since no particles below the increased energy threshold are registered.

3.3 NOAA data

In this thesis, we use data from 6 identical NOAA satellites with the SEM-2 instrument package (NOAA 15, 16, 17, 18 and 19, and MetOp 02). A full data set from both MEPED detectors is acquired every 2 seconds [*Evans and Greer*, 2004]. However, we will use a more compact and convenient way of presenting the data which has also been used by e.g. *Hauge and Søraas* [1975], *Lundblad et al.* [1979] (on ESRO 1A) and *Oksavik* [1998] (on NOAA 12) . The binning procedure is explained in the next section.

3.3.1 Data Binning

Figure 3.8 from *Oksavik* [1998] illustrates how the data used in this thesis are binned. The upper panel shows a pass across the Northern Hemisphere, from the evening sector to the morning sector. Measurements of electrons from the 0° detector (solid line) and 90° detector (dashed line) are shown. The vertical red line indicates the highest latitude intersected by the spacecraft, which separates the evening and morning sectors. In both hemispheres, a NOAA pass is divided into morning and evening sectors based on magnetic local time. 00 <MLT< 12 or 06 <MLT< 18 is defined as morning and the remaining MLT sector is thus evening. The Northern and Southern Hemisphere are distinguished by positive and negative ILAT, respectively. For MEPED (protons and electrons) the pass across a sector from ILAT 45° to 90° is processed into columns of 0.25° width. Data from ILAT $< 45°$ is not included in the dataset we use.

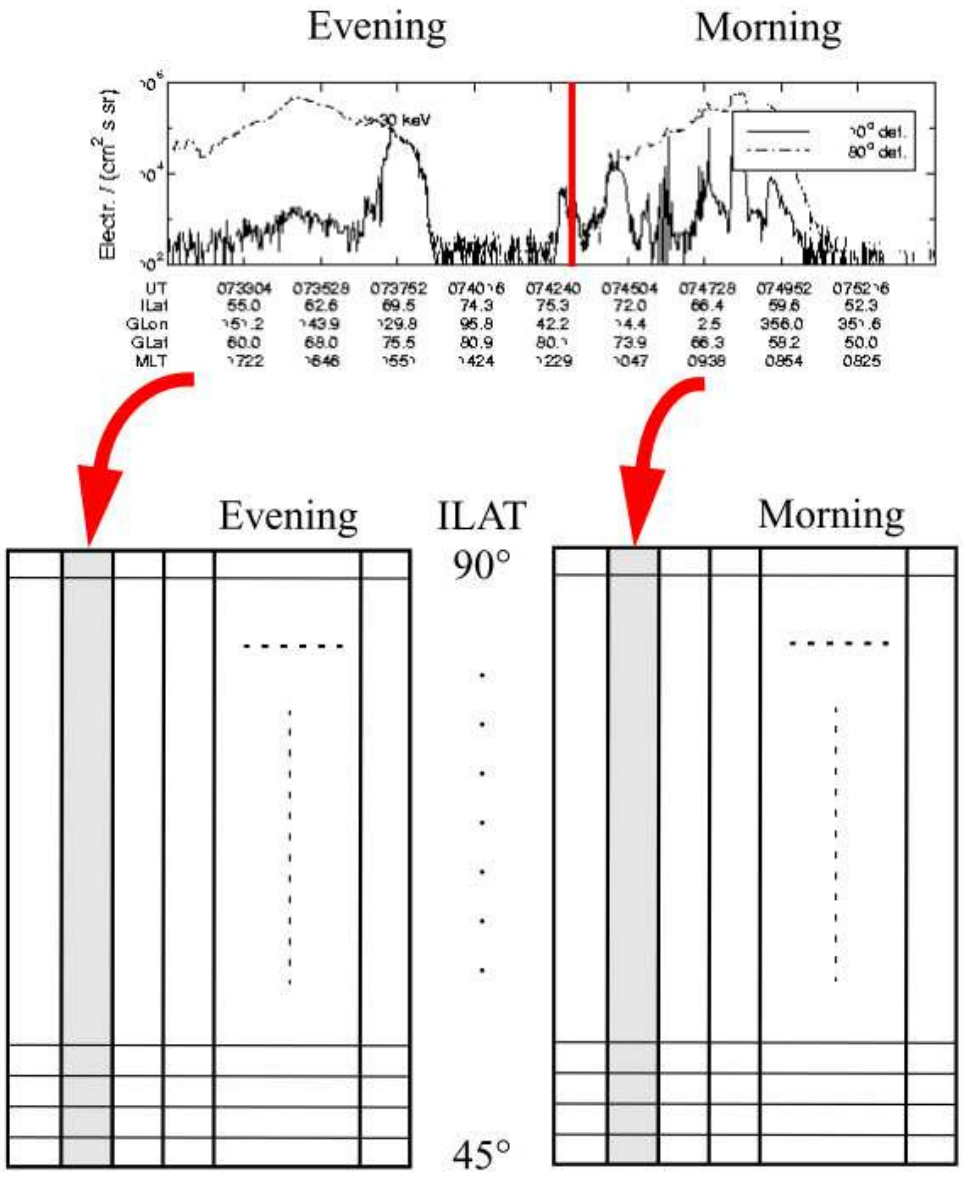

Figure 3.8: The figure shows how the NOAA data are sorted into sectors. Each individual pass is divided into morning and evening at the highest ILAT reached by the satellite. Next, each pass is processed into bins in a column from 45° to 90° ILAT. For MEPED, each column is 0.25° wide in latitude and contains the average flux detected within that invariant latitude interval. The figure is adopted from *Oksavik* [1998].

3.4 Time Evolution of Uncalibrated Data

We will now present and discuss uncalibrated data from NOAA satellites to visually inspect the degradation of the MEPED proton detector. First we take a closer look on the longest operating satellite in this study, NOAA 15, from launch in 1998 to today. Thereafter, we compare uncalibrated data from NOAA 15, NOAA 16, NOAA 17, NOAA 18, MetOp 02 and NOAA 19 from 2005 to 2010.

In Figure 3.9 we inspect the time evolution of proton flux in the 0° detector onboard NOAA 15 from 1999-2012. The data are from the Northern Hemisphere evening sector. In the top panel, the yearly averaged sunspot number is plotted up to 2012. NOAA 15 was launched in 1998, not long before maximum in solar cycle 23, which was reached in the year 2000. The Dst index is plotted in the second panel of the figure. Several large storms can be seen during solar cycle 23. Towards the solar minimum in 2008/2009, the Dst index shows a general decrease in activity. When the sunspot number increases after 2009, we also find an increase in the Dst index.

The 3rd, 4th, and 5th panels of Figure 3.9 displays the particle measurements by NOAA 15 from 1999-2012. The three panels are data from the P1, P2, and P3 channels, respectively. All data are averaged over one day. The color scale is logarithmic, and the flux is plotted vs ILAT and day. The maximum flux of precipitating protons is found approximately at ILAT 60° to 80°. The flux in this region is several orders of magnitude larger than at high and middle latitudes. We will denote this region where the maximum of precipitating flux is found the proton oval. The proton oval is seen to extend to higher and lower latitudes during geomagnetic storms. One extreme example of this can be seen late in 2003, during the famous Halloween storm [*Balch et al.*, 2004]. High fluxes of precipitation is seen from ILAT = 45° to ILAT = 90°. Around the solar cycle minimum, the proton oval is narrower and situated at slightly higher latitudes. The decreasing intensity of the precipitating flux with time is obvious in all three energy channels. The decrease in flux intensity is not only due to degradation, we find that it corresponds well with the declining solar cycle and decreasing Dst index. However, when the Dst index and sunspot number increase after 2009, we do not find a correspondingly large increase in the flux intensity. This is most likely due to the detector degradation, and is most easily visible in the P2 and P3 channels. Geomagnetic activity tends to enhance during the descending phase of a solar cycle [*Gonzalez et al.*, 1994], and the comparison of measurements from one satellite against itself should thus be done in the same phase of the two solar cycles. The years 2011/2012 are comparable with the year 1999, since both epochs are right before solar maximum in two solar cycles. When comparing the flux intensity in 2011/2012 with the flux intensity in 1999 there is a clear decrease in the measured flux.

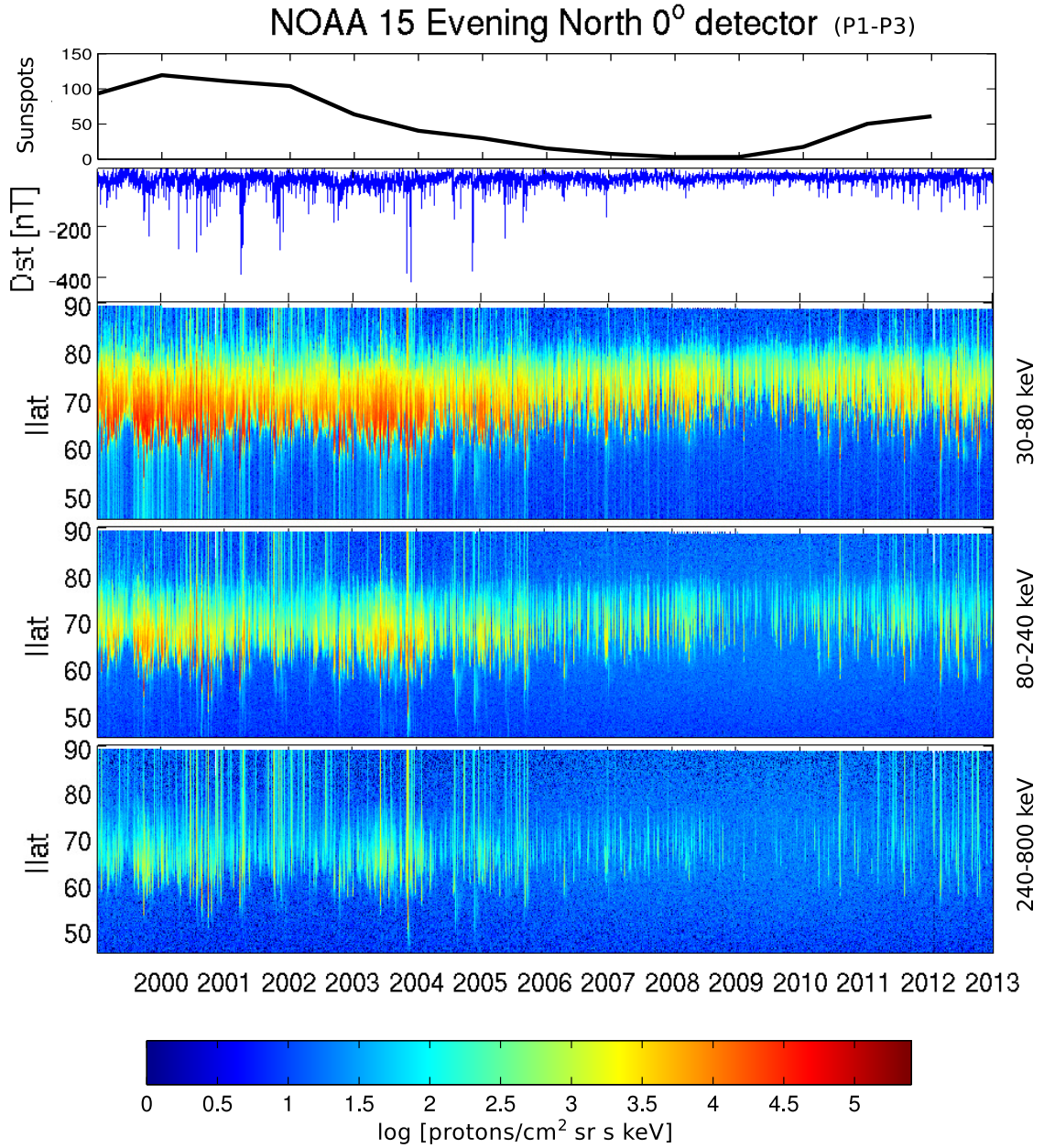

Figure 3.9: The top panel shows the yearly average sunspot number from 1999-2012 plotted at the start of each year. The second panel shows the Dst index. The 3rd, 4th and 5th panels show measurements from the 0° detector onboard NOAA 15 from P1, P2, and P3 respectively. The flux measurements are averaged over one day, and plotted on logarithmic color scale vs ILAT and day. The intensity of the flux is much larger in 1999-2005 than the following years. The sunspot number shows the maximum of solar cycle 23 in 2000. Solar cycle 24 starts at the end of 2008. The Dst index shows that the period 2008-2009 was quiet, and that the activity increases when the sunspot number increases from 2009. The intensity of the flux is also seen to increase after 2009, however, not to the levels seen before the maximum in solar cycle 23.

The Figure 3.10 displays the same as Figure 3.9, but with measurements from the 90° detector. The sunspot number is shown in the first panel, the Dst index is shown in the second panel, and the P1, P2, and P3 channels are shown in the 3rd, 4th, and 5th panels respectively. We see in the figure that the maximum flux of protons with pitch-angles of 90° is found coinciding with the maximum flux measured by the 0° detector. We also see that the region moves to higher latitudes at solar minimum compared to the solar maximum. The decrease in flux is evident in the 90° detector as well. As discussed, some of the decrease in flux is due to lower activity, however, when we compare fluxes from 2011/2012 with 1999, the degradation can clearly be seen. The degradation is easier to see in the P1 channel of the 90° detector than the 0° detector.

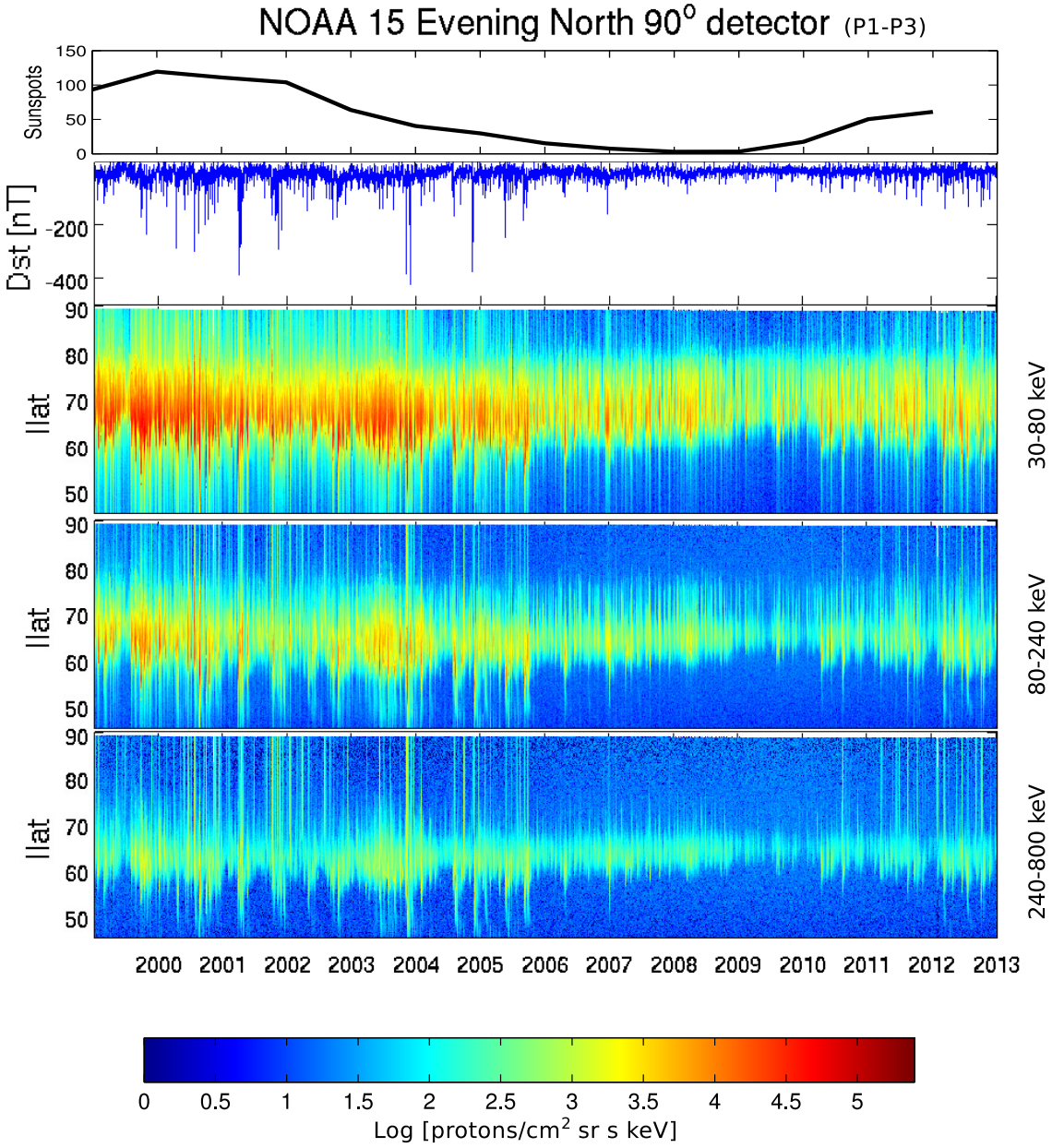

Figure 3.10: The top panel shows the yearly average sunspot number from 1999-2012. The second panel shows the Dst index. Third panel shows for the 90° detector the logarithmic daily averaged differential flux of precipitating protons with energies 30-80 keV (P1), plotted vs ILAT for each day in the period 1999-2012. Fourth and fifth panel shows the same for protons with energies 80-240 keV (P2) and 240-800 keV (P3), respectively. The same trends are seen in the 90° detector as for the 0° detector in Figure 3.9. The intensity of the flux is seen to decrease with time.

In Figure 3.11 we inspect a smaller time series, but compare measurements from all six satellites with each other. The period is the years 2005-2010, around solar minimum. The yearly average sunspot number is shown in the upper panel, and the Dst index in the second panel. The six color plots display measurements from NOAA 15, NOAA 16, NOAA 17, NOAA 18, MetOp 02 and NOAA 19. The flux is averaged over one day, and plotted in logarithmic color scale vs ILAT and day. All measurements are from the P1 channel of the 0° detector, and from the respective evenings sectors. The evening sector is, as previously noted, not the same MLT for all of the satellites. Table 3.1 lists the evening and morning sectors for all the satellites. Because of the common orbital plane of NOAA 16 and NOAA 18, they are well suited for a comparison. The most reasonable time to compare the two satellites is in 2005 when NOAA 18 is newly launched, and the detector can be assumed undegraded. The intensity of the flux measured by NOAA 16 in 2005 is lower compared to the flux measured by NOAA 18. The intensity of the flux measured by NOAA 15 is visibly lower than the other satellites through the entire period 2005-2009. MetOp 02 orbits in the same sector as NOAA 17, and NOAA 19 orbits in the same sector as NOAA 18. The degradation is not as easily found by visual inspection for NOAA 17 and NOAA 18.

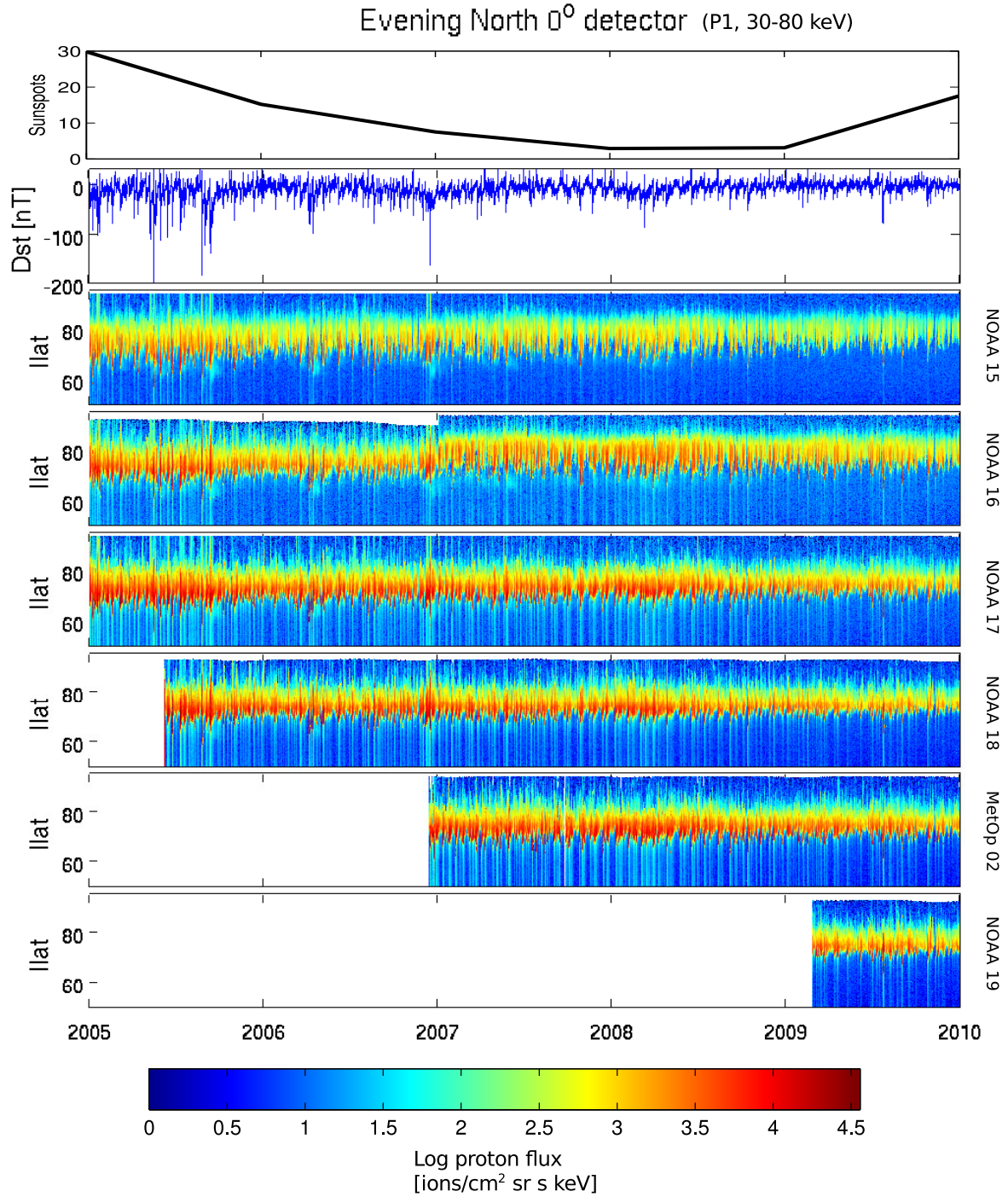

Figure 3.11: A comparison of flux intensity in the P1 channel of the 0° detector onboard NOAA 15, NOAA 16, NOAA 17, NOAA 18, MetOp 02 and NOAA 19 in the years 2005-2009. P1 measures protons with energies 30-80 keV. For all satellites, the flux from the evening north sector is averaged over one day. The flux is plotted vs ILAT and time, with the colorbar indicating the logarithmic intensity of the flux. The top panel shows the yearly averaged sunspot number (solid line) and the predicted sunspot number (dashed line). The second panel shows the Dst index for the period. White space indicates that the satellite has not been launched.

Figure 3.12 shows the flux measured in the P2 channel of the 0° detector of all six satellites from the evening sector in the Northern Hemisphere. The period displayed is the same as in Figure 3.11. In the P2 channel, the degradation of NOAA 16 compared to NOAA 18 is obvious.The degradation of NOAA 17 compared to MetOp 02, and NOAA 18 compared to NOAA 19 is visible in the P2 channel. In 2009, we can also see that compared to NOAA 19, all the satellites measure a lower flux.

Figure 3.13 shows the P2 channel of the 90° detector of all six satellites from the evening sector in the Northern Hemisphere. Again, we find that NOAA 16 measure a visibly lower flux than NOAA 18. We can also see a difference in the intensity of NOAA 18 compared to NOAA 19 in 2009. NOAA 16 seems to be more degraded in the P2 channel og the 90° detector than the other satellites.

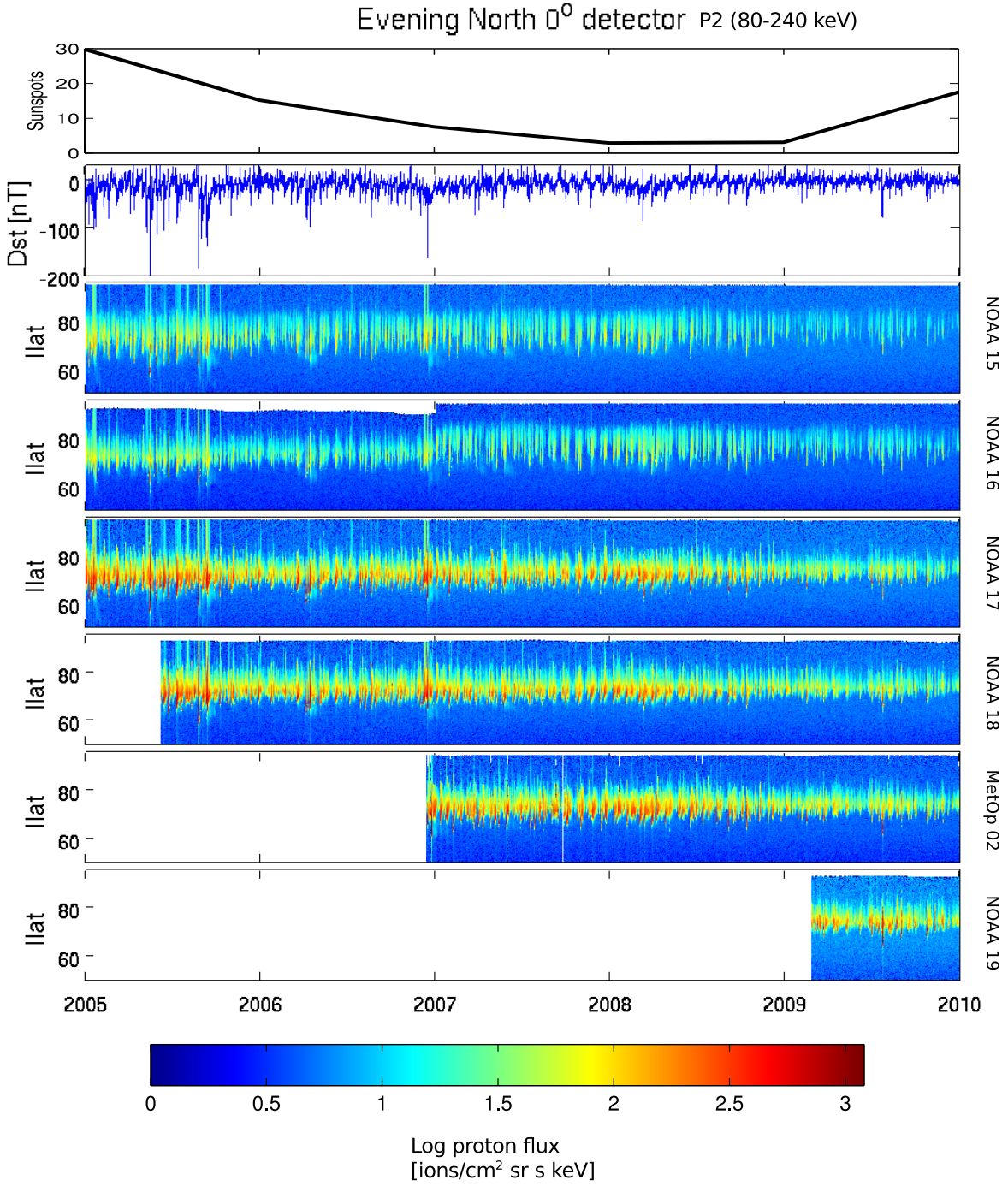

Figure 3.12: A comparison of flux intensity in the P2 channel of the 0° detector onboard NOAA 15, NOAA 16, NOAA 17, NOAA 18, MetOp 02 and NOAA 19 in the years 2005-2009. P2 measures protons with energies 80-240 keV.

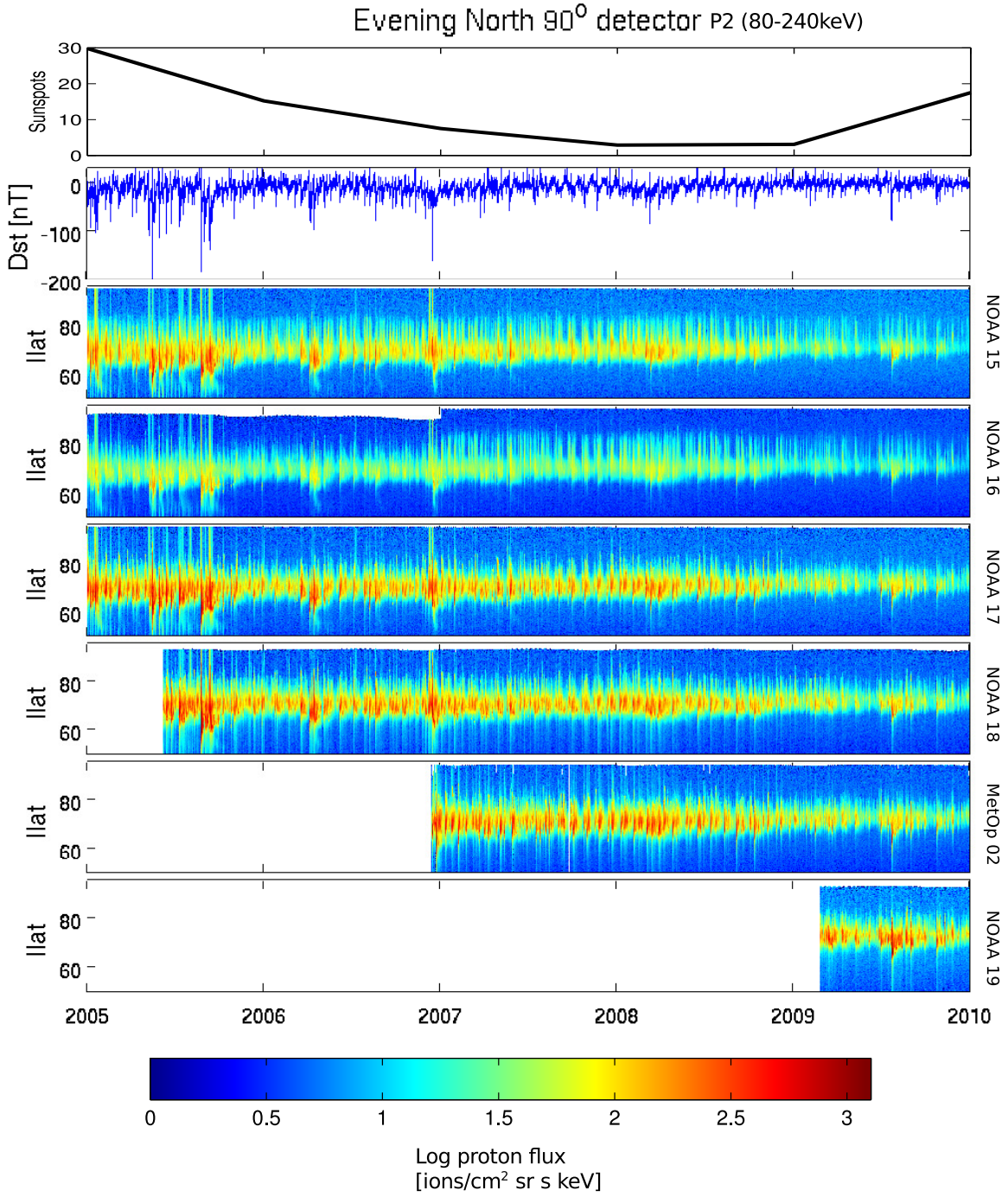

Figure 3.13: A comparison of flux intensity in the P2 channel of the 90° detector onboard NOAA 15, NOAA 16, NOAA 17, NOAA 18, MetOp 02 and NOAA 19 in the years 2005-2009. P2 measures protons with energies 80-240 keV.

Since there are three cases where an old satellite and a new satellite share orbital planes, we can inspect the degradation of these satellites a bit closer. Figure 3.14 shows averaged flux in the P1 channel of the 0° detector for the three pairs of satellites, for 150 days right after launch of the new satellite. The upper plot shows NOAA 16 vs NOAA 18, the middle plot shows NOAA 17 vs MetOp 02, and the lower plot shows NOAA 18 vs NOAA 19. The fluxes are averaged over one day, and for ILAT = 70° in the Northern evening sector, and plotted on logarithmic scale. In all three pairs, the measurements from new satellite is plotted in blue, and the old in black. The new satellite is found to measure more flux than the old satellite in all three cases.

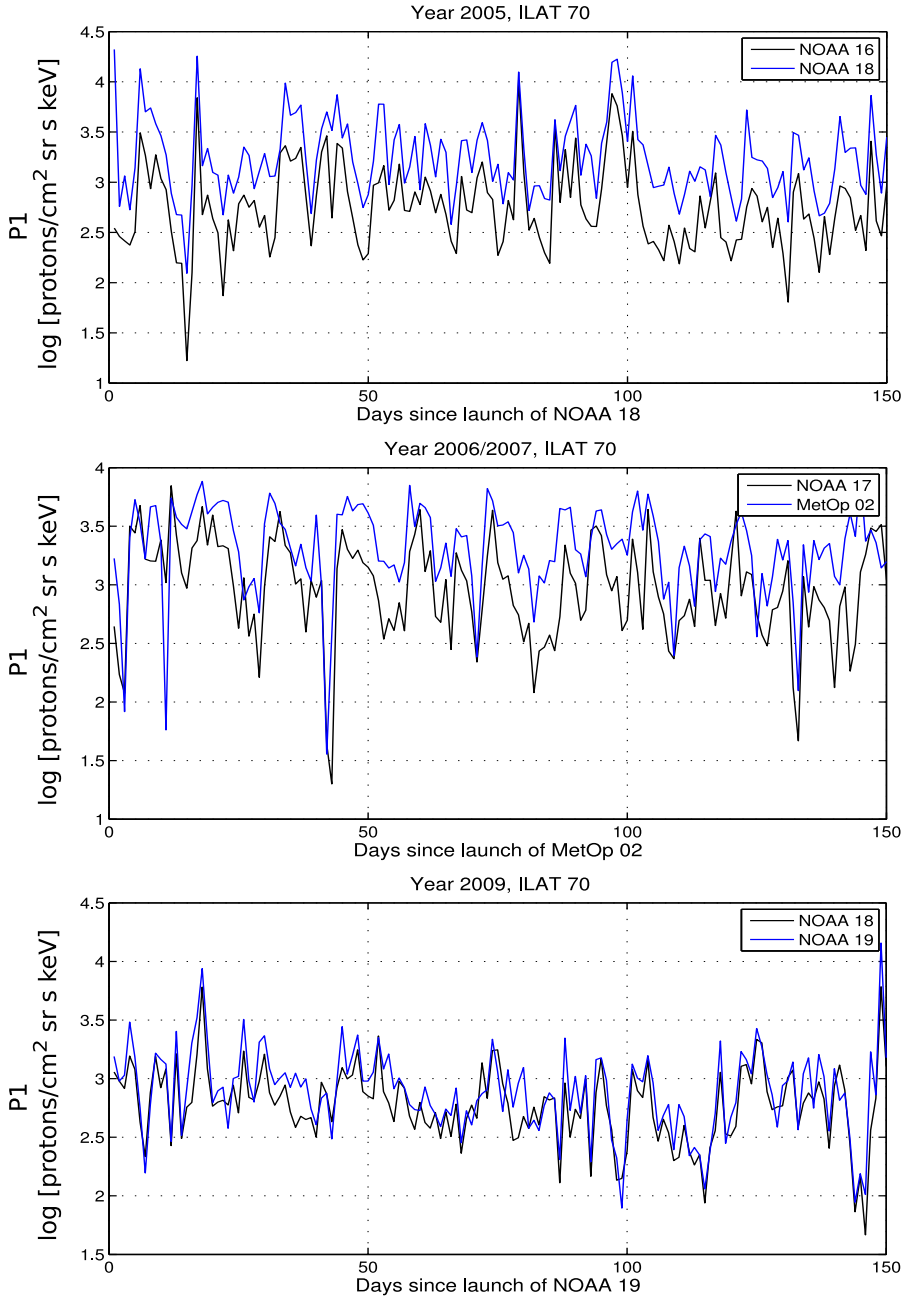

Figure 3.14: Daily average differential flux in the P1 channel of the 0° detector for newly launched satellites vs an old satellite in approximately the same MLT sector. The flux is measured at ILAT = 70° in the Evening Northern sector. Upper panel shows NOAA 16 and NOAA 18 for the first 150 days after launch of NOAA 18. The middle panel shows NOAA 17 and MetOp 02 for the first 150 days after the launch of MetOp 02. The lower panel shows NOAA 18 and NOAA 19 .

Chapter 4

Calibration

We have seen that several of the satellites display signs of degradation by visually inspecting the intensity of the measured flux. The degradation has previously been demonstrated by *Galand and Evans* [2000]. To our knowledge, the only attempt at recalibrating the whole NOAA dataset was done by *Asikainen and Mursula* [2011] and *Asikainen et al.* [2012]. Based on the level of particle flux exposure we expect the lower energy channels to degrade faster than the higher energy channels. The same argument holds for the 0°- and 90° detector as well as the temporal evolution of the degradation. The results by *Asikainen and Mursula* [2011] and *Asikainen et al.* [2012] do not meet these expectations. The α factors presented in the article sometimes show a larger degradation of the P2 channel than the P1 channel. In some cases, the P3 channel is found to have the largest α factor. The inability of *Asikainen and Mursula* [2011] and *Asikainen et al.* [2012] to fulfill our expectations was our motivation for developing an alternative method were we stray from the criteria of the satellites being located in the same space and time.

In this chapter we will first present previous work on calibration of the NOAA satellites. In the process of this thesis, two methods have been developed for calibrating the SEM-2 NOAA satellites. One method applies only for satellites orbiting in the same MLT sector. This method will be presented, and we will demonstrate why the method is not suitable for calibration of satellites in different MLT sectors. We then present the calibration results obtained by the use of this method in the three cases where one old and one new satellite share orbital planes in the launch year of the new satellite. Next, we present the second calibration method developed in this thesis, which can be used when satellites orbits in different MLT sectors. Finally, we present the results obtained by the second calibration method.

4.1 Previous Work

In this section we will present the method used by *Asikainen and Mursula* [2011] and *Asikainen et al.* [2012] to calibrate the NOAA satellites. This will be useful when we later describe the methods we have developed in this thesis, and to emphasize the

similarities and differences between our approach, and the *Asikainen and Mursula* [2011] and *Asikainen et al.* [2012] approach.

4.1.1 *Asikainen and Mursula* [2011]

The goal of the *Asikainen and Mursula* [2011] calibration was to estimate the factors by which the energy threshold of the MEPED instrument increase, and the temporal evolution of these factors. *Asikainen and Mursula* [2011] calibrated both SEM-1 and SEM-2 NOAA satellites.

The ideal situation would be to compare the energy spectrum measured by a degraded instrument to the true energy spectrum of the particle population where the satellite is located. As a proxy for the true energy spectrum, *Asikainen and Mursula* [2011] used the measurements of a newly launched satellite. To obtain a truthful comparison between degraded and undamaged detectors, the two satellites had to be as close as possible in space and time. Five criteria were set to identify conjunctions between satellites:

1. The conjunction must be within five months from the launch of the new satellite
2. The latitudinal and longitudinal separation (in geomagnetic coordinates) of the magnetic footprints (at 120 km altitude) of the two satellites must be less than 1°
3. The relative difference in L-values of the two satellites must be less than 10%
4. The particle count rates at the lowest energy channel must exceed one count per second
5. The time difference between two conjugate measurements (as defined by the above conditions) must be less than 30 s.

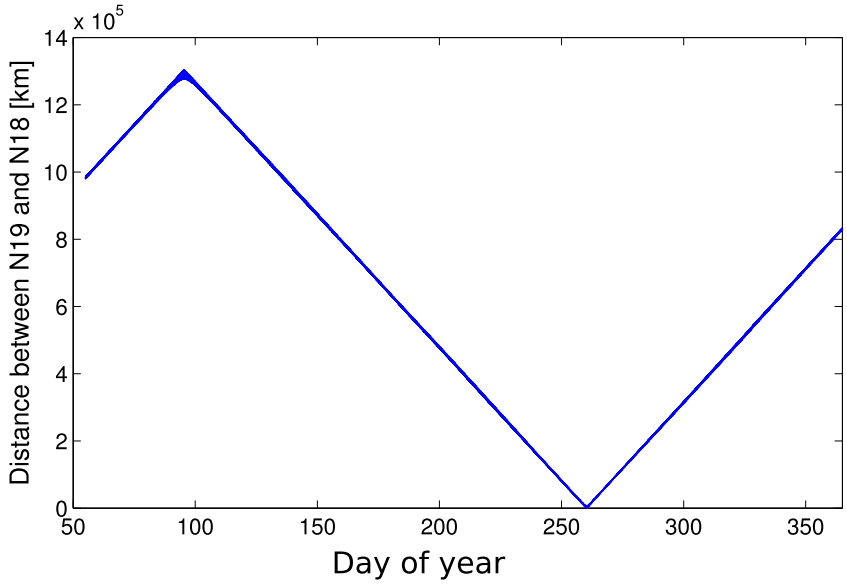

Figure 4.1: We have plotted the distance between NOAA 18 and NOAA 19 along the surface of a sphere at satellite altitude from February to December 2009. NOAA 19 is five months old around day of year 200. NOAA 18 and NOAA 19 did not fulfill the criteria set by [*Asikainen and Mursula*, 2011] within the five first months after launch of NOAA 19, even though they sample almost exactly the same region of space.

The criteria of being in the same space and time are hard to meet. Figure 4.1 shows the distance along the surface of a sphere between NOAA 18 and NOAA 19 vs day of year (DOY) in 2009 given in km at satellite altitude. Within the first five months after launch of NOAA 19, no conjunctions with NOAA 18 were identified by *Asikainen and Mursula* [2011]. The two satellites sample almost the exact same region of space (see Figure 3.2), but as Figure 4.1 implies, not at the same time.

Most of the identified conjunctions between any two satellites occurred inside the polar cap, where the fluxes of energetic particles are very low. However, when conjunctions were identified near the auroral zone, often ~ 100 comparisons of spectra could be made.

For an identified conjunction, the integral proton energy spectrum measured by the new satellite was found by:

$$F_n(E) = \int_E^\infty f_n(E')dE' \tag{4.1}$$

where the index n refers to 'new' satellite. $F_n(E)$ is the flux of protons observed above an energy E, and $f_n(E')$ is the flux observed with energy E'. Since the spectral form generally is unknown, a monotonic piecewise cubic hermite interpolating polynomial (PCHIP) was used to construct continuous spectra by interpolation between measure-

ments. The PCHIP maintains the monotonicity of the spectrum at all points, and its derivative is continuous.

The energy thresholds of all channels in the detector onboard the old satellite are assumed to have increased by factors α_i, where i designates the channel number. The integral flux for the old satellite can then be expressed as:

$$F_n(\alpha_i E_i) = \frac{1}{G_o} \sum_{k=i}^{k=5} N_{o,k} \tag{4.2}$$

where G_o is the geometrical factor of the instrument which converts the count rates to flux, and $N_{o,k}$ is the count rates. The index o refers to 'old' satellite, and k is the channel number.

To make the comparison, the flux $J(E_i)$ measured by the old satellite is found in the spectrum of the new satellite. The energy E corresponding to $J(E_i) = F_n(E)$ measured by the new satellite is taken as the new energy threshold of the old satellite.

$$F_n(E) = F_n(\alpha_i E_i) = \frac{1}{G_o} \sum_{k=i}^{k=5} N_{o,k} \tag{4.3}$$

where α_i is given by:

$$\alpha_i = \frac{E}{E_i} \tag{4.4}$$

To obtain the final α factor, the median of the distribution was used. The median is less sensitive to outliers than the mean, and thus gives more robust statistics. As the error of the distribution, the Median Absolute Deviation (MAD) is used. The MAD is defined as:

$$MAD(\alpha) = median\left(|\alpha - median(\alpha)|\right) \tag{4.5}$$

Figure 4.2 illustrates how an α factor is determined. The spectra in the figure are plotted based on averaged fluxes in the 0° detector. *Asikainen and Mursula* [2011] did not average the flux, however, the approach to determine α from two energy spectra is identical whether the fluxes are averaged or not. The flux is averaged over one day, and between ILAT 65-70°. Measurements from NOAA 18 and NOAA 16 on 07 June 2005 are used, and plotted as black crosses and filled circles, respectively. The PCHIP interpolants of the two satellites are drawn as a thin solid line for NOAA 18, and a thick dashed line for NOAA 16. We move horizontally from the integral flux in P1 of NOAA 16 (plotted at 30 keV, which is the nominal energy threshold for P1) until we find a point in the energy spectrum of NOAA 18 with equal flux. At this energy, we find the increased energy threshold of P1 in NOAA 16. α_1 can then be determined from Equation 4.4. The same procedure is repeated for all energy channels.

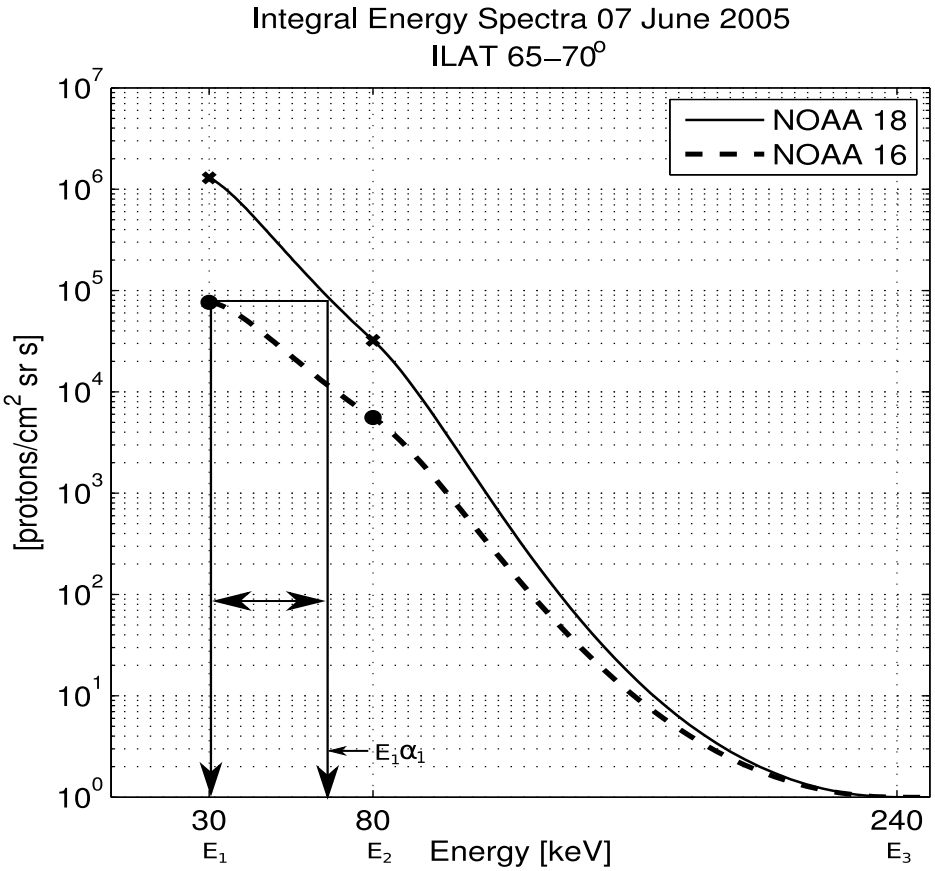

Figure 4.2: This plot shows the integral flux of NOAA 18 (as crosses) and NOAA 16 (as filled dots) averaged over 07 June 2005 and invariant latitude 65-70° in the Northern Night sector. The flux is plotted on logarithmic scale. The continuous integral spectra of the two satellites are made with PCHIP interpolation between the measurements. The spectrum of NOAA 18 is drawn as a thin solid line, and the spectrum of NOAA 16 is drawn as a thick dashed line. The increased energy threshold of the old satellite (here NOAA 16) is determined by finding the energy in the spectrum of the new satellite where the fluxes match. α is the ratio of the nominal energy threshold to the increased energy threshold. In this figure, we have shown how the α_1 factor of the P1 channel would be determined. The new energy threshold of the P1 channel in the 0° detector onboard NOAA 16 would be the energy $E_1\alpha_1$.

For each time a new satellite was launched, [*Asikainen and Mursula*, 2011] searched for conjunctions with older satellites in the five first months after launch, and calculated α factors every time a conjunction was found. The median α of the distribution was taken to be the α factor representative for that year. A drawback of this approach is that α factors can only be obtained for the years when a new satellite is launched.

When α factors were calculated for all years where conjunctions were identified, α was plotted vs time, and a visual inspection of the behavior of α vs time was used to determine a fit to the data. Figure 4.3 illustrates this for NOAA 15. Linear, 2nd and 3rd order polynomial, and PCHIP fits were used. For NOAA 18 and MetOp 02, *Asikainen and Mursula* [2011] could only determine α for one year during the lifetime of the satellites. When this was the case, a linear fit was used to find the temporal evolution of α, assuming $\alpha = 1$ in the launch year. The general increasing behavior of α with time was seen for all satellites, in P1, P2 and P3 of both detectors. Most of the α factors were found to stop increasing after a few years. However, for some cases it was found that α decreased in the years after 2006-2007, which is unrealistic. In the time evolution fitting, α factors were therefore set to constant levels from 2006 and onwards to avoid the decreasing behavior of α with time. The α factors presented in the article of *Asikainen and Mursula* [2011] were computed from the fits at the midpoints of every year the satellite was operational.

Figure 4.3 from *Asikainen and Mursula* [2011] article illustrates the temporal evolution of α factors found for the NOAA 15 P1, P2 and P3 channels. α factors for the 0° detector is shown as a blue squares, and for the 90° detector as red circles. In the P1 channel (left panel), the evolution of α in both detectors is estimated with a PCHIP interpolation between the median α factors found. The decrease seen in the α factor for the 0° detector is ignored and set to constant levels after 2007. In the P2 and P3 channel (middle and right panels, respectively), time evolution of α is found by 2nd order and linear fits. All the fitted curves are shown as solid lines.

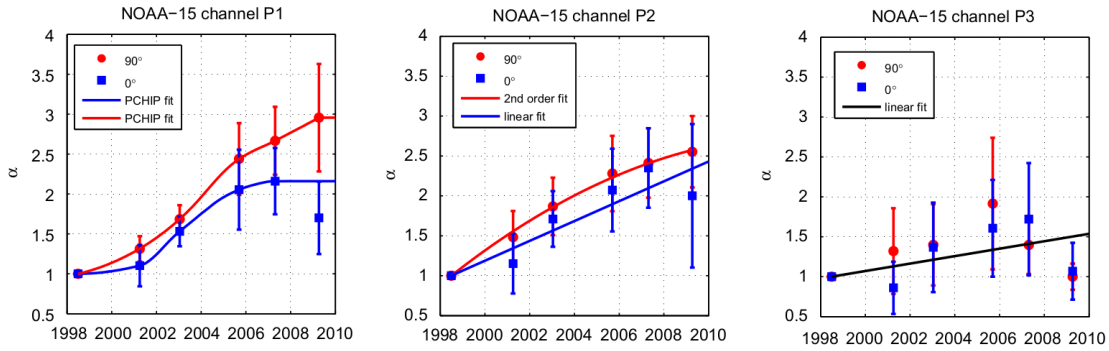

Figure 4.3: The α factors of NOAA 15 as a function of time for P1, P2 and P3 by *Asikainen and Mursula* [2011]. The blue squares represent the 0° detector and the red circles the 90° detector. The blue squares and red circles are median values of α factors found based on conjunctions in the respective years, and the errorbars are the MAD of the distribution. Different functions were fitted to the data, chosen by visual inspection. The fits are shown as solid lines, the blue lines are fits to the 0° detector, and the red lines are fits to the 90° detector. The figure is adopted from *Asikainen and Mursula* [2011].

We note that the MAD of the conjunction based α factors of NOAA 15 in Figure 4.3 is quite large. The same is seen for several of the other satellites presented in the same way in the article. The results presented by *Asikainen and Mursula* [2011] however, are presented without error. The average relative error of the α factors of all satellites and energy channels is found to be 20%.

Finally, the yearly α factors were used to calculate corrected count rates at the nominal energy of each energy channel.

4.1.2 *Asikainen et al.* [2012]

Asikainen et al. [2012] presented improved estimates for the effective energy thresholds in the three first energy channels of the 0° detector and the 90° detector for NOAA 06, NOAA 10, NOAA 12, NOAA 15, NOAA 16, NOAA 17, NOAA 18, and MetOp 02. NOAA 08 and NOAA 12 were corrected for increased electronic noise in the back detector. The estimates for the effective energy thresholds that were presented for NOAA 06 and NOAA 12 were based on daily averaged fluxes (too few conjunctions were identified for NOAA 06 and NOAA 12 in the article by *Asikainen and Mursula* [2011], and the α statistics for the two satellites were inadequate). *Asikainen et al.* [2012] argue that the satellites are expected to measure the same average flux levels over time scales of several days to months despite the fact that they do not sample the same MLT sector at exactly the same time.

Asikainen et al. [2012] exploited that all SEM-1 satellites (except NOAA 07) shared the same orbital plane. Daily averaged fluxes and energy spectra based on data from the Northern Hemisphere at $L \geq 2$ were computed and compared. NOAA 06 was compared to NOAA 10 in October 1986 right after the launch of NOAA 10. α factors were calculated with the same method as used by *Asikainen and Mursula* [2011], but with average integral energy spectra instead of instantaneous spectra. For the 0° detector of NOAA 12 daily averaged spectra were compared with daily averaged spectra from NOAA 15. The 90° detectors of NOAA 12 and NOAA 15 point in perpendicular directions (one of the differences between SEM-1 and SEM-2 satellites) and could therefore not be compared directly. The chosen solution was to use data from $L > 6$ during quiet conditions. During quiet times the isotropic boundary is expected to be at roughly ILAT = 65° at local midnight (which is approximately $L > 6$) [*Asikainen et al.*, 2010]. The isotropic boundary is the sharp border where the fluxes of energetic particles are the same at all pitch angles. Figure 4.4 shows a pass by NOAA 18 through the Northern Night sector, which for NOAA 18 is MLT 02-04. The thick black solid line is flux measured by the 0° detector, and the thin black dashed line is flux measured by the 90° detector (P1 channel in both detectors). The isotropic boundary is observed at ILAT $\approx$ 63 in this plot, where the fluxes in the two detectors are approximately equal. The trapping boundary marks the boundary between open and closed field lines, and is marked by the rightmost vertical line in Figure 4.4.

The flux is plotted on logarithmic scale vs ILAT.

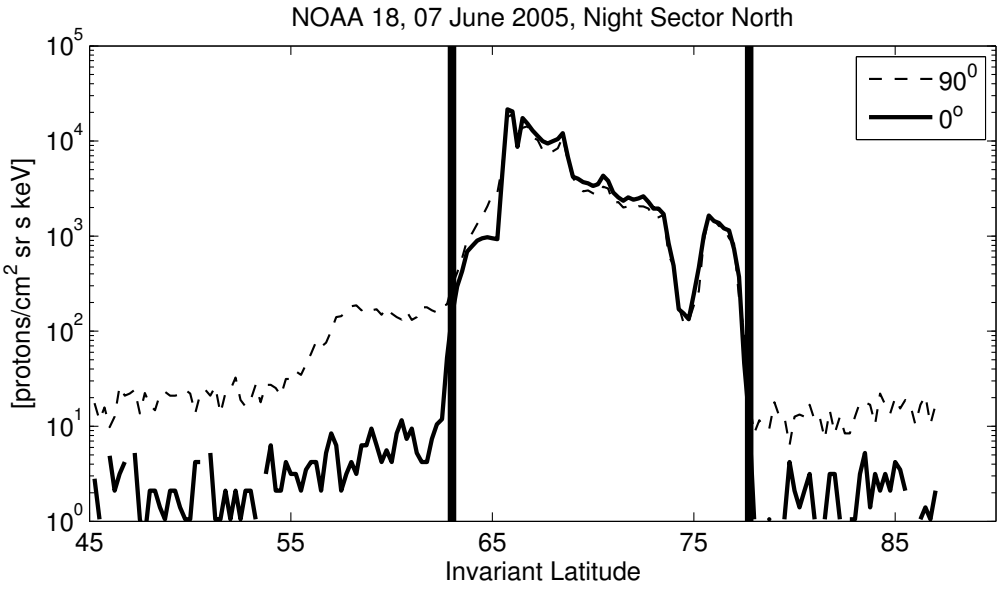

Figure 4.4: Differential flux vs ILAT for a pass through the evening sector in the Northern Hemisphere from NOAA 18. The black thick solid line is precipitating particles measured by the 0° detector. The thin black dashed line is mirroring particles measured by the 90° detector (data from P1 are used for both detectors). This pass is from 07 June 2005, the first day of data from NOAA 18. The isotropic boundary (IB) is marked with the vertical black line to the left, and the trapping boundary is marked with the vertical line to the right.

The rest of the NOAA satellites were not recalibrated by *Asikainen et al.* [2012], but the time evolution of the α factors were revised by estimating the total flux measured by the detectors through their lifetimes. The Ap index can be used as a crude proxy for the flux of energetic particles in the magnetosphere, and is thus roughly proportional to the total flux of particles that degrade the detector. The Ap index is an index that describes the level of activity in the magnetosphere, and it is derived from the Kp index. *Asikainen et al.* [2012] integrated the Ap index over the life time of each satellite, and the time evolution of the detector degradation could be approximated by the slope of the cumulative Ap index. It was shown that there was a close relationship between the cumulative Ap index and the temporal evolution of α factors.

4.2 Method 1: Calibrating Satellites at the Same MLT

In this section, we will present the first method for calibration of the NOAA satellites. This method can only be used for satellites that orbits in the same MLT sector. We will show why by applying the method to NOAA 15 using NOAA 19 in 2009, which fly in different MLT sectors. We will then present calibration results for the three cases where

a new satellite is launched into the orbit of an old satellite. These are NOAA 16 and NOAA 18 in 2005, NOAA 17 and MetOp 02 in 2006, and NOAA 18 and NOAA 19 in 2009.

4.2.1 Description of the Method

We use average measurements to construct energy spectra, similarly to what was done by *Asikainen et al.* [2012] for NOAA 06 and NOAA 12. Similarly, we also require that only data within the first five months after launch of a new satellite can be used, assuming the new detector to be undamaged that long. However, the method differs from the method by *Asikainen et al.* [2012] in several ways. *Asikainen et al.* [2012] constructed one daily energy spectrum based on all measurements in the Northern Hemisphere above L = 2 (L > 6 for the 90° detector of NOAA 12). The spectra constructed by *Asikainen et al.* [2012] were based on fluxes that were first corrected using α factors from *Asikainen and Mursula* [2011]. No corrections were done to to the dataset before it was used in this thesis. With method 1 in this thesis, we:

- Analyze data from the morning and evening (day/night) sectors separately.
- Divide each sector into nine invariant latitude intervals, and calculate α factors in each interval separately. Each ILAT interval is 5° wide in latitude.
- Analyze data from both hemispheres.

We divided the NOAA dataset into the 5° wide ILAT bins, illustrated in Figure 4.5. This makes 36 ILAT intervals in total for the four sectors. In each such interval, the flux measurements are averaged over one day, and over the 5° latitudes limited to the interval. Counts below 10 per second were removed as background noise, as the satellites always measures a few counts everywhere, including in the polar cap where it is unlikely to have high fluxes of energetic particles during quiet times. This background noise could have several sources, e.g. electronic noise, background radiation entering the detector from behind, etc. However, counts larger than 10 are well above this noise level.

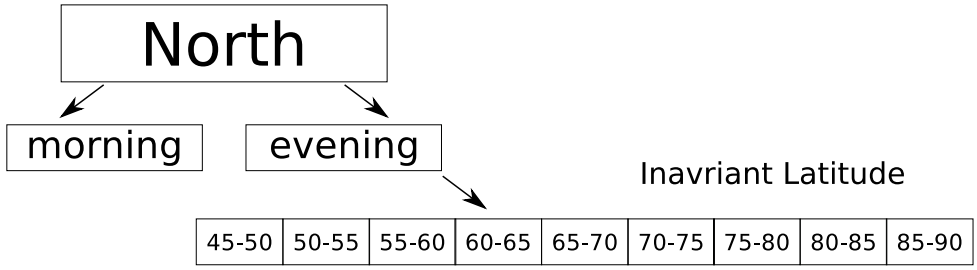

Figure 4.5: Illustration of how the NOAA data is binned into invariant latitude intervals. There are nine intervals per sector, making 36 bins in total for the four sectors.

In simple terms, the old satellite is compared to a newly launched satellite in each of the 36 ILAT intervals. Daily α factors are calculated based on integral energy spectra

with the same approach as used by *Asikainen and Mursula* [2011], described in section 4.1.1. In each of the ILAT intervals, the median α and the MAD of the distribution is found. We will later apply this method and analyze results from the four sectors separately. Through the analysis, we will show how the final α factors are obtained with this method.

Problems With Determining α for the P1 channel

Sometimes we find that the degraded satellite measures a greater integral flux in P1 than the new satellite. This situation implies that there is no point in the spectrum measured by the new satellite where the flux is equal to the degraded detector. Physically, these cases suggests that the new energy threshold for the P1 channel of the degraded detector is lower than the nominal energy threshold. All evidence point to this as unlikely [*Evans and Greer*, 2004; *Galand and Evans*, 2000; *Wüest et al.*, 2007]. However, since this is a statistical study where we use the median to represent our final α factors, we set $\alpha = 0.5$ when the problem arises. The choice to use 0.5 is arbitrary. The aim is to have an $\alpha < 1$ to weigh the median value somewhat lower. Fortunately, the median α is only dependent on how many times the situation arises, not on the actual ratio of the energy thresholds.

Why the method is not suitable when the satellites are at different MLT

To demonstrate why the first method is not suitable for calibration of satellites when they fly in different MLT, we apply the method to NOAA 15 in 2009, and try to calibrate NOAA 15 against NOAA 19 in the 5 month period right after launch of NOAA 19.

Figure 4.6 shows plots of the daily average flux in the 0° detector in P1, P2 and P3 for NOAA 15 (right) and NOAA 19 (left) in 2009. The logarithmic flux is plotted vs ILAT and day in the second, third and fourth panels, showing P1, P2, and P3 respectively. The uppermost plot in both columns display the Dst index for 2009. We can clearly see in the figure that NOAA 15 measures a smaller flux inside the proton oval than NOAA 19 in P1, P2, and P3. The Dst index shows that 2009 was a quiet year, with only one moderate storm in July. The maximum flux is found at ILAT $\approx 75°$ for NOAA 19, and at slightly higher latitudes for NOAA 15.

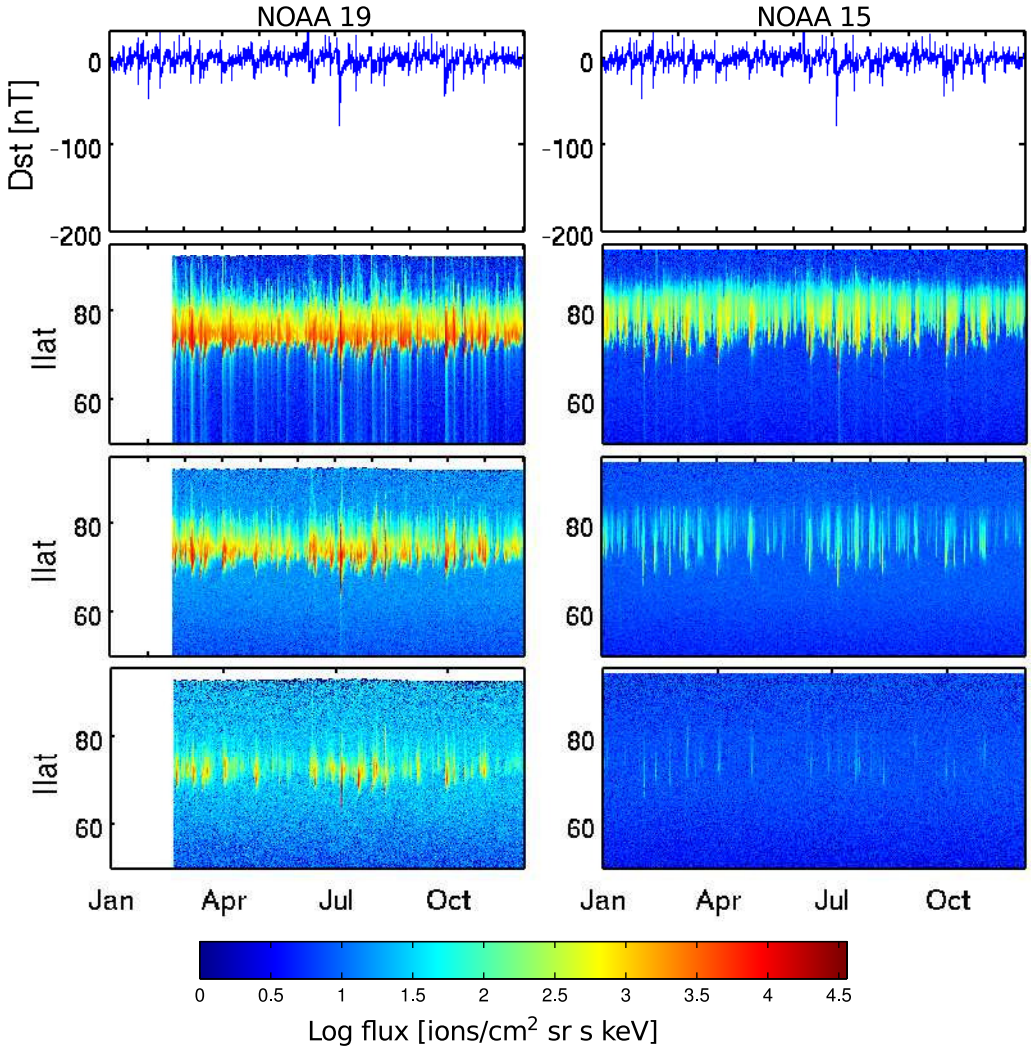

Figure 4.6: Differential proton flux measured by the 0° detector of NOAA 19 and NOAA 15 in 2009. All measurements are taken from the evening north sector, which is approximately MLT 02-04 and MLT 04-06 for NOAA 19 and NOAA 15 respectively. The top panel shows the Dst index for 2009. Second panel shows the daily average logarithmic flux intensity in P1 plotted vs ILAT and day. The third and fourth panel show the same for P2 and P3. The left column is measurements by NOAA 19, starting on 24 February 2009. The right column is measurements by NOAA 15. The Dst index shows that 2009 was a quiet year, with only one moderate storm in July. The maximum intensity of precipitating particles is found at ILAT $\approx 75°$ for NOAA 19, and at slightly higher latitudes for NOAA 15. Note the very low flux in the P3 channels of both satellites, and the considerably lower flux measured by NOAA 15 compared to NOAA 19.

NOAA 15 shows clear signs of degradation compared to NOAA 19. When we apply calibration method 1 in the Northern evening sector for NOAA 15 and NOAA 19, and use 150 days of data, we get the results for α shown in Figure 4.7. The upper panel shows how many satellite passes during the 150 days that were used to determine the α factors inside each of the nine intervals. All measurements for ILAT$< 60^\circ$ and ILAT$> 80^\circ$ were below the noise level, and therefore, no satellite passes could be used. In the middle panel, the mean separation of NOAA 19 and NOAA 15 in this sector is plotted, given in hours of MLT vs ILAT. The lower panel shows the median α for each interval, based on the daily α factors computed. The presented error is the median absolute deviation (MAD) of the α distribution inside each interval. Figure 4.7 shows that the comparison of two satellites that are separated in MLT gives a large variation of α with ILAT. This is not unexpected, because the flux intensity in the proton oval is known to have an MLT dependence [*Hardy et al.*, 1989].

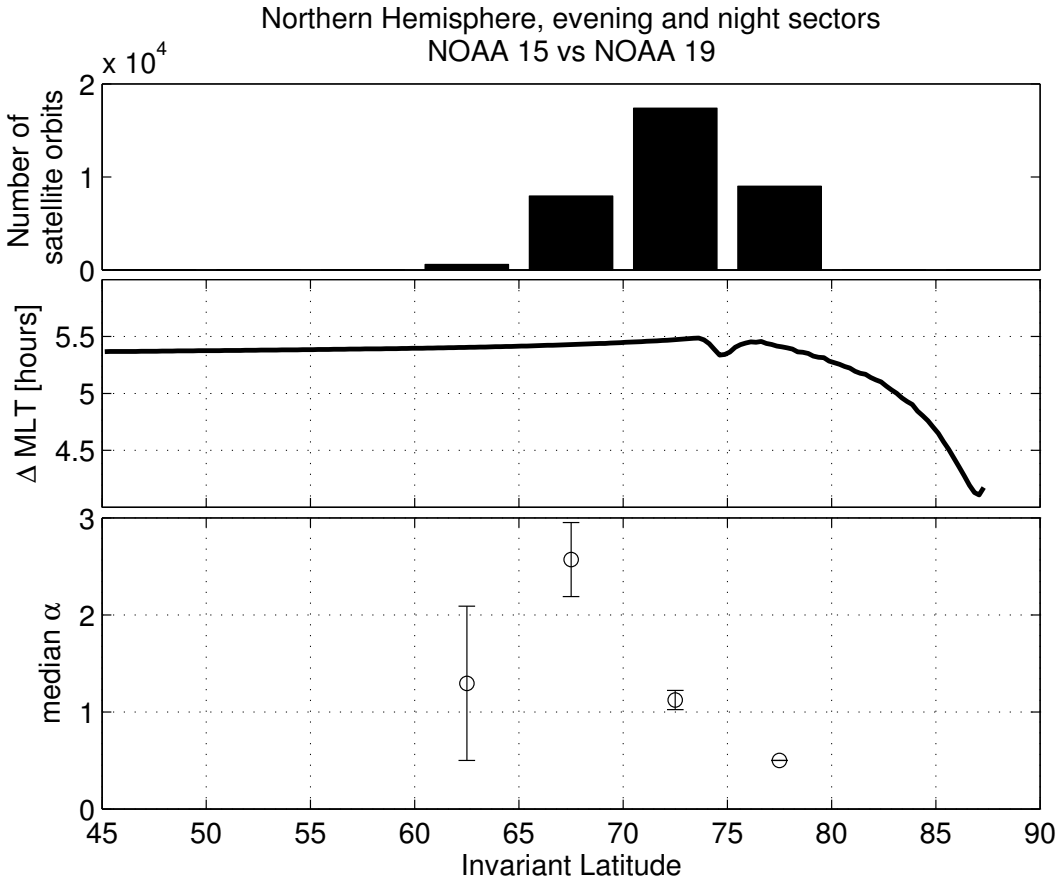

Figure 4.7: α factors in the evening sector of the Northern Hemisphere for NOAA 15 when it is compared with NOAA 19 (which is in the night sector) for 150 days after the launch of NOAA 19 in 2009. The upper panel shows the number of satellite orbits that could be used to determine α during the 150 days. The middle panel shows the mean separation of the two satellites in magnetic local time vs ILAT. The lower panel shows the median α in each interval. The errorbars is the MAD of the α distribution inside each ILAT interval.

In Figure 4.7, we find the median $\alpha \sim 2.5 \pm 0.5$ in the ILAT interval 65-70°. The large MAD reflects that the α factors vary much from day to day during the 150 days. Since the activity is low in 2009, 65-70° is at latitudes equatorward of the proton oval. However, when the precipitation reaches down to these latitudes, NOAA 19 always measures a larger flux than NOAA 15. This can be seen in Figure 4.6. The large flux in P2 of NOAA 19 relative to NOAA 15 would make the spectrum of NOAA 15 softer than the NOAA 19 spectrum, and thus give a large value for α in P1. The larger flux of NOAA 19 compared to NOAA 15 is most likely a combination of the degradation of NOAA 15, and that NOAA 19 is situated closer to midnight and NOAA 15 is closer

to dawn. At ILAT = 60-65°, the MAD is even larger, and only a small fraction of the satellite passes are used in this interval. The large MAD indicates a large day-to-day variation in the fluxes at these latitudes. At ILAT 75-80°, $\alpha = 0.5$, which shows that NOAA 15 measures a larger flux than NOAA 19, and the problem with determining α occurs (discussed in section 4.2.1). The median $\alpha \sim 1 \pm 0.1$ in the ILAT interval 70-75°. We find that in the ILAT interval 70-75° mainly two things are happening;

- NOAA 19 measures particles only in P1 $\Rightarrow \alpha \sim 1$
- NOAA 19 measures particles in P1 and P2 $\Rightarrow \alpha > 1$

The two cases are illustrated in Figure 4.8. The figure shows all integral spectra found for NOAA 19 during the 150 days in the top panel, plotted as blue lines. The measurements by NOAA 15 in the same period is plotted as red crosses in the same panel. In the two lower panels examples of each of the two types of spectra seen in NOAA 19 is plotted. In the left panel NOAA 19 measures zero flux in P2, resulting in $\alpha \approx 1$. In the right panel NOAA 19 measures significant flux in P2, resulting in $\alpha \approx 2$.

Consequently, even though Figure 4.6 shows that NOAA 15 is clearly degraded compared to NOAA 19 inside the proton oval, the use of method 1 finds $\alpha \sim 1$ for NOAA 15 at ILAT 70-75°. This is because the method fails to take into account the separation of the two satellites. The proton oval is located at different latitudes in the two MLT sectors where NOAA 19 and NOAA 15 fly, and we are therefore not comparing equivalent data when we limit the analysis to comparisons inside fixed ILAT intervals. Figure 4.9 illustrates the point. The lower left panel in the figure shows daily averaged differential flux measured by the P1 channel of the 0° detector onboard NOAA 15 at ILAT = 70° in the Northern evening sector, plotted vs the daily averaged differential flux measured by NOAA 19 at the same detector at the same latitude. The lower right panel shows the same, but with measurements from NOAA 18 vs NOAA 19. NOAA 18 and NOAA 19 fly in the same MLT, and we see that the measurements from NOAA 18 and NOAA 19 is well correlated at ILAT = 70°, with R = 0.89. NOAA 15 and NOAA 19 however, have a correlation coefficient of R = 0.69. The separation of two satellites in MLT makes it difficult to compare fluxes at fixed latitudes.

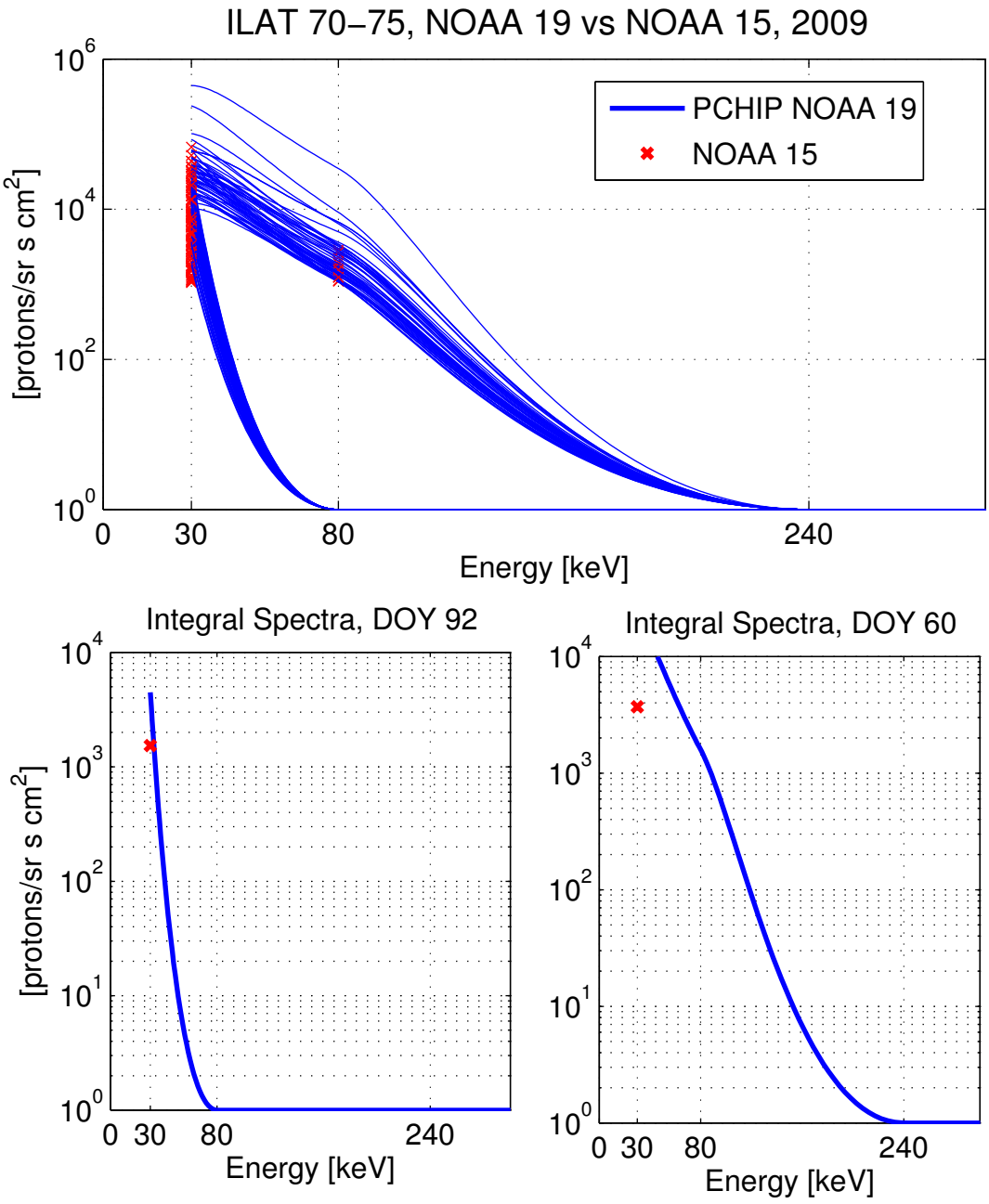

Figure 4.8: A closer look on the integral spectra of NOAA 19 in ILAT 70-75° during the 150 days period of 2009. In the upper panel, all 150 integral spectra of NOAA 19 is plotted with blue lines. The measurements by NOAA 15 are plotted as red crosses. Two different cases appear, one where NOAA 19 measures flux in P2, and one where NOAA 19 measures zero flux in P2. The two bottom plots show examples of the two cases. The left plot shows 02 April (day of year 92) in 2009, where NOAA 19 measures zero flux in P2. In this case $\alpha \approx 1$. The right plot shows 01 March (day of year 60) in 2009, where NOAA 19 measure flux in P2 (80-240 keV). In this case $\alpha \approx 2$.

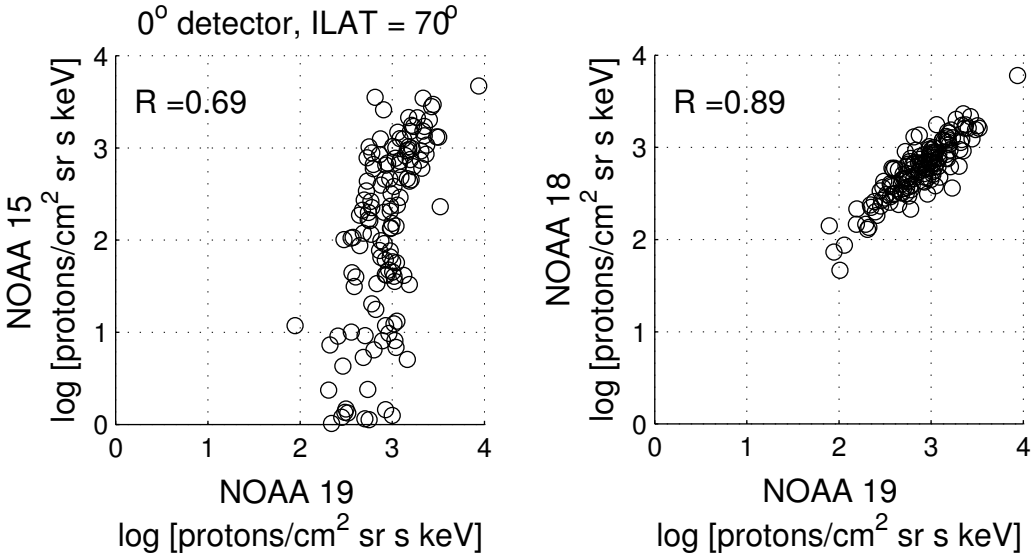

Figure 4.9: Left panel: Differential flux in the P1 channel in the 0° detector is averaged over one day. The average flux in the Evening/Night sector North at ILAT = 70° measured by NOAA 15 is plotted vs measurements by NOAA 19. The chosen period is 150 days long, starting with the first day of data of NOAA 19 in 2009. The correlation coefficient is R = 0.69 between NOAA 15 and NOAA 19. Right panel: Shows the same for NOAA 18 and NOAA 19. The correlation coefficient is R = 0.89. NOAA 19 and NOAA 18 flew in the same MLT sector in 2009. NOAA 15 was in a different MLT sector.

4.2.2 Results Using Method 1

In this section we apply method 1 to the three cases where an old satellite shares the same orbit as a newly launched satellite. These are NOAA 16 in 2005 when NOAA 18 was launched, NOAA 17 in 2006 when MetOp 02 was launched, and NOAA 18 in 2009 when NOAA 19 was launched. NOAA 16, 17 and 18 will be presented in ascending order. We will analyze each sector separately.

Calibration of NOAA 16 in 2005 using NOAA 18

This section will present a calibration of NOAA 16 in 2005 using NOAA 18. The first usable data from NOAA 18 is on 07 June 2005 (day of year 158). A period of 150 days from DOY 158 is used to obtain daily α factors. Figure 4.10 is a plot in magnetic local time vs invariant latitude showing the footprints of NOAA 16 (thin, solid magenta colored lines) and NOAA 18 (thick, dashed mustard colored lines) in 2005. The footprints of all orbits from the chosen day are plotted. The Northern Hemisphere is

shown to the left, and the Southern Hemisphere to the right in the figure. In 2005 the NOAA 16 and NOAA 18 dataset are divided into sectors in both hemispheres using the dawn-dusk meridian. This can be seen in Figure 4.10 as a discontinuity of the satellite footprints across this meridian. The evening sector is defined as 06 <MLT< 18 and morning sector as 18 <MLT< 06. In the figure, midnight is to the right and dusk at the bottom of the plot. In the following sections we will present and discuss each sector separately.

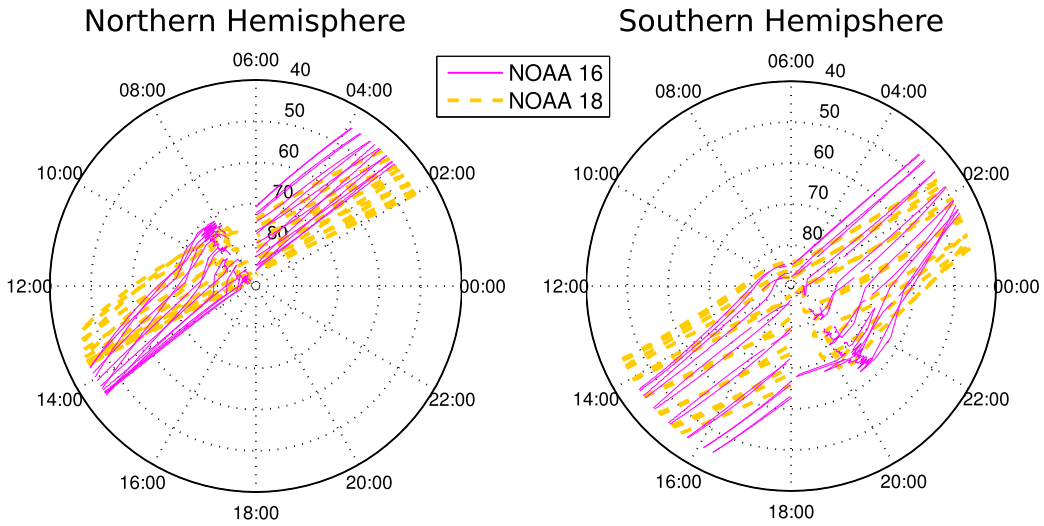

Figure 4.10: Plot showing the footprints of the 14-15 orbits of one day in 2005 for NOAA 16 as thin solid magenta colored lines, and NOAA 18 as thick dashed mustard colored lines. Data from NOAA 16 and NOAA 18 are divided into morning and evening sectors in the dawn-dusk meridian, as can be seen from the discontinuous lines here. The footprints are plotted in an MLT vs ILAT grid, and the perimeter is ILAT = 40° and each circle is 10° apart. Midnight is to the right and dusk is at the bottom of each plot.

Northern Hemisphere Night Sector

Figure 4.11 presents statistics on α factors for the Northern Hemisphere night sector. As can be seen in Figure 4.10 this is post-midnight (MLT $\sim$ 02 - 04) for NOAA 16 and NOAA 18 in 2005.

The top panel in Figure 4.11 is results for the 0° detector. The ILAT interval 45-90° has been divided in nine ILAT intervals as described in Chapter 4. The black circles are the median of all α factors obtained within each ILAT interval. The errorbars is the MAD of the distribution and thus give an indication of the spread of α within the interval. The second panel is a histogram displaying the number of satellite passes

through the ILAT interval used to determine the median α factor. The third and fourth panel show the same information for the 90° detector.

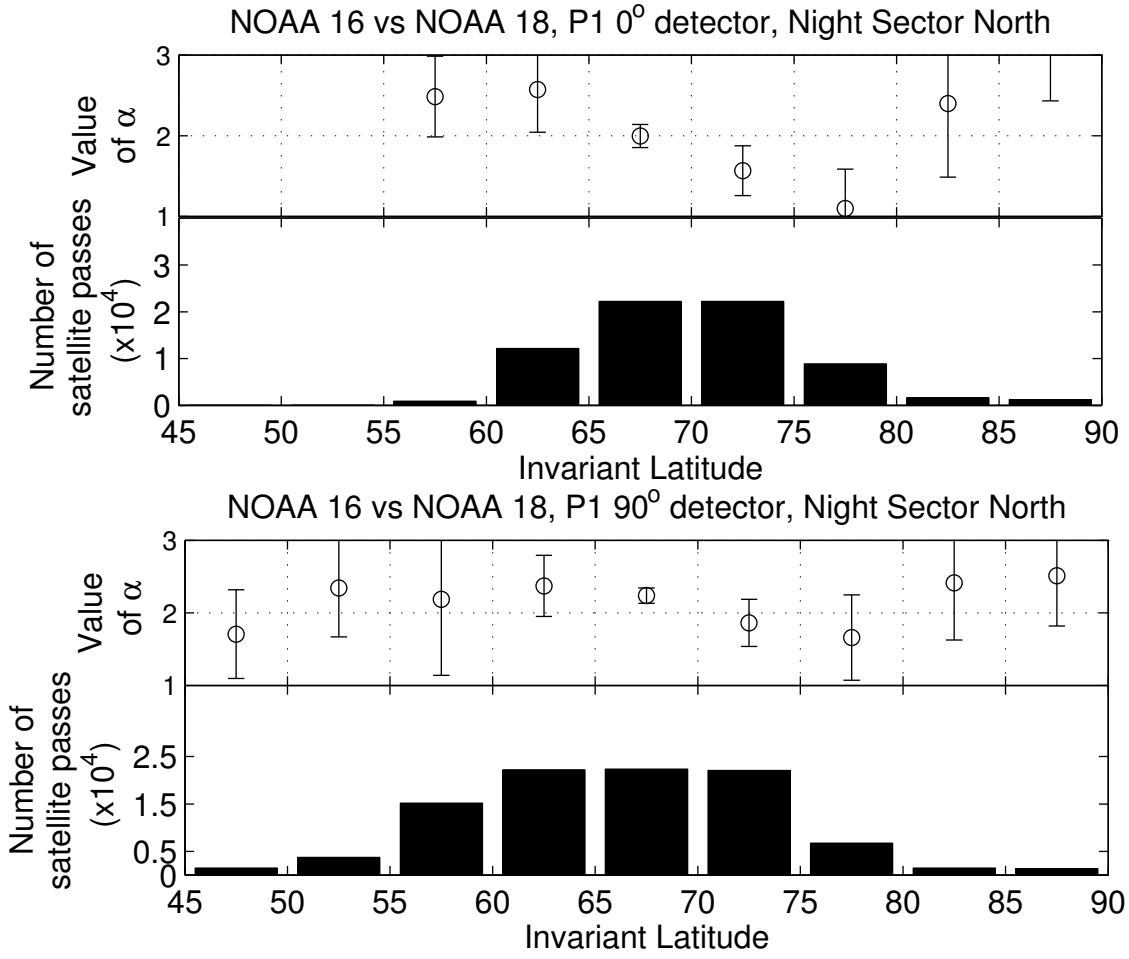

Figure 4.11: Statistics for the calibration of the P1 channel of NOAA 16 in the nightside Northern sector in 2005. The top panel shows the median of α factors inside each 5° wide ILAT interval. The error is the MAD of the distribution. The number of satellite passes through the ILAT interval used to determine the median α factor is shown in the histogram in the second panel. The two lower panels shows the same for the 90° detector.

The 0° detector There seems to be no simple relationship between α and ILAT in Figure 4.11. Ideally, the α factor should be constant and independent of ILAT, however, α is seen to vary with ILAT. In Figure 4.11, we observe the MAD to be high in all ILAT intervals except 65-70°. A large MAD indicates that α change considerably from day to day inside the ILAT interval. As seen in the histogram in the second panel of Figure 4.11, few α factors could be determined for ILAT<60 and ILAT>80, and no α factors for ILAT<55. At high and low latitudes, the 0° detector normally measures a low flux of particles (as seen in e.g. Figure 4.12 which is a plot of the mean flux measured by NOAA 18 in the Northern Hemisphere 31 December 2005). During quiet conditions these fluxes are below the noise threshold, and therefore not used for calibration. No discrimination between different levels of activity has been made is this part of the analysis, and therefore we expect to sometimes find a flux above the noise threshold at high and low latitudes.

ILAT 65-70° is almost always inside the isotropic zone, where the flux of particles is equal for all pitch-angles. The flux of average precipitation is high, and as indicated by the MAD in Figure 4.11, α does not vary much from day to day in this ILAT interval. However, equatorward and poleward of the isotropic zone the flux is several orders of magnitude lower than the maximum inside the isotropic zone. This can be observed in Figure 4.12. The isotropic zone is situated at latitudes from approximately 63° to 80° on the nightside of the Northern Hemisphere, which is to the left in the figure. 65-70° is thus situated completely within this zone. Equatorward and poleward of the isotropic zone, the precipitation is 3-4 orders of magnitude lower for this particular day. Figure 3.11 shows that 3-4 orders of magnitude lower flux at higher and lower latitudes than the maximum is a common situation. Equatorward and poleward of the isotropic zone, the daily mean flux is thus very sensitive for locally enhanced particle populations, as e.g. experienced when a satellite fly through a substorm. A substorm can last on time scales shorter than the orbital period of the NOAA satellites, and can therefore be experienced by one satellite and not the other, even though they fly in the same MLT sector.

At latitudes where the flux of average precipitation is always high, a substorm experienced by one satellite and not the other will alter the average flux to a lesser degree. Since the α factor is decided based on the integral energy spectrum of the satellites, the daily α factor will change considerably with time if the daily integral spectra varies with time. Inside the isotropic zone, the one day average is enough to make the spectra nearly constant over time. At higher and lower latitudes, the one day average is not sufficient to eliminate all time variation and is probably why the MAD is quite large.

For calibration, we need to find intervals where we can eliminate the time variability in the particle populations as a source of error in the α factor. For the night sector in the Northern Hemisphere the latitude interval 65-70° has the lowest MAD, and is therefore appears to be the best place to do the calibration in this sector.

The 90° detector Figure 4.11 shows large variation in α with ILAT for the 90° detector as well, which must be due to time variability in the particle population. The exception is ILAT 65-70°, where the flux is large, and the MAD is small. This interval

can be used for the calibration. ILAT intervals 60-65°, 65-70°, and 70-75° have the median α based on almost all the data from the 150 day calibration period. However, the MAD shows that the time variability is larger in intervals 60-65° and 70-75°, and these intervals are therefore excluded for calibration use.

Northern Hemisphere Daytime Sector

ILAT 60-70° is approximately where the maximum intensity in the night sector of the Northern Hemisphere is found. In the morning however, we find the maximum at higher latitudes. In Figure 4.12 the mean differential flux in P1 in the 0° detector is plotted vs invariant latitude for the Northern Hemisphere on 31 December 2005. From left to right the satellite passes through the night sector towards the day sector. On the nightside, the maximum flux measured by the 0° detector is found at ILAT ≈ 65-75°. On the dayside, the maximum is found at ILAT ≈ 70-80°.

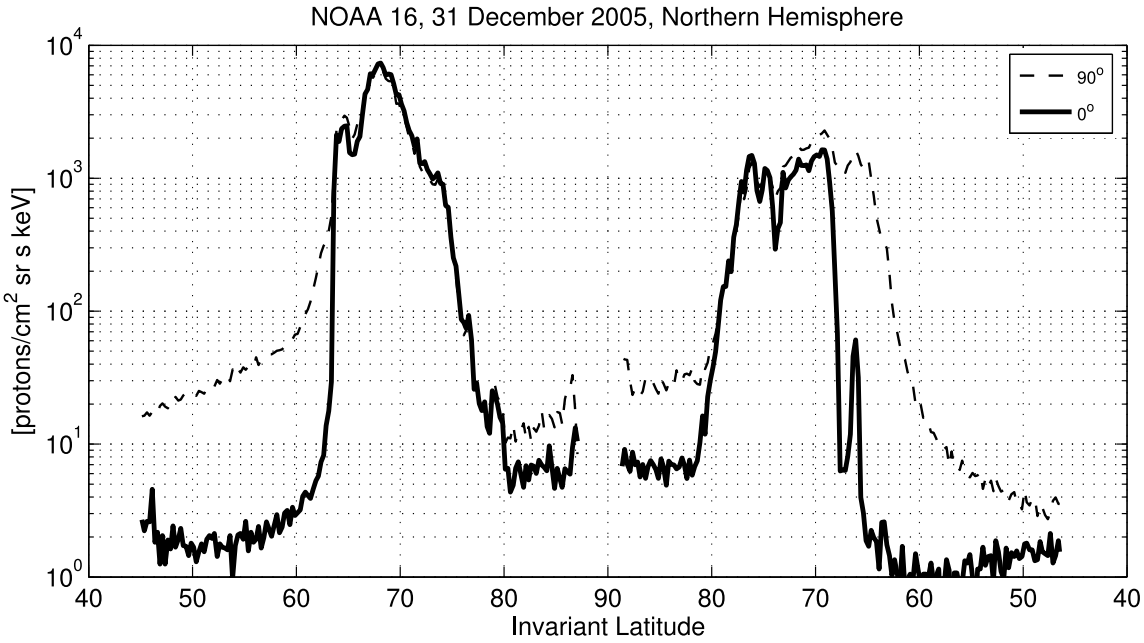

Figure 4.12: The mean differential flux measured in P1 in the 0° detector onboard NOAA 16 31 December 2005 in the Northern Hemisphere, plotted vs invariant latitude. The satellite passes from left to right, through the night sector and then through the daytime sector. The satellite does not cross directly over ILAT = 90° this day, and therefore the plot is not continuous.

Figure 4.13 shows the same as Figure 4.11 but for the Northern Hemisphere daytime sector. In 2005 NOAA 16 and NOAA 18 leave the daytime sector approximately at MLT 13-15, see Figure 4.10.

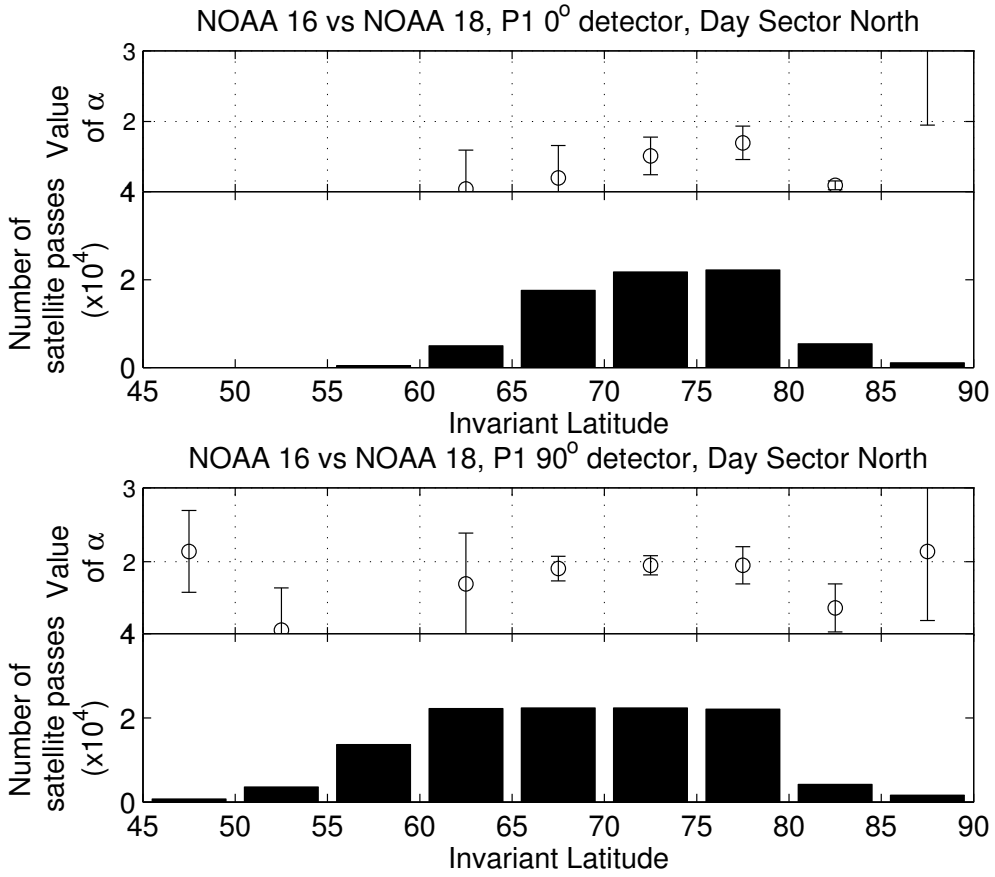

Figure 4.13: Statistics for the P1 channel of NOAA 16 in the daytime Northern sector. The top panel shows the median of α factors inside each 5° wide ILAT interval. The error is the MAD of the distribution. The number of satellite passes through the ILAT interval used to determine the median α factor is shown in the histogram in the second panel. The two lower panels shows the same for the 90° detector. Note that for ILAT 55-60 (both detectors) α could not be determined. The few events that had fluxes above the noise threshold in this ILAT interval had higher fluxes measured by NOAA 16 than NOAA 18, and thus gave $\alpha = 0.5$ as discussed in Section 4.2.1.

The 0° detector As for the night sector, we find that α vary with ILAT in the day sector. The largest number of α factors are calculated in regions where there are a substantial flux of precipitating particles, at invariant latitudes 65-80°. However, as discussed for the night sector, the MAD is the indicator of how much the α factor vary with time in each ILAT interval. We choose the interval with the largest number of *alpha* factors and the lowest MAD, for the 0° detector in the daytime sector, this is ILAT 75-80.

The 90° detector For the 90° detector, the ILAT intervals 65-70 and 70-75 both have a large number of α factors determined and low MAD. in these two intervals we find that the median α is approximately the same. When two intervals give the same median α with small MAD, we interpret this as a confirmation that the combination of large data used and low MAD gives a reliable value for α.

Southern Hemisphere

The statistics for the Southern Hemisphere are similar to the Northern Hemisphere, see Figures 4.14 and 4.15. The α factors vary with ILAT and with time, reflected in the large MAD in most of the ILAT intervals.

The smallest MAD is found near the isotropic zone for both sectors. Few α factors are obtained outside this region. For the 90° detector, we find the smallest MAD at invariant latitudes where the maximum flux of mirroring particles is found.

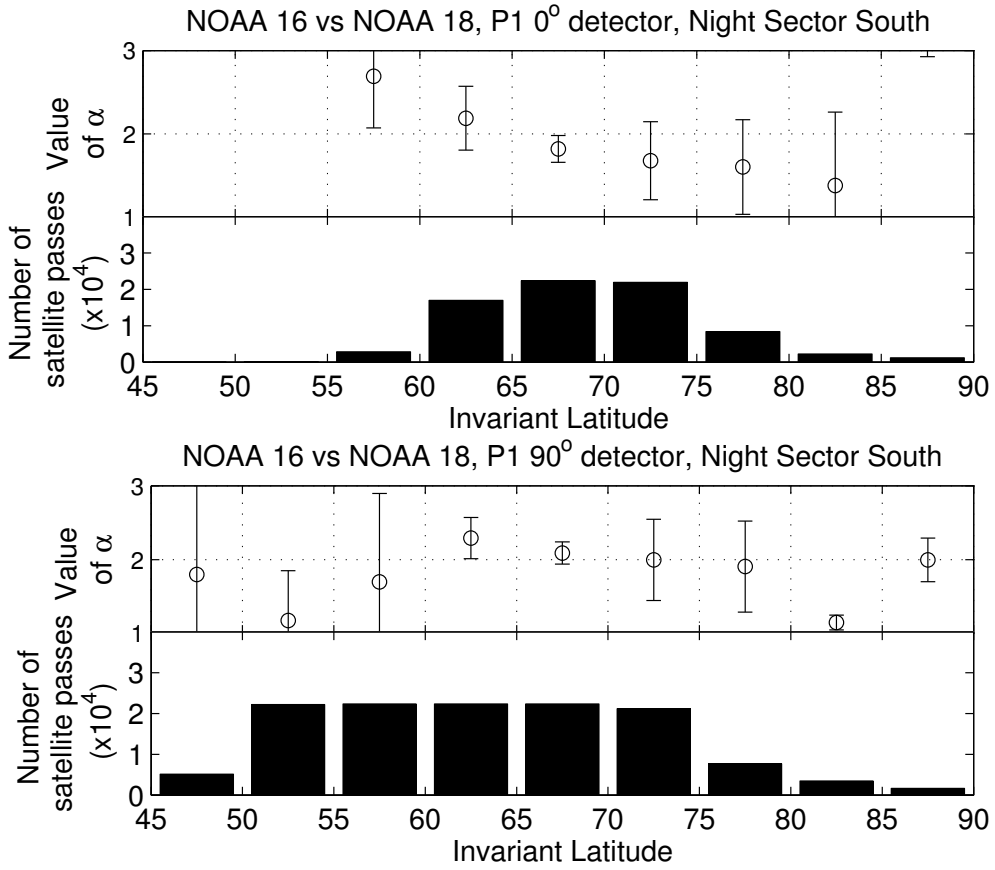

Figure 4.14: Statistics for the P1 channel of NOAA 16 in the Southern Hemisphere night sector. The top panel shows the median of α factors inside each 5° wide ILAT interval. The error is the MAD of the distribution. The number of satellite passes through the ILAT interval used to determine the median α factor is shown in the histogram in the second panel. The two lower panels show the same for the 90° detector.

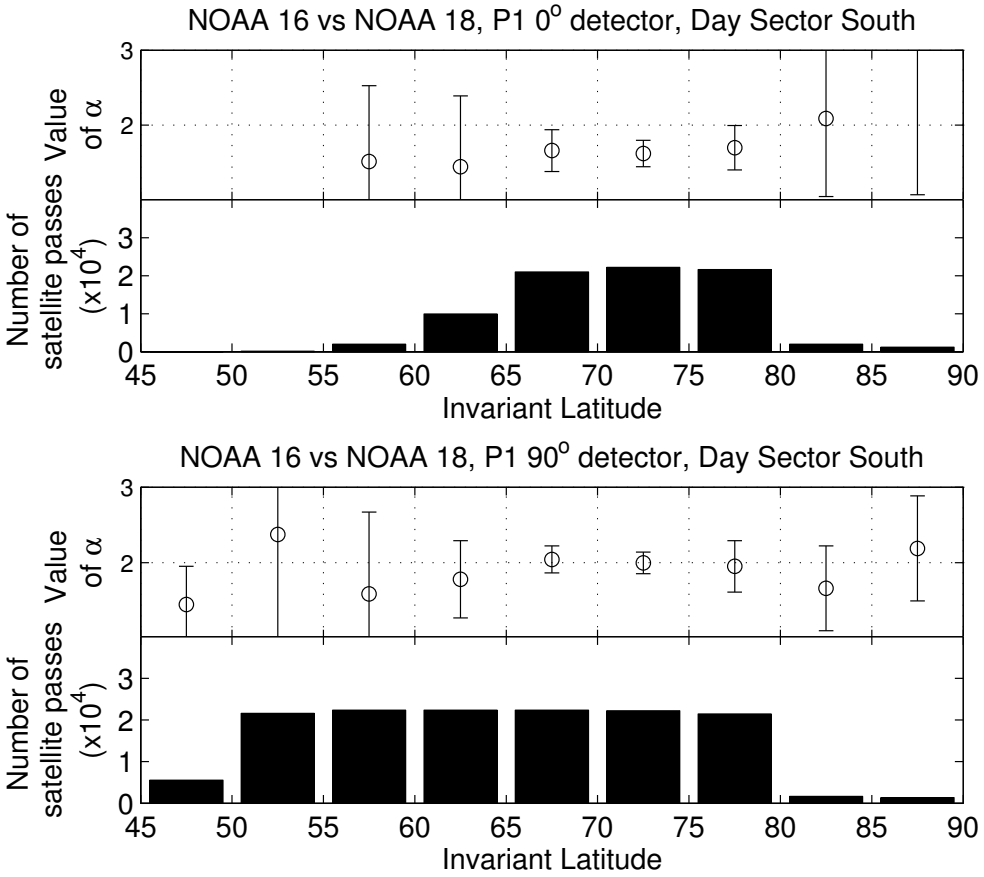

Figure 4.15: Statistics for the P1 channel of NOAA 16 in the Southern Hemisphere day sector. The top panel shows the median of α factors inside each 5° wide ILAT interval. The error is the MAD of the distribution. The number of satellite passes through the ILAT interval used to determine the median α factor is shown in the histogram in the second panel. The two lower panels show the same for the 90° detector.

Higher Energy Channels Generally, the same trends are seen for the higher energy channels as for P1. The α factors vary with ILAT and within intervals. There are fewer α factors calculated with increasing channel number, especially few in the 0° detector, because the spectra drop off with energy below the 10 count threshold.

P2 In the 0° detector the largest number of α factors are found in the ILAT interval 65-70° in all sectors except the Northern day sector, where they are divided almost equally in the two ILAT intervals 65-70° and 70-75° . In all sectors, the MAD is small in the interval with the largest number of α factors. Figure 4.16 shows the night sector in the Southern Hemisphere as an example. The MAD is large for ILAT >75°.

In the 90° detector the maximum number of α factors is reached in all sectors for at

least one of the nine ILAT intervals. The general trend visible in Figure 4.16 applies to all four sectors. In the Southern hemisphere, the median α in ILAT 65-70° has a large MAD as opposed to the MAD α between ILAT 65-70° in the Northern Hemisphere, which is small.

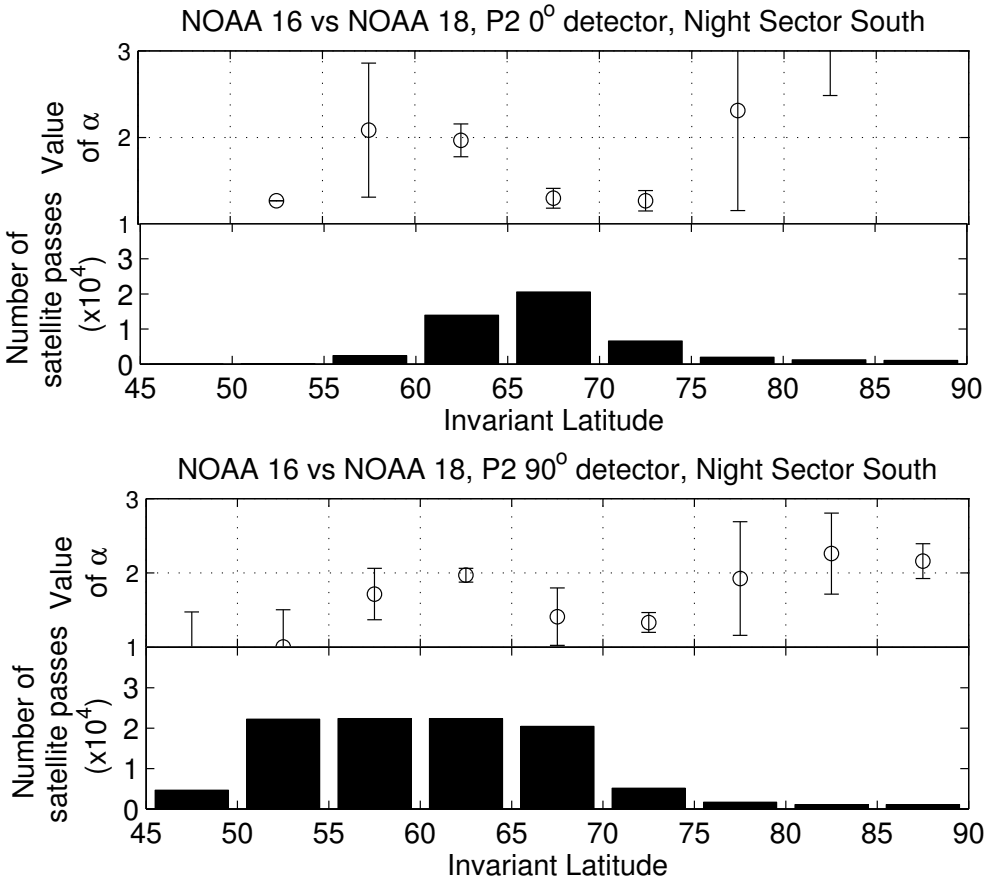

Figure 4.16: Statistics for the P2 channel of NOAA 16 in the Evening North sector. The top panel show the median of α factors inside each 5° wide ILAT interval. The error is the MAD of the distribution. The number of satellite passes through the ILAT interval used to determine the median α factor is shown in the histogram in the second panel. The two lower panels show the same for the 90° detector.

P3 The statistics for the third energy channel of the 0° detector is insufficient compared to P1 and P2, see Figure 4.17 with the Southern night sector as an example. However, in both hemispheres, we find the smallest MAD where we have determined the most α factors. On the nightside, this is ILAT 60-65° . On the dayside, it is ILAT 60-70°.

For the 90° detector the number of α factors determined is generally large also for

the P3 channel. We find the smallest MAD at ILAT 55-65° on the nightside, and 50-65° on the dayside.

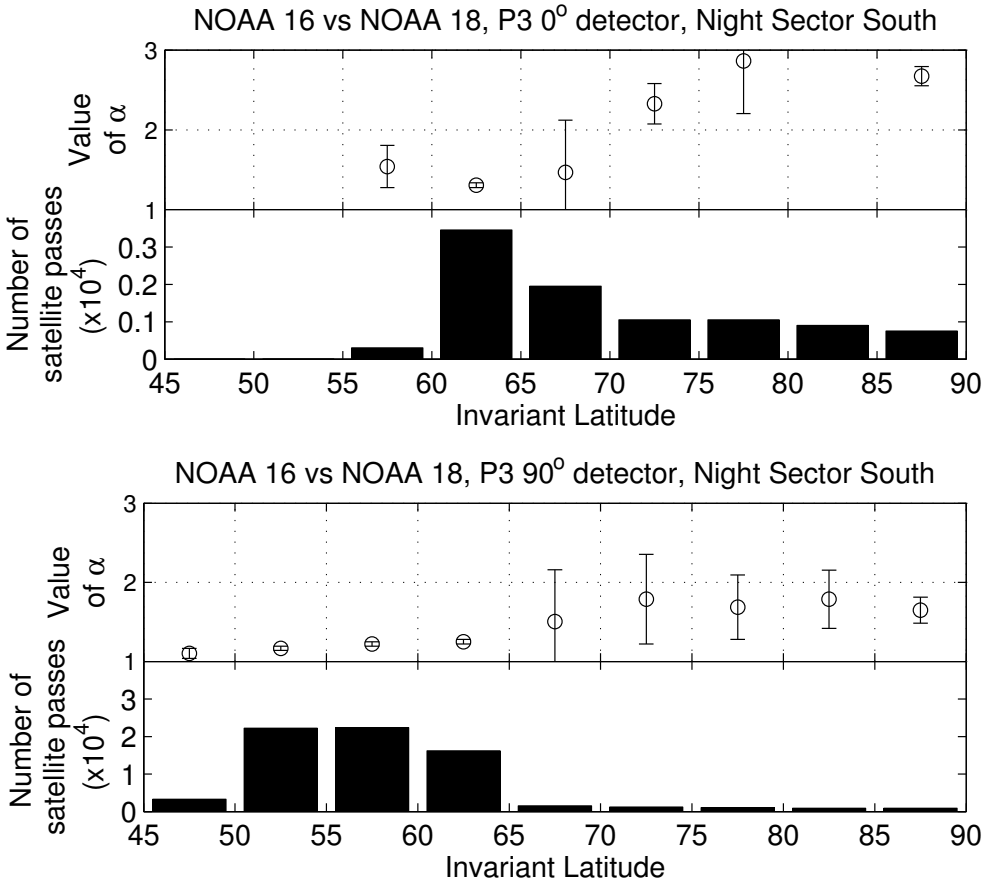

Figure 4.17: Statistics for the P3 channel of NOAA 16 in the Southern Hemisphere night sector. The top panel shows the median of α factors inside each 5° wide ILAT interval. The error is the MAD of the distribution. The number of satellite passes through the ILAT interval used to determine the median α factor is shown in the histogram in the second panel. The two lower panels show the same for the 90° detector.

P4 and P5 For P4 and P5 there are too few events to conclude anything about the degradation.

Summary of the Calibration of NOAA 16 in 2005

In this section, we present the α factors for NOAA 16 in 2005. These are summarized in Table 4.1 for both the α factors of the 0° detector, and the 90° detector. In the table we have listed the invariant latitude intervals where the combination of small MAD and large number of α factors determined in the 150 days period was found. All calculated

α factors in the chosen ILAT interval from each sector are combined, and the median of this distribution is presented as the α factors for NOAA 16 in 2005. The error in the α factor is the median absolute deviation of the distribution.

Table 4.1: The α factors for the 0° detector and the 90° detector onboard NOAA 16 in 2005. α factors for P1-P3 are presented. The table list which ILAT interval from the four sectors are used to calculate the median α factor. The intervals are chosen because they have the combination of large number of α factors determined, and small MAD in the respective sectors. The error presented is the Median Absolute Deviation of the total distribution when all factors from the four ILAT intervals are combined.

Calibration of NOAA 16 in 2005					
Energy Channel	Night North	Day North	Night South	Day South	$\alpha\pm$ MAD
P1 0°	65-70	70-75	65-70	70-75	1.8 ± 0.2
P2 0°	65-70	70-75	65-70	65-70	1.3 ± 0.1
P3 0°	60-65	65-70	60-65	60-65	1.3 ± 0.1
P1 90°	65-70	70-75	65-70	70-75	2.0 ± 0.2
P2 90°	65-70	65-70	60-65	60-65	1.8 ± 0.2
P3 90°	60-65	60-65	55-60	55-60	1.2 ± 0.1

Calibration of NOAA 17 in 2006/2007

In this section we will present α factors for NOAA 17 in 2007. NOAA 17 is calibrated against MetOp 02. MetOp 02 was launched late in 2006, and the first day with data is 03 December 2006. The calibration period is 150 days long, starting on 03 December 2006. Since most of the data in the calibration period is from 2007, we take the α factors obtained to be valid for 2007. Figure 4.18 is a plot in magnetic local time vs invariant latitude showing the footprints of MetOp 02 (thin, solid red colored lines) and NOAA 17 (thick, dashed cyan colored lines) in 2006. The footprints of all orbits of the chosen day are plotted. The Northern Hemisphere is shown to the left, and the Southern Hemisphere to the right in the figure. In 2006 the NOAA 17 and MetOp 02 dataset are divided into sectors in both hemispheres using the dawn-dusk meridian. The night sector is defined as 18 <MLT< 06 and day sector as 06 <MLT< 18. In Figure 4.18, midnight is to the right and dusk at the bottom of the plot.

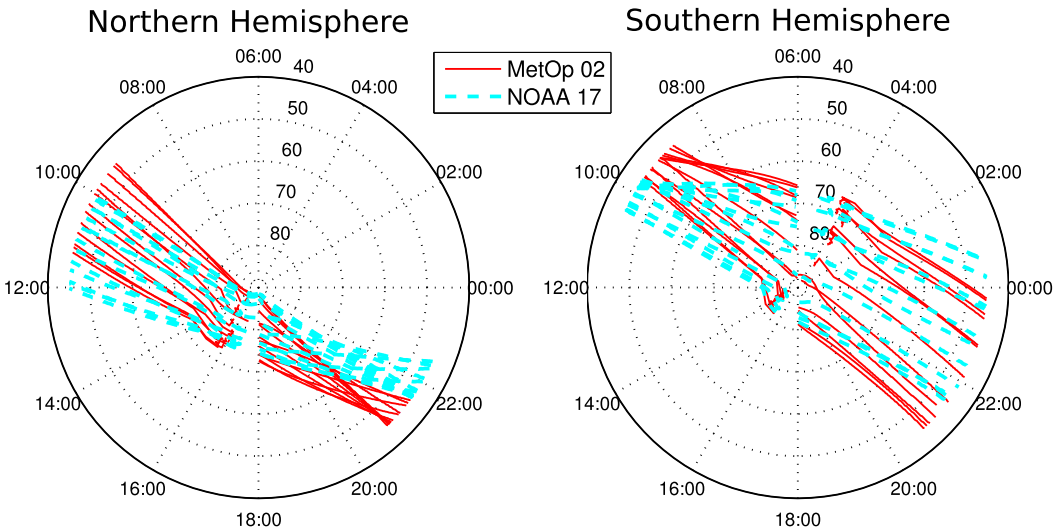

Figure 4.18: Plot showing the footprints of the 15 orbits of one day in 2006 for MetOp 02 as thin solid red colored lines, and NOAA 17 as thick dashed cyan colored lines. The data of NOAA 17 and MetOp 02 are divided into day and might sectors in the dawn-dusk meridian, as can be seen from the discontinuous lines here. The footprints are plotted in an MLT vs ILAT grid, and the perimeter is ILAT = 40° and each circle is 10° apart. Midnight is to the right and dusk at the bottom of each plot.

In the 150 day period, daily α factors are calculated using our statistical approach. The four sectors are analyzed separately. In each sector we identify the ILAT interval with the smallest MAD, combined with a large number of daily α factors determined. The identified intervals from each sector are combined, and the median of this distribution is taken as the final α factor. The MAD of the distribution is also found.

As for NOAA 16, we generally find the smallest MAD in the 0° detector at latitudes approximately 65-70° in the evening sectors, and at slightly higher latitudes in the morning sectors. Another common feature is that for the 90° detector, there are more α factors determined than for the 0° detector. In addition, the latitude intervals where the largest number of α determined are broader for the 90° detector. This is not unexpected, since the region where flux in the 90° detector is above the noise threshold is generally broader than the region of flux above the same threshold in the 0° detector. An example can be seen in Figure 4.4, showing how the isotropic zone is determined. The flux of particles in the 90° detector is generally larger than the flux in the 0° detector outside the isotropic zone, where the fluxes are approximately equal.

For the P3 channel of the 0° detector, the statistics from the two morning sectors are inadequate, and we do not include the α factors in the final distribution. To few daily α factors are determined in these sectors. The reason could be that there is too

low activity in 2007 to get high enough fluxes in the P3 channel in the morning sectors. The problem did not arise in 2005 for NOAA 16 because the activity in 2005 was higher than the activity in 2007. This can e.g. be seen in the Dst index and intrnsity of the fluxes in Figures 3.11, 3.12 and 3.13.

Table 4.2 present the α factors for NOAA 17 in 2007 found by method 1 of this thesis.

Table 4.2: The α factors for the 0° detector and the 90° detector onboard NOAA 17 in 2007. α factors for P1-P3 are presented. The table list which ILAT interval from the four sectors are used to calculate the median α factor. The intervals are chosen because they have the combination of large number of α factors determined, and small MAD in the respective sectors. The error presented is the Median Absolute Deviation of the total distribution when all factors from the four ILAT intervals are combined. For the P3 channel, the day sectors in both hemispheres had inadequate statistics, and were not included.

Calibration of NOAA 17 in 2007					
Energy Channel	Night North	Day North	Night South	Day South	$\alpha\pm$ MAD
P1 0°	65-70	70-75	65-70	75-80	1.4 ± 0.3
P2 0°	65-70	65-70	65-70	70-75	1.2 ± 0.1
P3 0°	65-70	-	60-65	-	1.2 ± 0.1
P1 90°	65-70	65-70	65-70	65-70	1.7 ± 0.2
P2 90°	65-70	65-70	65-70	65-70	1.3 ± 0.1
P3 90°	60-65	60-65	55-60	55-60	1.2 ± 0.1

Calibration of NOAA 18 in 2009

In this section we will present α factors for NOAA 18 in 2009. NOAA 18 is calibrated against NOAA 19. NOAA 19 was launched early in 2009, and the first day with data is 24 February 2009. The calibration period is 150 days long, starting on 24 February 2009. Figure 4.19 is a plot in magnetic local time vs invariant latitude showing the footprints of NOAA 19 (thin, solid blue colored lines) and NOAA 18 (thick, dashed mustard colored lines) in 2009. The footprints of all orbits of the chosen day are plotted. The Northern Hemisphere is shown to the left, and the Southern Hemisphere to the right in the figure. In 2009 the NOAA 19 and NOAA 18 dataset are divided into sectors in both hemispheres using the dawn-dusk meridian. The night sector is defined as 18 <MLT< 06 and day sector as 06 <MLT< 18. In Figure 4.19, midnight is to the right and dusk at the bottom of the plot.

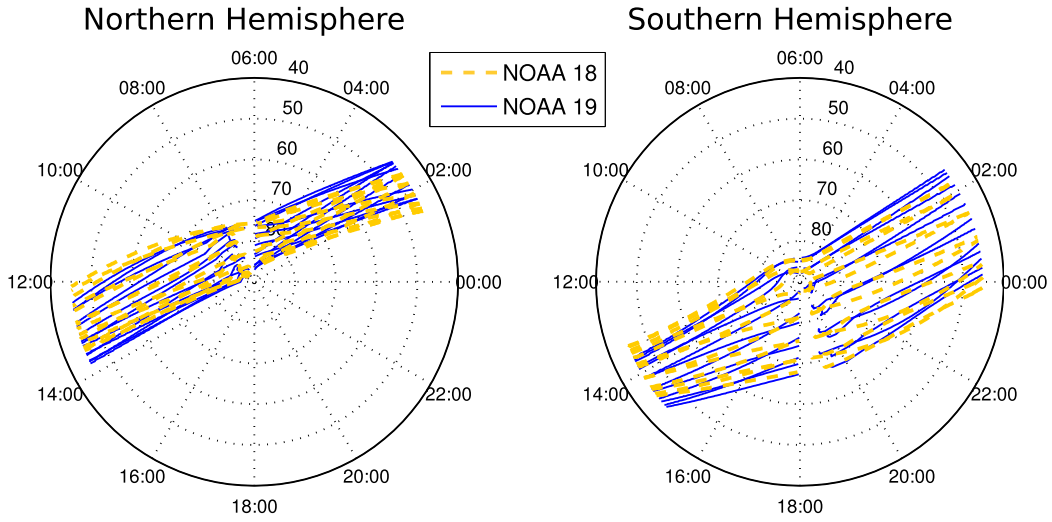

Figure 4.19: Plot showing the footprints of the 15 orbits of one day in 2009 for NOAA 19 as thin solid blue colored lines, and NOAA 18 as thick dashed mustard colored lines. The data of NOAA 19 and NOAA 18 are divided into day and might sectors in the dawn-dusk meridian, as can be seen from the discontinuous lines here. The footprints are plotted in an MLT vs ILAT grid, and the perimeter is ILAT = 40° and each circle is 10° apart. Midnight is to the right and dusk at the bottom of each plot.

In the 150 day period, daily α factors are calculated using our statistical approach. The four sectors are analyzed separately. In each sector we identify the ILAT interval with the smallest MAD, combined with a large number of daily α factors determined. The identified intervals from each sector are combined, and the median of this distribution is taken as the final α factor. The MAD of the distribution is also found. We have seen several times that the activity is very low in 2009, and the flux in the P3 and higher energy channels is minimal. Because of this the α factor of the P3 channel could not be determined with this method. The number of times α for the P3 channel could be determined in each sector was too low, or else it could never be determined.

The low activity in 2009 is also reflected in where we find the ILAT interval with the smallest MAD for th 0° detector. In the night sector of the Northern Hemisphere, the maximum number of α factors is found at ILAT 70-75° rather than 65-70°. In the day sector it is found at 75-80° rather than 70-75°.

Table 4.3 present the α factors for NOAA 18 in 2005 found by method 1 of this thesis.

Table 4.3: The α factors for the 0° detector and the 90° detector onboard NOAA 18 in 2009. α factors for P1 and P2 are presented. In the P3 channel, the statistics were unsatisfactory. The table list which ILAT interval from the four sectors are used to calculate the median α factor. The intervals are chosen because they have the combination of large number of α factors determined, and small MAD in the respective sectors. The error presented is the Median Absolute Deviation of the total distribution when all factors from the four ILAT intervals are combined.

Calibration of NOAA 18 in 2009					
Energy Channel	Night North	Day North	Night South	Day South	$\alpha\pm$ MAD
P1 0°	70-75	75-80	65-70	75-80	1.02 ± 0.10
P2 0°	65-70	75-80	65-70	65-70	1.08 ± 0.05
P1 90°	70-75	75-80	65-70	75-80	1.05 ± 0.13
P2 90°	65-70	65-70	65-70	65-70	1.11 ± 0.03

4.2.3 Summary of Method 1

The first method developed in this thesis can be used to calibrate satellites in the same MLT, and was applied to NOAA 16 in 2005, NOAA 17 in 2007 and NOAA 18 in 2009. The results are presented in Tables 4.1, 4.2, and 4.3.

We found that different ILAT intervals in the day and night sectors of the two hemispheres gave reliable results for the α factor. All α factors for the most reliable ILAT intervals were combined, and the median α from this distribution was found.

4.3 Method 2: Calibrating Satellites at Different MLT

Method 1 could be used only when two satellites were flying in the same sector, and one of them was newly launched. For the SEM-2 satellites, the first method could only calibrate NOAA 16 in 2005, NOAA 17 in 2007 and NOAA 18 in 2009. It could not be used to calibrate these three satellites in any other year, nor to calibrate the remaining satellites. We are therefore faced with two challenges:

- How can we calibrate satellites that fly in different MLTs?
- How can we determine the time evolution of α for each satellite?

Both the intensity and the energy input from particle precipitation is known to depend on MLT [*Hardy et al.*, 1985, 1989; *Hauge and Søraas*, 1975]. To calibrate satellites at different MLT, it requires knowledge of how the intensity of the particle flux varies with MLT. In addition, our approach this far has shown that the maximum intensity of the particle flux is located at different ILAT for different MLT. This is also found by several authors, e.g. *Hardy et al.* [1985, 1989]; *Hauge and Søraas* [1975]. The precipitation moves to lower latitudes during disturbed conditions, and is thus dependent on the level of geomagnetic activity. In our second calibration method, we will take the MLT

dependence and activity dependence of the particle flux and the location of the isotropic zone into account. The second method consists of two parts:

1. The construction of statistical maps of proton flux at different Kp.
2. The calibration of the NOAA satellites using the statistical maps.

4.3.1 Construction of Statistical Maps for Proton Flux

To get an overview of the statistical distribution of the proton precipitation during different activity levels, a rebinning of the NOAA data was done. For each new satellite, exactly one year of pristine data just after the launch of new satellites was rebinned in an MLT-ILAT grid. The choise to use one year of data was made to get enough data so that all activity levels would be covered. The degradation of the detectors is known to become prominent after 2-3 years [*Evans and Greer*, 2004], so the first year of data should not be severely affected by degradation.

The grid consisted of bins with an equal area, exactly 1° ILAT wide. The number of bins thus vary with latitude. For each pass through the morning and evening sector, the universal time of the satellite's entry into the sector was checked and sorted according to the activity level of the Kp index. What we want information about is where the auroral oval is located at different activity levels, and how the precipitation varies with latitude. To ensure that we keep the information about the auroral oval, we save only fluxes inside the isotropic zone. As was shown in Figure 4.4, this is where the ratio of flux from the 0° detector to the 90° detector is 1. For the pass through a sector, the isotropy zone was found according to the relation [*Asikainen et al.*, 2010]:

$$\left| \frac{I_0 - I_{90}}{I_0 + I_{90}} \right| < 0.15 \tag{4.6}$$

When this criterion was fulfilled, the data from both detectors was binned according to MLT and ILAT. The ratio of flux in the 0° detector to flux in the 90° detector was also saved. It was also recorded how many times the criterion was fulfilled inside each bin. Figure 4.20 shows the number of events for each Kp in the Northern Hemisphere, where an event is the binning of data in a particular bin at a given Kp. Events in the Southern Hemisphere are shown in Figure 4.21.

The events displayed in Figures 4.20 and 4.21 are collected in 1998-1999 (NOAA 15), 2001-2002 (NOAA 16), 2002-2003 (NOAA 17), 2005-2006 (NOAA 18), 2006-2007 (MetOp 02), and 2009-2010 (NOAA 19). That is, the data is obtained in different periods through the solar cycle. Figures 4.20 and 4.21 show that we have very good coverage in the post-midnight post-noon sector for Kp 0-3 in both hemispheres. NOAA 19 orbits in this sector, and as shown in Figure 4.6 the year 2009 was exceptionally quiet. This could explain why NOAA 19 data contribute more to the statistics for low Kp. However, NOAA 18 and NOAA 16 fly in this sector in the launch year of the satellites as well, and the sector is thus very well covered. Data from the other satellites seems to be more evenly distributed over Kp 0-4, which was found by *Rangarajan and Iyemori* [1997] to be the activity level 80% of the time. *Rangarajan and Iyemori* [1997]

found Kp> 6 to occur less than 4% of the time, which is well reflected in the three plots in the last row of Figures 4.20 and 4.21.

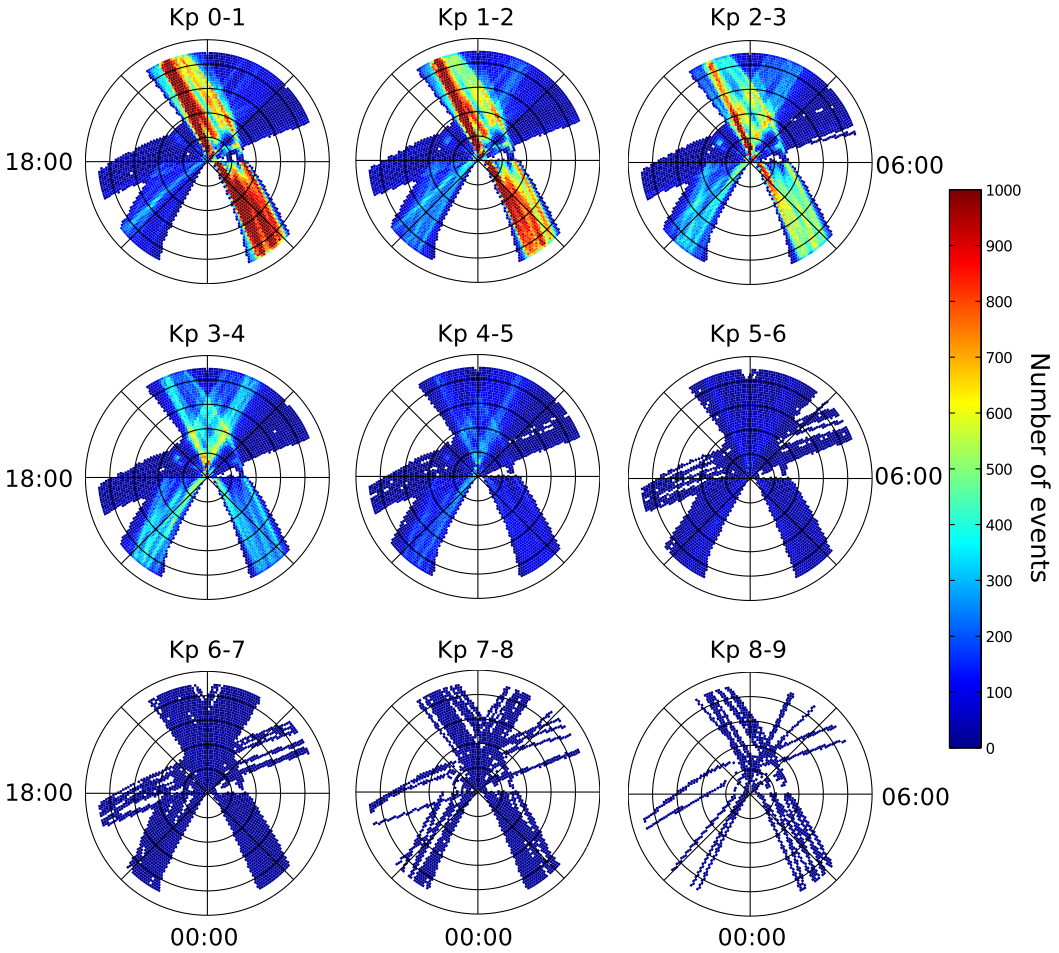

Figure 4.20: Distribution of events in MLT vs ILAT grid for the Northern Hemisphere. For the first year after launch, data from all satellites are sorted according to Kp and rebinned. The upper row shows Kp 0-1, 1-2 and 2-3. The middle row shows Kp 3-4, 4-5 and 5-6. The bottom row shows Kp 6-7, 7-8 and 8-9. An event is a measurement by a satellite inside a bin at the given Kp.

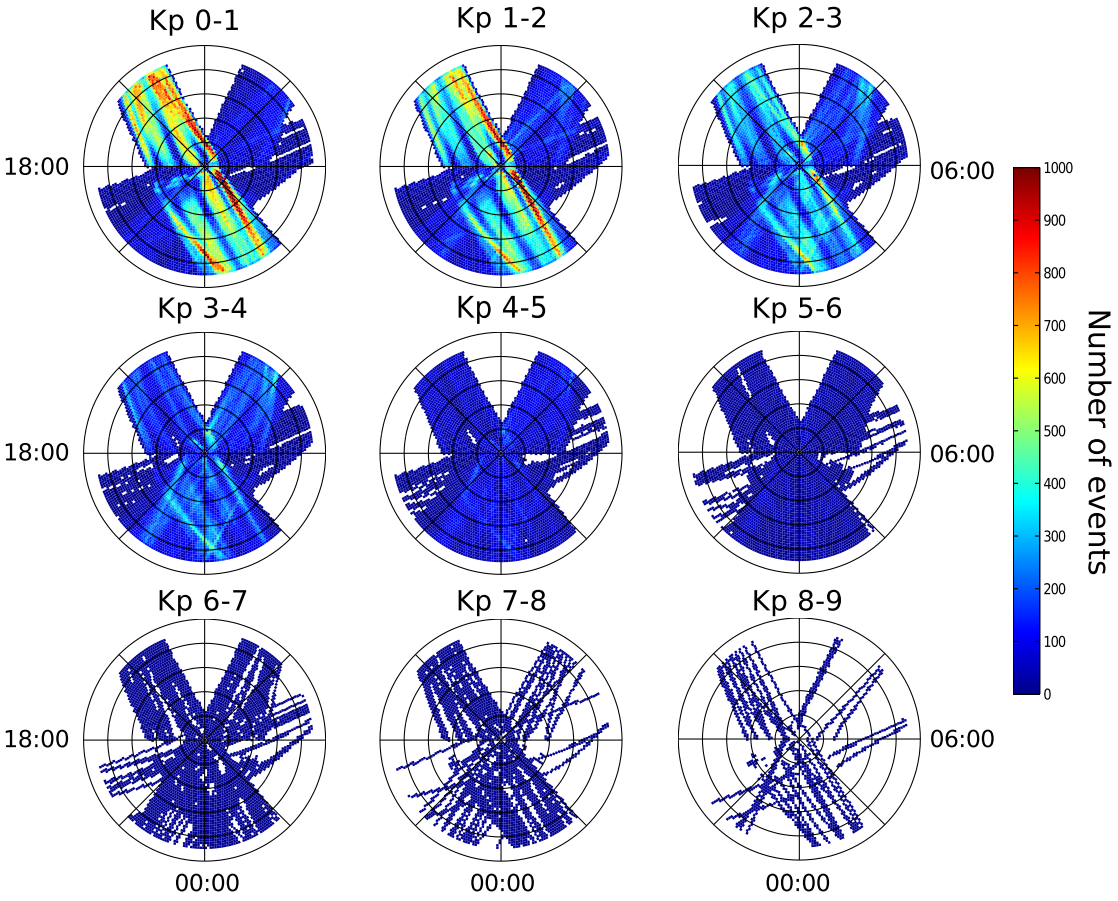

Figure 4.21: Distribution of events in MLT vs ILAT grid for the Southern Hemisphere. For the first year after launch, data from all satellites are sorted according to Kp and rebinned. The upper row shows Kp 0-1, 1-2 and 2-3. The middle row shows Kp 3-4, 4-5 and 5-6. The bottom row shows Kp 6-7, 7-8 and 8-9. An event is a measurement by a satellite inside a bin at the given Kp.

To get a better coverage and statistics, we add together the results obtained in the Northern and the Southern Hemisphere. The fluxes from both hemispheres were summed inside each bin, then divided by the number of events in both hemispheres. The expected pattern is seen in for precipitating particles (0° detector) in Figure 4.22 and for mirroring particles (90° detector) in Figure 4.23. When Kp increases, the flux increases, and the location of maximum flux moves to lower latitudes. The six satellites cover almost the entire proton oval when both hemispheres are combined. Even though we have added together events from the Northern and Southern Hemispheres, we see from Figures 4.22 and 4.23 that the coverage for Kp>5 is too sparse to use. However, according to *Rangarajan and Iyemori* [1997] we only exclude $\sim 20\%$ of the data by only using Kp<4.

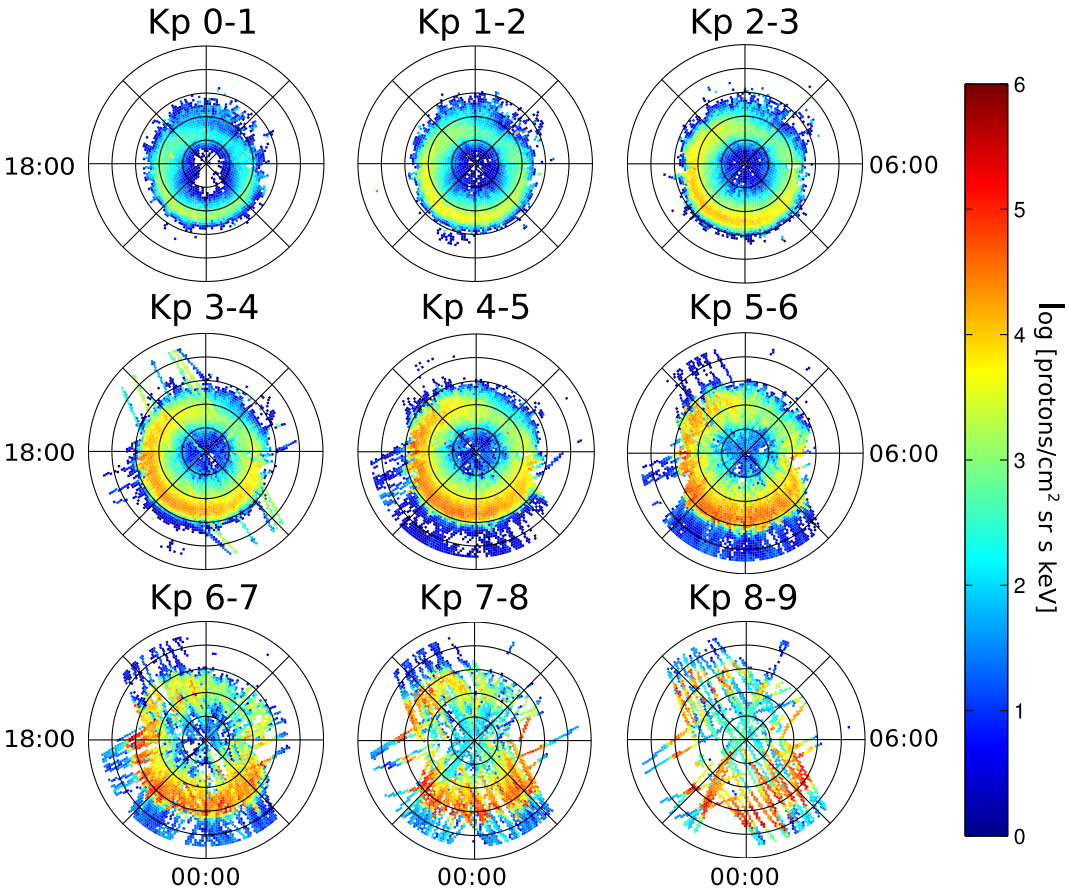

Figure 4.22: The flux of precipitating protons (0° detector) with 30-80 keV energy from both hemispheres, sorted according to Kp. The upper row shows Kp 0-1, 1-2 and 2-3. The middle row shows Kp 3-4, 4-5 and 5-6. The bottom row shows Kp 6-7, 7-8 and 8-9. Noon is at the top of the plots, and dawn is to the right.

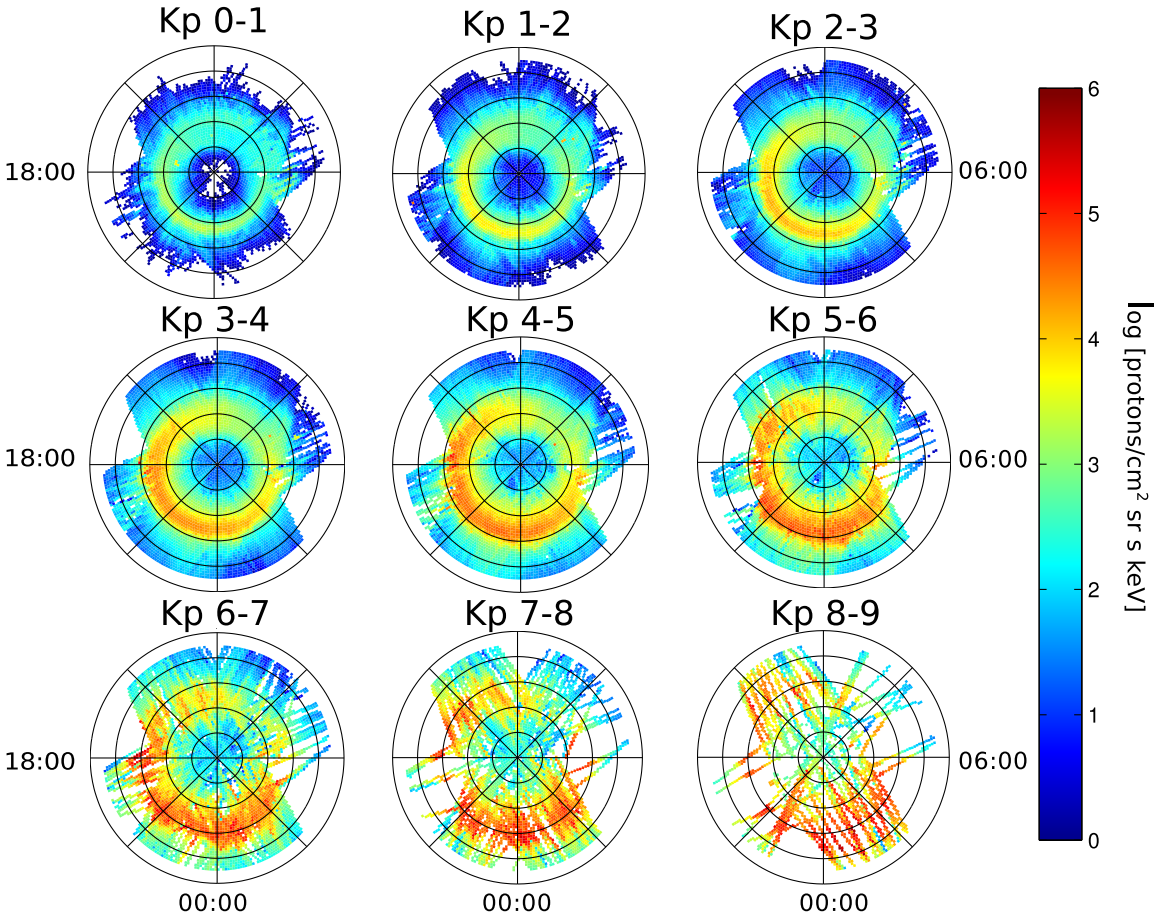

Figure 4.23: The flux of mirroring protons (90° detector) with 30-80 keV energy from both hemispheres, sorted according to Kp. The upper row shows Kp 0-1, 1-2 and 2-3. The middle row shows Kp 3-4, 4-5 and 5-6. The bottom row shows Kp 6-7, 7-8 and 8-9. Noon is at the top of the plots, and dawn is to the right.

The Figures 4.22 and 4.23 show that we get a rather well defined oval around the pole where we have maximum intensity of particles in the 0° and 90° detectors. This is the isotropic zone. As expected, we see that the flux intensity varies with MLT, and with Kp. We can also see that the isotropic zone is wider for larger Kp, and that the equatorward isotropic boundary moves further equatorward with increasing Kp. To utilize this information for calibration, we determined the maximum flux for each 0.5 hours of MLT as a function of ILAT. We then determined the boundaries of the isotropic zone, which we defined to be at ±50% of maximum flux. We then found the mean fux inside the isotropic zone. We repeated the procedure for both detectors, P1-P3, and all levels of Kp< 4. Panel a) of Figure 4.24 shows the ILAT for the boundaries of the isotropic zone for Kp 3-4 in blue lines, plotted vs MLT. The red line in the middle is the mid point between the two boundaries. In panel b) the mean differential flux in the P1

channel of the 0° detector between the two boundaries is plotted on logarithmic scale vs MLT. The error is the standard deviation of the mean. In panel c) the number of events between the boundaries is plotted.

Figure 4.24 shows that for Kp 3-4, there is a smooth variation of the latitude of the isotropic boundaries with MLT, and of the mean particle flux inside the boundaries with MLT, except for two spikes at MLT 08:30 and MLT 18:00. The spikes are both uniquely related to a small number of events as seen in panel c). The same is seen for all Kp intervals when similar spikes occur.

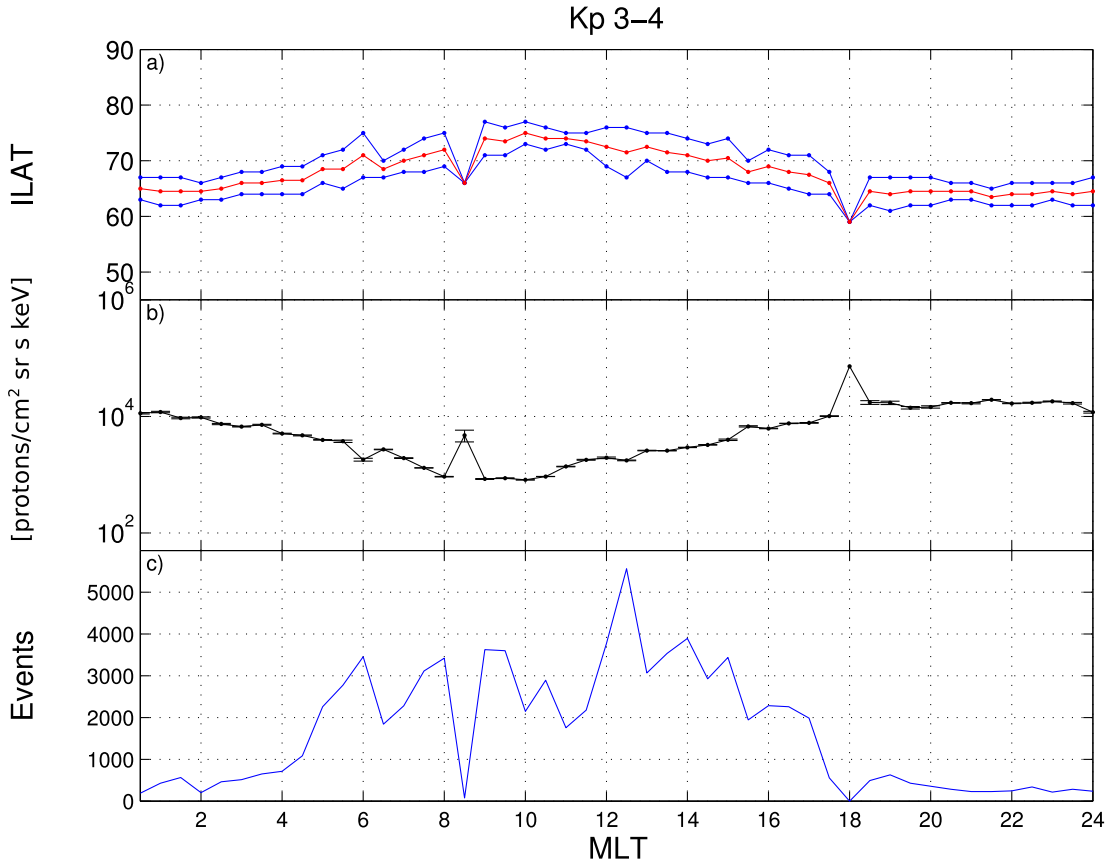

Figure 4.24: Based on data for Kp 3-4, panel a) shows the location of the equatorward and poleward boundaries for the precipitation zone (blue lines). For every 0.5 hour interval of MLT, the maximum intensity of precipitating protons is found. The boundaries are defined as the latitude where the intensity of the precipitation is 50% of the maximum intensity. Plotted in red is the mid point between the boundaries. Panel b) shows the mean differential flux in P1 between the two boundaries, and the errorbars show the standard deviation. Panel c) shows the number of events between the two boundaries. Note that the peaks found at MLT 8:30 and 18:00 in panels a) and b) are coinciding with few events at these local times for this Kp interval in panel c).

For Kp 0-1 and 1-2, isolated events of high flux at low latitudes causes the equatorward boundary of the isotropic zone to be identified at too low latitudes. When this happens, the number of events between the boundaries can get large. The contribution of flux equatorward of the oval, however, is not correspondingly large, and the mean flux between the boundaries is thus seen to drop for such MLT. The problem is illustrated in Figure 4.25 at MLT 19:30, marked Spike 2. Between MLT 08:30-09:00 there is also a spike due to a few events of extra high flux, marked Spike 1. The location of the spikes in Figure 4.25 are marked in Figure 4.26, also as Spike 1 and Spike 2. For all other MLT,

the curves in Figure 4.25 and equivalent plots for Kp< 4 vary more or less smoothly. For Kp> 4, the variation of the boundaries and mean flux are more noisy due to less statistics. For Kp> 6 we find that the curves are not smooth at all as can be seen in Figure 4.27. For the purpose of calibrating the MEPED detectors, we find that only data when Kp< 4 can be used with this method.

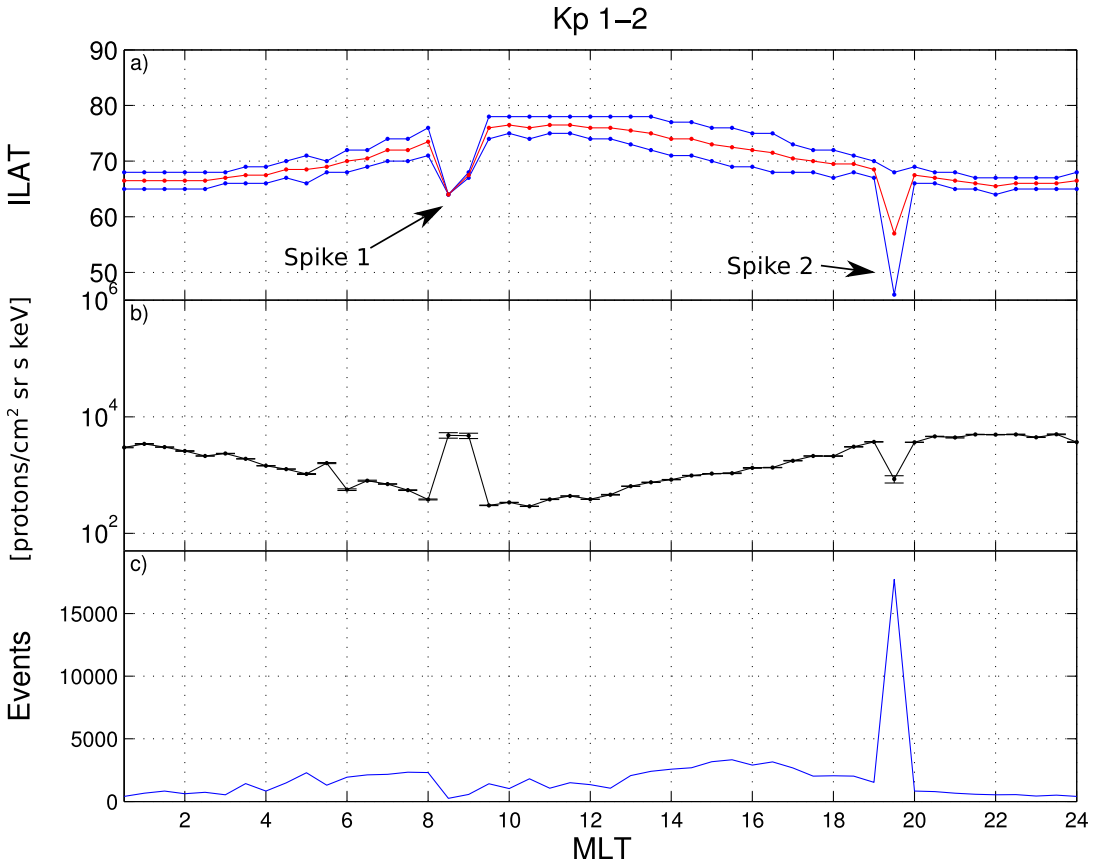

Figure 4.25: Based on data for Kp 1-2, panel a) shows the location of the equatorward and poleward boundaries for the precipitation zone (blue lines). For every 0.5 hour interval of MLT, the maximum intensity of precipitating protons is found. The boundaries are defined as the latitude where the intensity of the precipitation is 50% of the maximum intensity. Plotted in red is the mid point between the boundaries. Panel b) shows the mean differential flux in P1 between the two boundaries, and the errorbars show the standard deviation. Panel c) shows the number of events between the two boundaries. For MLT 08:30-09:00 and MLT 19:30 two spikes can be seen resulting from a wrong identification of auroral equatorward boundary.

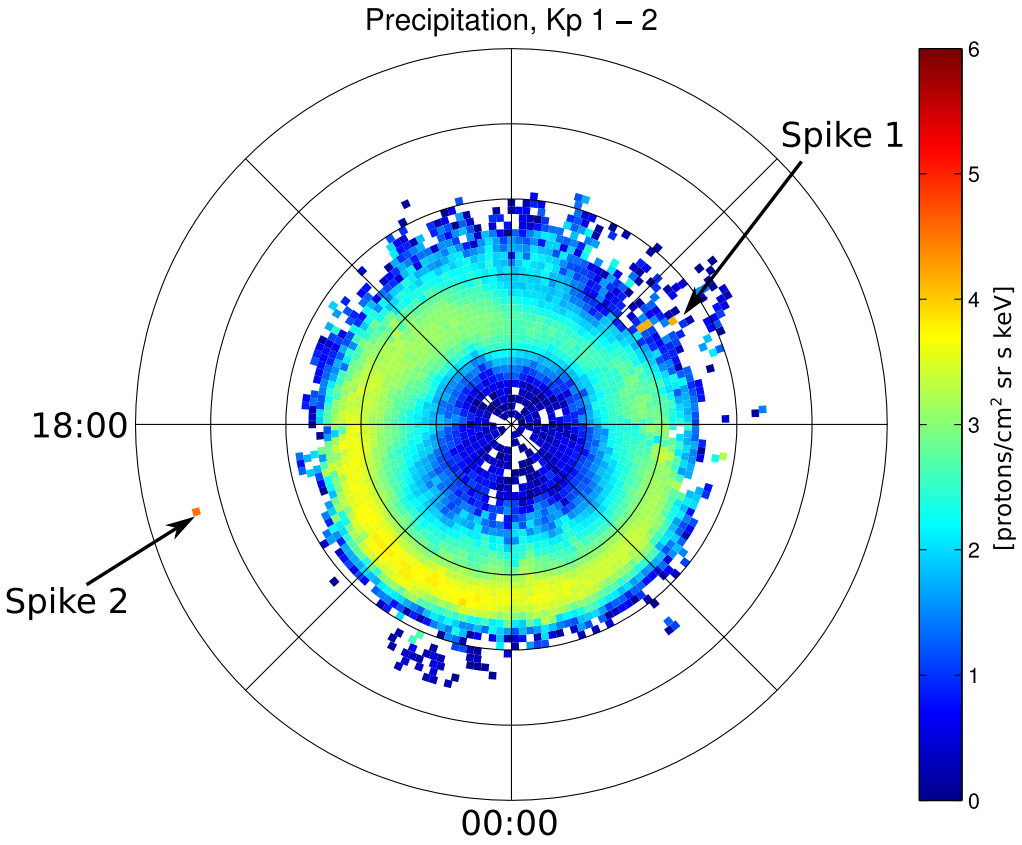

Figure 4.26: Rebinned particle data from the 0° detector for Kp 1-2 from both hemispheres added together. The logarithmic flux of 30-80 keV precipitating protons is plotted using a color scale. The spikes observed in Figure 4.25 are marked with arrows at 19:30 MLT and 09:00 MLT. Both these high intensities occur outside the main precipitation oval.

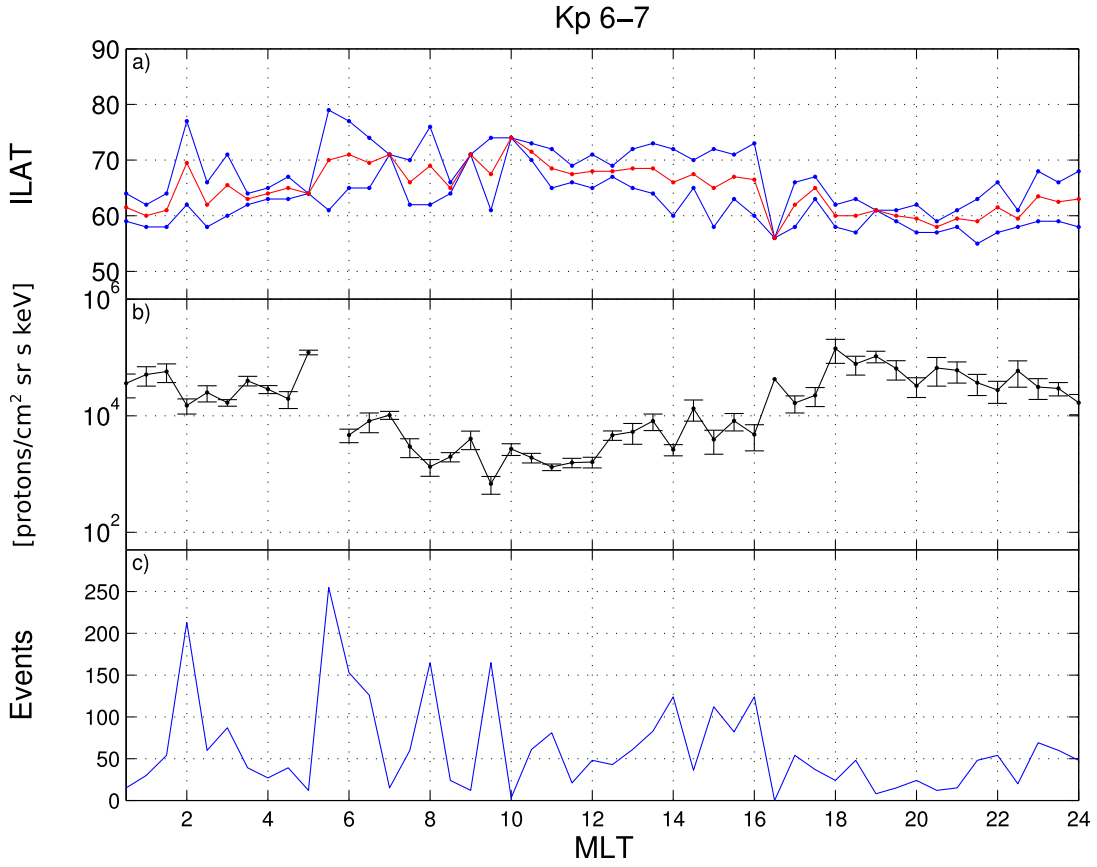

Figure 4.27: Based on data for Kp 6-7, panel a) shows the location of the equatorward and poleward boundaries for the precipitation zone (blue lines). For every 0.5 hour interval of MLT, the maximum intensity of precipitating protons is found. The boundaries are defined as the latitude where the intensity of the precipitation is 50% of the maximum intensity. Plotted in red is the mid point between the boundaries. Panel b) shows the mean differential flux in P1 between the two boundaries, and the errorbars show the standard deviation. Panel c) shows the number of events between the two boundaries. The boundaries in panel a) are noisy, most likely due to the varying number of events at different MLT seen in panel c). At some MLT, the number of events is close to zero.

4.3.2 How the Calibration is Performed

When the MLT dependence of the isotropic zone, and the mean flux inside the boundaries defining the isotropic zone, are found, we can exploit this to calibrate satellites that sample different MLT sectors. When calibrating a degraded satellite, we still require that the new satellite has to be undamaged. Thus, we can only calibrate old satellites in the years when a new satellite is launched. For consistency, we use a 150 day period when utilizing this calibration technique as well.

After the launch of a new satellite, we rebin the 150 first days of data from the new satellite, and the same period of data from the old satellite, in an MLT vs ILAT grid like was done to make the statistical maps shown in Figure 4.22 and 4.23. Every satellite pass through all sectors are checked vs Kp, and only data when Kp$<$ 4 are used. The general idea of the further procedure is as follows: For each level of Kp,

1. We locate at which 0.5 hour MLT the data from the old satellite are binned.
2. We locate at which 0.5 hour MLT the data from the new satellite are binned.
3. At every MLT, we find the ratio of the statistical mean flux to the statistical mean flux at all MLT where the new satellite is measuring.
4. For the given Kp level and MLT, we find the latitude of the isotropic zone in the statistical maps.
5. In the statistically found isotropic zone, we calculate the mean flux (for the entire 150 days period) measured at each 0.5 hour MLT by the old satellite, and by the new satellite.
6. For every 0.5 hour MLT for the old satellite, we multiply the mean flux measured by the old satellite by the ratios found in point 3. This gives us an estimate of what the old satellite *are assumed to measure* had it been located in the same MLT as the new satellite. We call this estimated flux the *equivalent flux* of the old satellite in the MLT of the new satellite.
7. We use the equivalent flux of the old satellite to construct energy spectra, which we compare with energy spectra for the new satellite for every MLT where the new satellite is located.

Figures 4.28 and 4.29 explains the procedure visually. In both figures, the statistical variation of the mean flux in the P1 channel for protons with pitch-angles of 0° is plotted vs MLT as a blue dashed curve. The flux is plotted on logarithmic scale. To represent the new satellite in this plot, we have used NOAA 17 in 2002. The 150 first days of data from the evening sector in the Northern Hemisphere is sorted according to Kp, binned by MLT, and averaged over the whole period. Next, the same is done with data from NOAA 16 in the night sector of the Northern Hemisphere, which is the old satellite. The mean flux measured by NOAA 17 in the statistical isotropic zone is plotted as red circles, the mean flux measured by NOAA 16 is plotted as black circles.

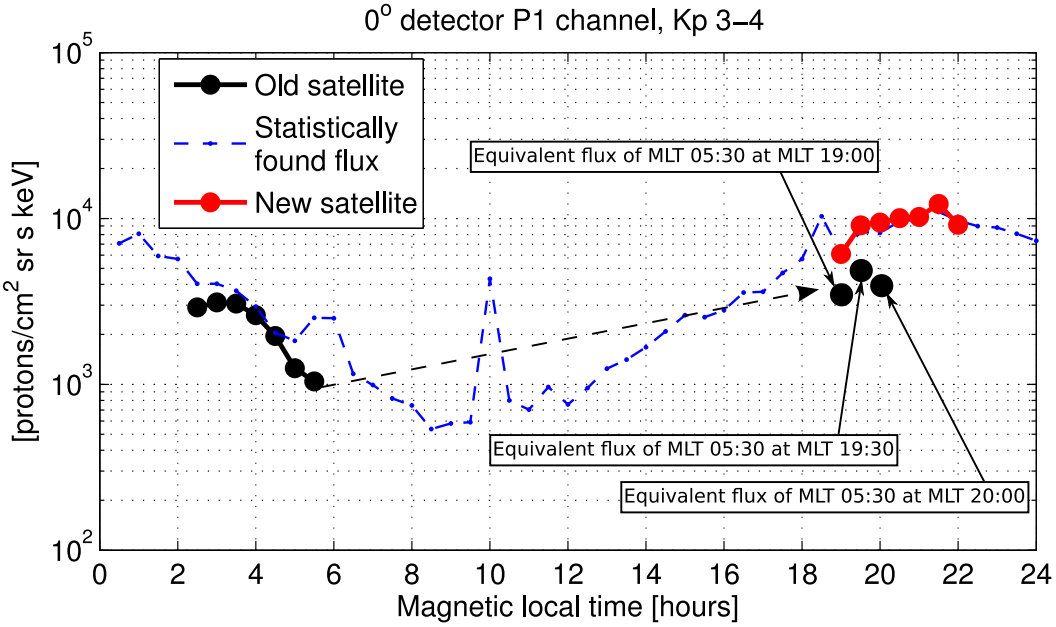

Figure 4.28: The statistical variation of the mean flux measured by the P1 channel in the 0° detector is plotted vs MLT as a blue dashed curve. The mean flux measured by NOAA 17 (new satellite) is plotted as red circles. The mean flux measured by NOAA 16 (old satellite) is plotted as black circles. For every MLT where there are measurements by the old satellite, we find the equivalent flux of the old satellite in all MLT where the new satellite is located. The dashed arrow is there to illustrate that the measurements from the old satellite at MLT 05:30 is used, and that we have found what the old satellite *are assumed to measure* at the MLT where the new satellite is located. We have also marked the equivalent flux found for the measurements obtained at MLT 05:30, at MLT 19:00, 19:30, and 20:00. The method would continue to find the equivalent flux at MLT 20:30, 21:00, ..., 22:00.

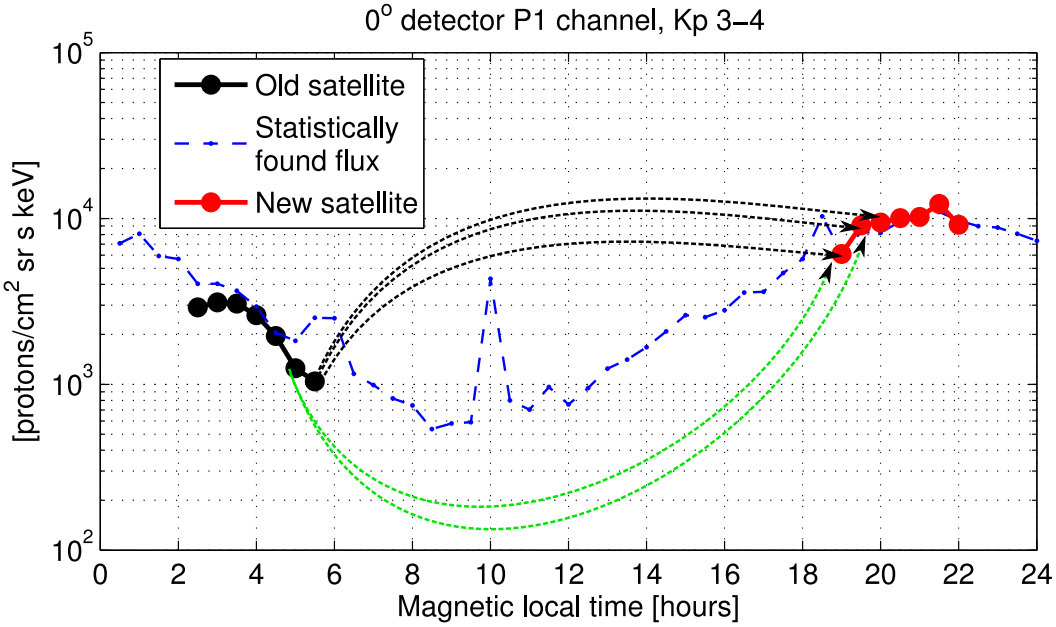

Figure 4.29: The statistical variation of the mean flux measured by the P1 channel in the 0° detector is plotted vs MLT as a blue dashed curve. The mean flux measured by NOAA 17 (new satellite) is plotted as red circles. The mean flux measured by NOAA 16 (old satellite) is plotted as black circles. We compare every measurement from the old satellite with *all* measurements from the new satellite. The black dashed arrows indicate the first three comparisons for MLT 05:30. The green dashed arrows indicate the two first comparisons for MLT 05:00.

All the NOAA satellites have in common that they cover several MLT during a day, and a larger area in the Southern Hemisphere than in the Northern Hemisphere. Over the 150 days, data from each satellite cover from 3-6 hours of MLT. When we bin the data in bins of 0.5 hours of MLT, this means that the old and the new satellite will have data in 6-12 of the 48 bins, but not the same bins. In the Figures 4.28 and 4.29, where only data from the northern evening and night sectors are used, the data both satellites are binned in 7 MLT-bins of 0.5 hours. This allows for $7 * 7 = 49$ comparisons of energy spectra with data from only one sector (from each satellite). When we do comparisons of all four sectors, for Kp 0-1, 1-2, 2-3, and 3-4, we get over a thousand comparisons in one calibration. Because our maps of average particle fluxes are constructed based on data from both hemispheres, we assumed that the location and intensity of the maximum particle flux was approximately the same in both hemispheres for a given Kp, and therefore valid to use as a representation of both hemispheres. The method could only provide α factors for P1 and P2. The results from the calibration will no be presented.

Results Using Method 2

Tables 4.4, 4.5, 4.6, 4.7, and 4.8 present the results found for NOAA 15, NOAA 16, NOAA 17, NOAA 18 and MetOp 02.

Table 4.4: α factors for NOAA 15. P1 and P2 are presented for both detectors. 150 days of data are used, and approximately 1500 integral energy spectra are compared every year. In 2007, over 3000 spectra are compared.

Calibration of NOAA 15				
Year	P1 0°	P2 0°	P1 90°	P2 90°
2001	1.3 ± 0.3	1.4 ± 0.3	1.5 ± 0.3	1.5 ± 0.3
2002	1.6 ± 0.4	1.7 ± 0.4	1.9 ± 0.4	1.9 ± 0.5
2005	2.2 ± 0.5	2.1 ± 0.4	2.6 ± 0.6	2.3 ± 0.5
2007	2.2 ± 0.9	2.1 ± 0.7	2.6 ± 1.0	2.2 ± 0.8
2009	2.1 ± 0.7	2.1 ± 0.5	2.5 ± 0.6	2.5 ± 0.7

Table 4.5: α factors for NOAA 16. P1 and P2 are presented for both detectors. 150 days of data are used, and approximately 1500 integral energy spectra are compared every year. In 2007, over 3000 spectra are compared.

Calibration of NOAA 16				
Year	P1 0°	P2 0°	P1 90°	P2 90°
2002	1.2 ± 0.6	1.2 ± 0.3	1.2 ± 0.6	1.4 ± 0.4
2005	1.6 ± 0.4	1.6 ± 0.4	1.9 ± 0.4	1.9 ± 0.4
2007	1.7 ± 1.1	1.7 ± 0.6	1.8 ± 1.0	1.8 ± 0.8
2009	1.6 ± 0.5	1.7 ± 0.4	1.9 ± 0.4	1.9 ± 0.5

Table 4.6: α factors for NOAA 17. P1 and P2 are presented for both detectors. 150 days of data are used, and approximately 1500 integral energy spectra are compared every year. In 2007, over 3000 spectra are compared.

Calibration of NOAA 17				
Year	P1 0°	P2 0°	P1 90°	P2 90°
2005	1.3 ± 0.3	1.5 ± 0.3	1.5 ± 0.4	1.7 ± 0.4
2007	1.4 ± 0.9	1.5 ± 0.5	1.6 ± 0.7	1.7 ± 0.6
2009	1.5 ± 0.4	1.6 ± 0.3	1.7 ± 0.4	1.8 ± 0.4

Table 4.7: α factors for NOAA 18. P1 and P2 are presented for both detectors. 150 days of data are used, and approximately 1500 integral energy spectra are compared every year. In 2007, over 3000 spectra are compared.

Calibration of NOAA 18				
Year	P1 0°	P2 0°	P1 90°	P2 90°
2007	-	1.1 ± 0.3	1.0 ± 0.5	1.1 ± 0.4
2009	1.0 ± 0.5	1.2 ± 0.2	1.1 ± 0.5	1.2 ± 0.2

Table 4.8: α factors for MetOp 02. P1 and P2 are presented for both detectors. 150 days of data are used, and approximately 1500 integral energy spectra are compared.

Calibration of MetOp 02				
Year	P1 0°	P2 0°	P1 90°	P2 90°
2009	1.1 ± 0.6	1.1 ± 0.2	1.2 ± 0.6	1.2 ± 0.2

We see that the results produced with this calibration method have large MAD. In this method, time variation is not the main source of error. The fluxes used in the integral spectra are averaged over 150 days, 0.5 MLT and approximately 3-5° invariant latitude, depending on Kp. The statistical maps of precipitating and mirroring particles ensure that we select only data well inside the region of maximum flux measured by both detectors. The most uncertain part of this analysis is the assumption that we can find the equivalent flux at one MLT, based on the average measurements at some other MLT. Figure 4.25 and 4.24 are examples of the statistical situation for the location and intensity of precipitating particles (0° detector) at Kp 1-2 and 3-4, respectively. The mean flux within the two boundaries that were identified is seen to vary with MLT in panels b) of both figures. The shape of the curves are reminiscent of a sine curve. However, our data coverage is to sparse to make the curves completely smooth. Also, we have not fitted the curves to a function. When we find the equivalent flux, we first calculate the ratio between fluxes in the two MLTs in question based on our statistical maps, then we multiply the flux measured by the old satellite by the ratio we found. Since the mean flux does not vary smoothly, the ratio between the flux at two MLTs can be largely influenced by small variations in the curve. Especially if one of the MLTs happen to be where a spike on the curve is found.

Chapter 5

Comparison With Previous Work

The α factors presented by *Asikainen and Mursula* [2011] and *Asikainen et al.* [2012] are found by fits to the yearly α factors they could obtain. Such fits have not been done in this thesis due to limited time. In the *Asikainen and Mursula* [2011] article, plots were presented showing the yearly α factors for NOAA 15-18 and MetOp 02, including the fits that were made to the data. In the *Asikainen et al.* [2012] article only the factors inferred from the improved fits are presented. We will therefore discuss our α factors in the light of the conjunction-based yearly α factors by *Asikainen and Mursula* [2011] where this is possible, and by the improved fits by *Asikainen et al.* [2012]. We remark that the yearly conjunction-based α factors and errors are read off the plots presented visually.

5.1 Method 1

5.1.1 NOAA 16 in 2005

Asikainen and Mursula [2011] identified 50 conjunctions between NOAA 18 and NOAA 16. In Figure 8 in their article presenting NOAA 16, we assume that the conjunctions with NOAA 18 are presented as the α factor in 2006, since there is no α factor plotted for 2005. In Table 5.1 we have therefore presented the α factors for the 0° detector and the 90° detector, using the factors for 2006 found by *Asikainen and Mursula* [2011] and *Asikainen et al.* [2012].

The α factor found in this thesis shows a larger degradation in the P1 channel, and a smaller degradation in the P2 and P3 channel than found by *Asikainen and Mursula* [2011] and *Asikainen et al.* [2012], which is reasonable, because the degradation is expected to be most severe at the lowest energies. However, we also find a smaller MAD with our method than *Asikainen and Mursula* [2011] found with the conjunction-based method, especially for the higher energy channels, which may indicate that our results are more accurate. However, it is difficult to judge what is the true value for the α factor. The difference in the method used in this part of this thesis, and the method used by *Asikainen and Mursula* [2011] gives different sources of error to the different results. In general, we do not know where the conjunctions occurred or what the particle

population looked like during the conjunctions. If the energy spectra of the identified conjunctions look different from conjunction to conjunction, this would make the MAD of the α distribution large.

The α factors presented by *Asikainen et al.* [2012] are presented without error. The factors are based on fits to the data from the *Asikainen and Mursula* [2011] article, but improved with the aid of the cumulative Ap index as described in Section 4.1.2. The new α factors are not radically different from the ones presented by *Asikainen and Mursula* [2011], with the exception of P3 which is larger in the *Asikainen et al.* [2012] article.

We find a decreasing α factor with increasing energy channels. Since the flux of particles drops off with increasing energy, we expect the higher energy channels to be less degraded than the lower energy channels. For NOAA 16, *Asikainen et al.* [2012] find the P3 and P2 channel of the 0° detector to be more degraded than the P1 channel.

Table 5.1: The α factors for the 0° detector and the 90° detector onboard NOAA 16 in 2005. We compare the α factors found in this thesis with the α factor found by *Asikainen and Mursula* [2011](referred to as AM2011) and *Asikainen et al.* [2012] (referred to as A2012).

α factors for NOAA 16 in 2005			
Energy Channel	This thesis	AM2011	A2012
P1 0°	1.8 ± 0.2	1.5 ± 0.25	1.53
P2 0°	1.3 ± 0.1	1.8 ± 0.4	1.75
P3 0°	1.3 ± 0.1	1.6 ± 0.5	1.79
P1 90°	2.0 ± 0.2	1.75 ± 0.25	1.83
P2 90°	1.8 ± 0.2	2.0 ± 0.4	2.02
P3 90°	1.2 ± 0.1	2.0 ± 0.7	1.64

For the 90° detector we also find a decreasing degradation with increasing energy channel. Our α factors have smaller MAD in P2 and P3 than the conjunction-based factors found by *Asikainen and Mursula* [2011]. As for the 0° detector, we find a larger α factor for P1, but smaller factors for P2 and P3 compared to *Asikainen and Mursula* [2011] and *Asikainen et al.* [2012]. We also note that we find a larger degradation of the P1 and P2 channel in the 90° detector, as is expected since the 90° detector is exposed to a larger radiation dose than the 0° detector. The P3 channels of the two detectors are approximately equally degraded in our calibration. *Asikainen and Mursula* [2011] find the 90° detector to be more degraded in all three channels, while *Asikainen et al.* [2012] find a larger degradation in P3 of the 0° detector compared to the 90° detector.

5.1.2 NOAA 17 in 2007

Asikainen and Mursula [2011] identified 17 conjunctions between NOAA 17 and MetOp 02. In Table 5.2 we present the α factors for the 0° detector and the 90° detector, using the factors for 2007 found by *Asikainen and Mursula* [2011] and *Asikainen et al.* [2012].

As for NOAA 16, our calibration gives a decreasing degradation for increasing energy

channels. The factors we find for the P1 channel in both detectors are approximately equal to factors found by *Asikainen and Mursula* [2011] and *Asikainen et al.* [2012].

Table 5.2: The α factors for the 0° detector and the 90° detector onboard NOAA 17 in 2007. We compare the α factors found in this thesis with the α factor found by *Asikainen and Mursula* [2011](referred to as AM2011) and *Asikainen et al.* [2012] (referred to as A2012).

α factors for NOAA 17 in 2007			
Energy Channel	This thesis	AM2011	A2012
P1 0°	1.4 ± 0.3	1.5 ± 0.25	1.52
P2 0°	1.2 ± 0.1	1.6 ± 0.1	1.52
P3 0°	1.2 ± 0.1	1.5 ± 0.5	1.56
P1 90°	1.7 ± 0.2	1.75 ± 0.25	1.73
P2 90°	1.3 ± 0.1	1.8 ± 0.2	1.84
P3 90°	1.2 ± 0.1	1.5 ± 0.6	1.49

5.1.3 NOAA 18 in 2009

Asikainen and Mursula [2011] identified zero conjunctions between NOAA 18 and NOAA 19. The only new satellite found to have conjunctions with NOAA 18 was MetOp 02 in 2007. The α factors are set to constant after 2007, and the factors presented for 2009 are thus based on conjunctions with MetOp 02, not NOAA 19. In Tables 5.3 we present the α factors for the 0° detector and the 90° detector, using the factors for 2009 found by *Asikainen and Mursula* [2011] and *Asikainen et al.* [2012]. In this thesis we could not determine the α factor for the P3 channel in the two detectors, and therefore we present only results for P1 and P2.

Since *Asikainen and Mursula* [2011] did not find any conjunctions between NOAA 19 and NOAA 18, it is difficult to compare our results directly. However, what we can see is that the degradation of NOAA 18 is not severe in 2009. The adjusted α factors by *Asikainen et al.* [2012] are only slightly larger than the *Asikainen and Mursula* [2011] factors for P1. For P2 the adjustment is a bit larger. Our calibration are closer to the factors of *Asikainen and Mursula* [2011] than the factors of *Asikainen et al.* [2012].

Table 5.3: The α factors for the 0° detector and the 90° detector onboard NOAA 18 in 2009. We compare the α factors found in this thesis with the α factor found by *Asikainen and Mursula* [2011](referred to as AM2011) and *Asikainen et al.* [2012] (referred to as A2012).

α factors for NOAA 18 in 2009			
Energy Channel	This thesis	AM2011	A2012
P1 0°	1.02 ± 0.10	1.00	1.01
P2 0°	1.08 ± 0.05	1.06	1.17
P1 90°	1.05 ± 0.13	1.05	1.09
P290°	1.11 ± 0.03	1.19	1.25

5.2 Method 2

We find a similarity in how our α factors evolve over time when we compare them to the α factors by *Asikainen et al.* [2012]. Figure 5.1 show the P1 and P2 channels of the 0° detector onboard NOAA 15. The blue squares are α factors found in this thesis and presented in Table 4.4. The black crosses are α factors presented by *Asikainen et al.* [2012]. Our α factors are lower than the *Asikainen et al.* [2012] factors, except in 2009. For all satellites and both detectors, we find similar results. Our α factors and the α factors by *Asikainen et al.* [2012] follow a similar evolution with time, sometimes below and sometimes above. The *Asikainen et al.* [2012] factors are always found within the MAD of our α factors.

Our method of comparing satellites in the same MLT deviates from the trend in some cases. Figure 5.2 shows this for NOAA 16. The blue squares are α factors found in this thesis and presented in Table 4.5. The black crosses are α factors presented by *Asikainen et al.* [2012]. The red circle shows the α factors calculated for P1 and P2 with comparing NOAA 16 and NOAA 18 in the same MLT in 2005. In P1, this method gives a larger degradation, and a smaller degradation in P2. in the 90° detector of NOAA 16 however, the two methods produce quite similar α factors. For NOAA 17 and NOAA 18, the two methods give similar results for α in the P1 channel of both detector. In P2, the same-MLT-method gives a significantly smaller value for α.

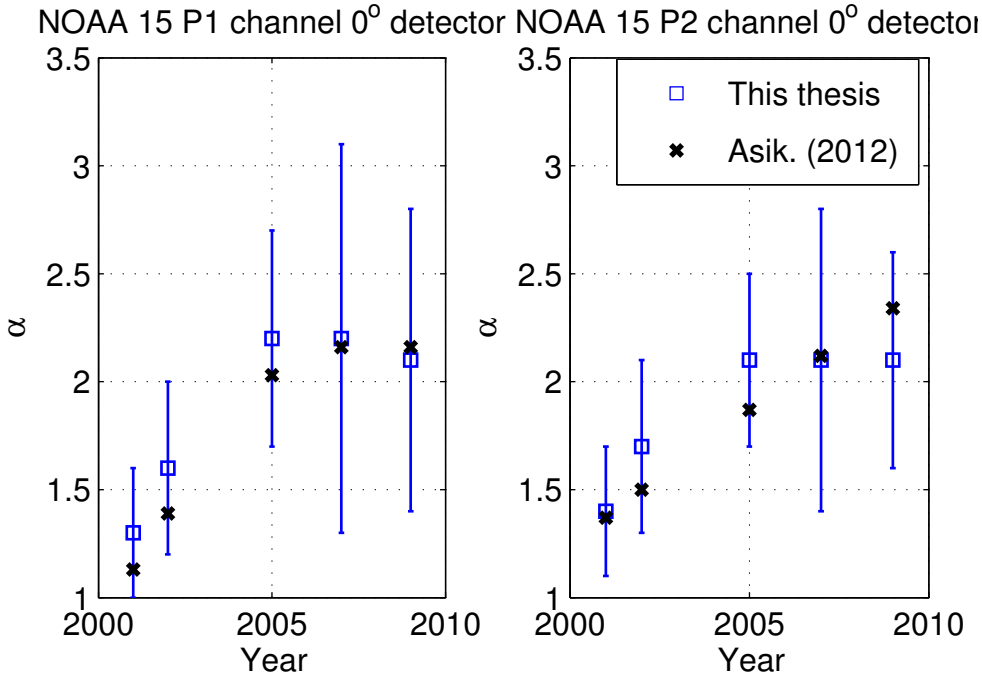

Figure 5.1: Time evolution for the α factors of the P1 and P2 channel in the 0° detector onboard NOAA 15. P1 is shown to the left, and P2 to the right. The blue squares are the α factors found in this thesis with the method that compares satellites in different MLT sectors. The black crosses are α factors for the same years as presented by *Asikainen et al.* [2012]. Note that α factors are presented by *Asikainen et al.* [2012] without error. However, the presented factors are derived from a curve fitted to α factors with error in the same range as the error shown in our results.

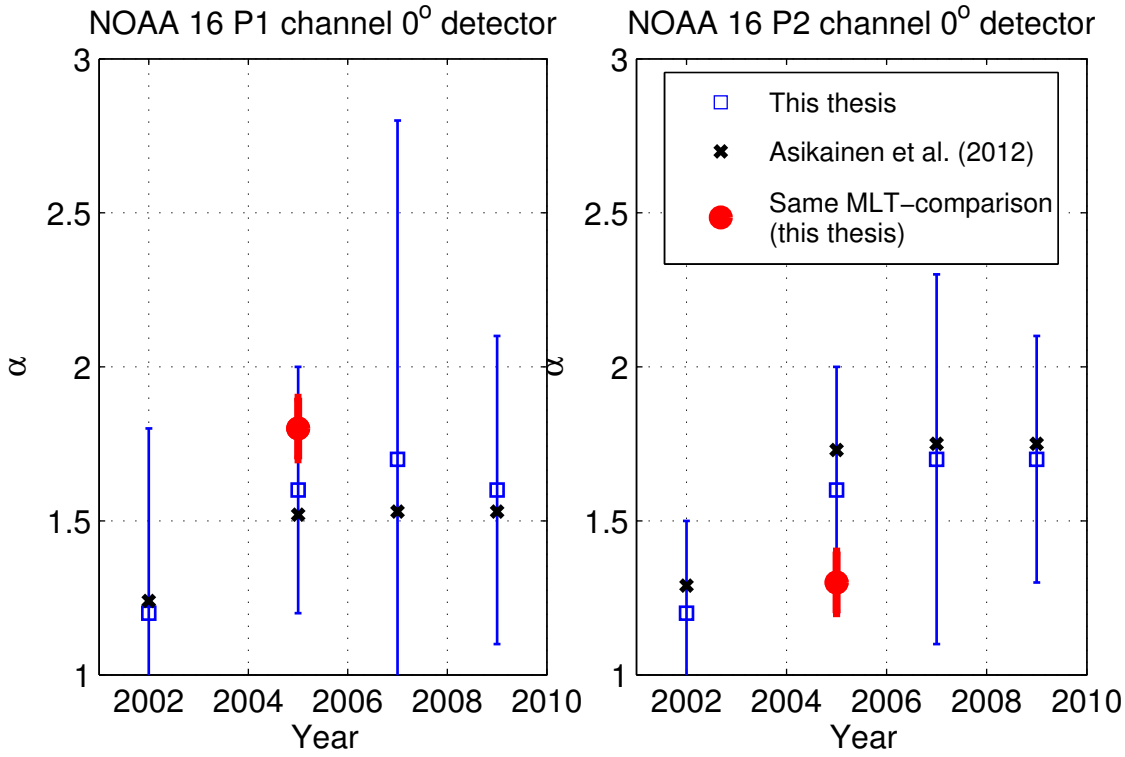

Figure 5.2: Time evolution for the α factors of the P1 and P2 channel in the 0° detector onboard NOAA 16. P1 is shown to the left, and P2 to the right. The blue squares are the α factors found in this thesis with the method that compares satellites in different MLT sectors. The black crosses are α factors for the same years as presented by *Asikainen et al.* [2012]. The red filled circle is the α factor found by use of the method that compares satellites in the same MLT. Note that α factors are presented by *Asikainen et al.* [2012] without error. However, the presented factors are derived from a curve fitted to α factors with error in the same range as the error shown in our results.

Chapter 6

Summary and Conclusions

Our main goal with this thesis was to develop a statistical method for calibrating the proton dataset obtained by the MEPED instrument onboard the polar orbiting NOAA satellites. We restricted the task to only focus on the newer satellites having the SEM-2 version of the instrument. This left us with six NOAA satellites, and approximately 15 years of data. Two methods were developed, and a short summary of the results is given here.

6.1 Calibration of Satellites at the Same MLT

A method for calibration at the same MLT was used to calibrate NOAA 16 in 2005, NOAA 17 in 2007 and NOAA 18 in 2009. For these satellites, a new satellite was launched into approximately the same MLT sector in these years. 150 days of data were used in all three cases, and fluxes were averaged over one day and 5° invariant latitude.

We found that the daily mean flux was probably not sufficient to average out temporal fluctuations in the particle population at middle and high latitudes. This was reflected in large MAD of the α distribution at these latitudes. Since substorms can occur on time scales of less than the satellite orbital period of $\sim$100 minutes, a substorm could influence the daily average energy measured by one of the satellites and not the other. In such a case, we will not get a "true" comparison of the average flux at the latitude where the substorm occurred because the substorm was missed by one of the satellites. When the old satellite measures a larger flux than the new satellite, the energy thresholds of the detector onboard the old satellite would appear to have decreased, and α is found to be less than 1.

The true degradation of the detectors is the same everywhere, regardless of ILAT and MLT. A substantial challenge lies in identifying conditions during which the degradation can be determined most accurately. *Asikainen and Mursula* [2011] required that the two satellites should be close in space and time when the comparison was made. This was to ensure that both satellites were exposed to the same level of radiation so that the energy spectra that were being compared were actually from the same particle population. With our statistical method, we do not require that the satellites have to be close in time.

However, we still require that the satellites have to be exposed to the same average level of radiation. The only location where our method ensures that the two satellites are subjected to the same average particle flux is where the particle fluxes are high. When the fluxes are high they are not as severely influenced by locally enhanced particle populations seen by only one of the satellites, especially since we average the flux in invariant latitude intervals of 5° width.

In this part of the analysis we did not discriminate between different levels of activity. However, we know that the region of maximum fluxes expand and move equatorward with increasing levels of activity. The region where the comparison of energy spectra can be done with the largest confidence will therefore move from day to day according to the level of activity. Since the most common activity level is quiet to moderately disturbed [*Rangarajan and Iyemori*, 1997], the average location of the maximum will be rather constant through a period of 150 days. We find that in the quiet year 2009, the intervals with the lowest MAD are situated at higher latitudes than in 2007 and 2005. This shows that we can not pick a fixed invariant latitude interval always, but have to identify the interval with lowest MAD from sector to sector and from year to year.

The α factors we find with this method are more in accordance with our expectation for the degradation of the detectors than the results presented by *Asikainen and Mursula* [2011] and *Asikainen et al.* [2012]. We find a decreasing degradation with increasing energy channel, which sounds reasonable. The lowest energy channels will experience the highest flux and therefore be more degraded.

6.2 Calibration of Satellites at Different MLTs

A method for calibration at different MLTs was used to calibrate NOAA 15-18 and MetOp 02 in every year when a new satellite was launched. When developing this method, we had to construct maps of the average flux of energetic protons as a function of ILAT and MLT. To do this, we rebinned the first year of data from every new satellite. The data were also sorted according to the Kp index. For every Kp, we found the boundaries for the maximum flux region in invariant latitude as a function of MLT. Between these boundaries, we calculated the statistical average flux as measured by both detectors. We could then determine the ratio of measured flux between any two magnetic local times. This ratio was used to calculate how large flux the old satellite would have measured had it been located in the same MLT as the new satellite. When we found the equivalent flux of the old satellite in the MLT of the new satellite, we compared energy spectra for the two satellites. The flux was thus averaged over 150 days, over a few degrees of invariant latitude (depending on where the boundaries of maximum flux were for the given Kp), and over 0.5 hours MLT.

The use of this method gives α factors with a large MAD. However, the factors evolve with time very similarly to the factors by *Asikainen et al.* [2012]. *Asikainen and Mursula* [2011] found the average error of all conjunction based α factors to be about 20%. Our method gives an average error in the α factors of about 30%. We see that the year 2006/2007 when MetOp 02 is new gives an extra large MAD. We also found

that in this year, almost twice as many comparisons of energy spectra could be made compared to every other year. The reason could be that MetOp 02 and NOAA 17 cover a relatively large area of the Southern Hemisphere in the calibration period. Figure 4.18 showed the coverage of MetOp 02 and NOAA 17 in one day in 2006. During the 150 day period, the two satellites provides measurements in many of the MLT bins. However, the passes through the Southern Hemisphere are quite far apart, and the statistics could therefore be unsatisfactory for each bin.

6.3 Concluding Remarks

The results obtained by calibration by two different methods developed in this thesis show that more work has to be done to determine the degradation of the MEPED instrument more robustly. In the three years where we can use both calibration methods, the two methods give very similar results, and the α factor obtained with method 1 is within the error for the α factor obtained with method 2 in the same year. The error of the results from method 2 is quite large. However, the α factors calculated by *Asikainen and Mursula* [2011] has errorbars in the same range. Several suggestions for improvements to the calibration methods are listed in the next chapter.

Chapter 7

Future Work

More work is required to establish reliable α factors for the MEPED proton detectors on-board NOAA satellites. In this chapter we suggest some improvements to our methods, and some new methods that could be utilized.

7.1 Improvements to the Statistical Methods

In the method for comparing satellites in the same MLT sector, we divide the data into bins that are 5° wide in latitude. This division is quite crude. A width of 1° could improve the method. This will better accommodate the fact that the region around maximum precipitation swells and shrinks with the level of activity. It will also improve the statistics with up to 5 times as many comparisons of energy spectra. However, smaller bins may also increase the error, since we get fewer samples in each box. We could also improve the method by averaging over more than one day. This will decrease the number of comparisons we can make, but average out more of the time variability in particle fluxes seen at middle and high latitudes, and thus maybe lower the MAD at these latitudes. In this way we might be able to rely on more of the data and α factors found. Another approach that could be tested is to identify the location where the daily average flux has the smallest standard deviation, and calculate the α factors here. This would most likely be inside the isotropic zone. This approach would also take into account the motion of the isotropic boundaries.

Our second method can also be improved. To get better statistical maps, the data can be sorted into larger intervals of Kp. In this way we could get a better estimation of the mean particle flux as a function of MLT, and also better identify the boundaries for the maximum particle flux region as a function of MLT. It might also be useful to fit the mean flux to a mathematical function for finding the equivalent flux in a different MLT, instead of the approximation now used with the ratio of the statistical flux in the two different MLT. The method should also be improved to include calibration of the P3 channel.

The methods developed in this thesis, and by *Asikainen et al.* [2012] are all limited to calibration in the launch years of new satellites. However, satellites are not launched

every year. When there are several years between each time we can estimate an α factor, the temporal evolution of the factors become more uncertain. It would therefore be interesting to further develop the second method from this thesis to test if it could be used for calibration only by comparing the old satellite to the statistical maps. This would in principle enable the calculation of a yearly α factor, and better estimate the temporal evolution. However, it would have to be tested.

7.2 Events That Could Confirm α factors

Conditions that are ideal for calibration are when all (or several) of the satellites are exposed to the same level of radiation, even though they may not be close in time and space. At least two such types of events are known to exist.

1. During solar energetic particle (SEP) events the polar cap is exposed to isotropic energetic precipitation. During such events, all satellites could be calibrated using the newest satellite inside the polar cap regardless of their location in MLT.

2. During a geomagnetic storm, a Storm Time Equatorial Belt (STEB) of trapped particles is observed for NOAA satellite's altitudes around geomagnetic equator [*Søraas et al.*, 2003]. The STEB is approximately symmetric during the recovery phase of the storm. When such a symmetry exists, a calibration could be done for satellites at different MLT at low latitudes.

A SEP or STEB event could give an additional point in the time evolution of α. The α factors obtained through different methods may provide more confidence about the true degradation of the detector.

Bibliography

Asikainen, T., and K. Mursula (2011), Recalibration of the long-term NOAA/MEPED energetic proton measurements, *Journal of Atmospheric and Solar-Terrestrial Physics*, *73*(2-3), 335–347, doi:10.1016/j.jastp.2009.12.011.

Asikainen, T., V. Maliniemi, and K. Mursula (2010), Modeling the contributions of ring, tail, and magnetopause currents to the corrected Dst index, *Journal of Geophysical Research*, *115*(A12), A12,203, doi:10.1029/2010JA015774.

Asikainen, T., K. Mursula, and V. Maliniemi (2012), Correction of detector noise and recalibration of NOAA/MEPED energetic proton fluxes, *Journal of Geophysical Research*, *117*(A9), 1–16, doi:10.1029/2012JA017593.

Axford, W. I. (1985), The solar wind, *Solar Physics*, *100*(1-2), 575–586, doi:10.1007/BF00158446.

Baker, D. N., et al. (2013), A Long-Lived Relativistic Electron Storage Ring Embedded in Earth's Outer Van Allen Belt, *Science*, *186*, doi:10.1126/science.1233518.

Balch, C., D. Biesecker, L. Combs, M. Crown, K. Doggett, J. Kunches, and H. Singer (2004), Halloween space weather storms of 2003, *Tech. Rep. June*, National Oceanic and Atmospheric Administration, Boulder, Colorado.

Balogh, A., et al. (1999), The Solar Origin of Corotating Interaction Regions and their Formation in the Inner Heliosphere, *Tech. rep.*, Space Science Reviews.

Barnett, M. A. F. (1974), The early days of ionosphere research, *Journal of Atmospheric and Terrestrial Physics*, *36*, 2071–2078.

Baumjohann, W., and G. Paschmann (1990), Geometry of the near-Earth plasma sheet, *Journal of Geophysical Research*, *95*(A7), 10,707–10,710, doi:10.1029/JA095iA07p10707.

Baumjohann, W., and R. A. Treumann (1996), *Basic Space Plasma Physics*, Imperial College Press.

Berry, P. A. M. (1987), Periodicities in the Sunspot Cycle, *Vistas in Astronomy*, *30*, 97–108.

Birkeland, K. (1908), *The Norwegian Aurora Polaris Expedition 1902-1903*, Aschehoug & Co, London, New York.

Borovsky, J. E., and M. H. Denton (2006), Differences between CME-driven storms and CIR-driven storms, *Journal of Geophysical Research*, *111*(A7), A07S08, doi:10.1029/2005JA011447.

Bourdarie, S., and M. Xapsos (2008), The Near-Earth Space Radiation Environment, *IEEE Transactions on Nuclear Science*, *55*(4), 1810–1832, doi:10.1109/TNS.2008.2001409.

Breen, A. R., W. A. Coles, R. Grail, M. T. Klinglesmith, P. J. Moran, C. A. Varley, and P. J. S. Williams (1997), Eiscat measurements of interaction regions inthe solar wind, *Advances in Space Research*, *20*(I), 6–9.

Carpenter, D. L. (1963), Whistler Evidence of a Knee' in the Magnetospheric Ionization Density Profile, *Journal of Geophysical Research*, *68*(6), 1675–1682.

Carrington, R. (1859), Description of a Singular Appearance in the Sun on September 1, 1859, *Monthly Notices of the Royal Astronomical Society*, *20*, 13–15.

Chapell, C. R. (1972), Recent Satellite Measurements of the Morphology and Dynamics of the Plasmasphere, *Reviews of Geophysics and Space Physics*, *10*(4), 951–979.

Chen, M., M. Schulz, and L. R. Lyons (1997), Modeling of Ring Current Formation and Decay: A Review, in *Magnetic Storms, Geophys. Monogr. Ser. vol. 98*, edited by B. T. Tsurutani, W. D. Gonzalez, Y. Kamide, and J. K. Arbollo, pp. 173–186, American Geophysical Union, Washington D.C., doi:10.1029/GM098p0173.

Codrescu, M. V., T. J. Fuller-Rowell, R. G. Roble, and D. S. Evans (1997), Medium energy particle precipitation influences on the mesosphere and lower thermosphere, *Journal of Geophysical Research*, *102*(A9), 19,977, doi:10.1029/97JA01728.

Cutnell, J. D., and K. W. Johnson (2013), *Introduction to Physics*, 9 ed., John Wiley & Sons, Inc.

Daae, M., P. Espy, H. Nesse Tyssøy, D. Newnham, J. Stadsnes, and F. Søraas (2012), The effect of energetic electron precipitation on middle mesospheric night-time ozone during and after a moderate geomagnetic storm, *Geophysical Research Letters*, *39*(21), n/a–n/a, doi:10.1029/2012GL053787.

Daly, E. (1994), The radiation belts, *Radiation Physics and Chemistry*, *43*(1-2), 1–17, doi:10.1016/0969-806X(94)90198-8.

Darrouzet, F., and J. De Keyser (2012), The dynamics of the plasmasphere: Recent results, *Journal of Atmospheric and Solar-Terrestrial Physics*, pp. 1–8, doi:10.1016/j.jastp.2012.07.004.

Davis, G. (2007), History of the NOAA satellite program, *Journal of Applied Remote Sensing*, *1*(1), 012,504, doi:10.1117/1.2642347.

Doe, R. A., M. B. Moldwin, and M. Mendillo (1992), Plasmapause Morphology Determined From an Empirical, *Journal of Geophysical Research*, *97*(A2), 1151–1156.

Domingo, V., B. Fleck, and A. I. Poland (1995), The soho mission: an overview, *Solar Physics*, *162*(1-2), 1–37.

Dungey, J. (1961), Interplanetary Magnetic Field And Auroral Zones, *Physical Review Letters*, *6*(2), 47.

Ebert, R. W., D. J. McComas, H. a. Elliott, R. J. Forsyth, and J. T. Gosling (2009), Bulk properties of the slow and fast solar wind and interplanetary coronal mass ejections measured by Ulysses: Three polar orbits of observations, *Journal of Geophysical Research*, *114*, A01,109, doi:10.1029/2008JA013631.

Elphinstone, R. D. (1996), What ia a Global Auroral Substorm?, *Reviews of Geophysics*, *34*, 169–232.

Escoubet, C. P., R. Schmidt, and M. L. Goldstein (1997), Cluster – science and mission overview, *Space Science Reviews*, *79*(1-2), 11–32.

Evans, D. S., and M. S. Greer (2004), Polar Orbiting Environmental Satellite Space Environment Monitor - 2: Instrument Descriptions and Archive Data Documentation, *Tech. Rep. January*, Natl. Atmos. and Oceanic Admin., Space Environ. Cent., Boulder, Colorado.

Feminella, F., and M. Storini (1997), Large-scale dynamical phenomena during solar activity cycles, *Astronomy and Astrophyics*, *322*, 311–319.

Fleck, B., D. Müller, S. Haugan, L. S. Duarte, and T. Siili (2006), 10 Years of SOHO, *ESA bulletin*, *126*.

Galand, M., and D. S. Evans (2000), Radiation Damage of the Proton MEPED Detector on POES (TIROS / NOAA) Satellites, *Tech. Rep. 456*.

Ganguli, G., M. Reynolds, and M. Liemohn (2000), The plasmasphere and advances in plasmaspheric research, *Journal of Atmospheric and Solar-Terrestrial Physics*, *62*(17-18), 1647–1657, doi:10.1016/S1364-6826(00)00117-6.

Gonzalez, W. D., J. a. Joselyn, Y. Kamide, H. W. Kroehl, G. Rostoker, B. T. Tsurutani, and V. M. Vasyliunas (1994), What is a geomagnetic storm?, *Journal of Geophysical Research*, *99*(A4), 5771, doi:10.1029/93JA02867.

Gosling, J. T. (1993), The solar flare myth, *Journal of Atmospheric and Solar-Terrestrial Physics*, *98*(93).

Gringauz, K. I. (1963), The structure of the ionized gas envelope of earth from direct measurements in the u.s.s.r. of local charged particle concentrations*, *Planetary Space Science*, *11*, 281–296.

Hardy, D. A., M. S. Gussenhoven, and E. Holeman (1985), A statistical model of auroral electron precipitation, *Journal of Geophysical Research*, *90*(A5), 4229, doi:10.1029/JA090iA05p04229.

Hardy, D. A., M. S. Gussenhoven, and D. Brautigam (1989), A statistical model of auroral ion precipitation, *Journal of Geophysical Research*, *94*(88), 370–392.

Harten, R., and K. Clark (1995), The Design Features of the GGS Wind and Polar Spacecraft, *Space Science Reviews*, *71*, 23–40.

Hauge, R., and F. Søraas (1975), Precipitation of gt 115 keV Protons In the Evening Forenoon Sectors in Relation to the Magnetic Activity, *Planet Space Sci*, *23*(1973), 1141–1154.

Heber, B., T. Sanderson, and M. Zhang (1999), Corotating interaction regions, *Advances in Space Research*, *23*(3), 567–579, doi:10.1016/S0273-1177(99)80013-1.

Hudson, H., B. Haisch, and K. T. Strong (1995), Comment on "The solar flare myth" by J. T. Gosling, *Journal of Geophysical Research*, *100*(94), 3473–3477.

Hughes, W. J. (1995), The Magnetopause, Magnetotail, and Magnetic Reconnection, in *Introduction to Space Physics*, edited by M. G. Kievelson and C. T. Russell, 1 ed., chap. 9, pp. 227–285, Cambridge University Press, New York.

Hundhausen, A. J. (1995), The Solar Wind, in *Introduction to Space Physics*, edited by M. G. Kivelson and C. T. Russel, 1 ed., chap. 4, pp. 91–128, Cambridge University Press, New York.

Kamide, Y., et al. (1997), Magnetic Storms: Current Understanding and Outstanding Questions, in *Magnetic Storms, Geophys. Monogr. Ser. vol. 98*, edited by B. T. Tsurutani, W. D. Gonzalez, Y. Kamide, and J. K. Arballo, pp. 1–19, American Geophysical Union, Washington D.C.

Kane, R. P. (2006), Long-term variations of solar, interplanetary, geomagnetic indices and comic ray intensities—A brief tutorial, *Indian Journal of Radio & Space Physics*, *35*, 312–323.

Kelley, M. C. (2009), *The Earth's Ionosphere Plasma Physics and Electrodynamics*, 2 ed., Elsevier.

Kivelson, M. G. (1995), Physics of Space Plasmas, in *Introduction to Space Physics*, edited by M. G. Kivelson and C. T. Russell, 1 ed., chap. 2, pp. 27–55, Cambridge University Press, New York.

Li, X., D. N. Baker, S. G. Kanekal, M. Looper, and M. Temerin (2001), Long term measurements of radiation belts by SAMPEX and their variations, *Geophysical Research Letters*, *28*(20), 3827–3830, doi:10.1029/2001GL013586.

Lockwood, M., R. Stamper, and M. N. Wild (1999), A doubling of the Sun's coronal magnetic field during the past 100 years, *Nature*, *399*, 437–439.

Lundblad, J., K. Aarsnes, and F. Søraas (1979), Substorm Morphology of gt 100 keV Protons, *Planetary Space Science*, *27*, 841–865.

Mackay, H., T. Karpen, L. Ballester, B. Schmieder, and G. Aulanier (2010), Physics of Solar Prominences: II—Magnetic Structure and Dynamics, *Space Science Reviews*, *151*, 333–399, doi:10.1007/s11214-010-9628-0.

McPherron, R. L. (1979), Magnetospheric Substorms, *Reviews of Geophysics and Space Physics*, *17*(4), 657–681.

McPherron, R. L. (1995), Magnetospheric Dynamics, in *Introduction to Space Physics*, edited by M. Kievelson and C. T. Russell, 1 ed., chap. 13, pp. 400–457, Cambridge University Press, New York.

McPherron, R. L. (1997), The Role of Substorms in the Generation of Magnetic Storms, in *Magnetic Storms, Geophys. Monogr. Ser. vol. 98*, edited by B. T. Tsurutani, W. D. Gonzalez, Y. Kamide, and J. K. Arbollo, pp. 131–146, American Geophysical Union, Washington D.C.

Miyoshi, Y., A. Morioka, and H. Misawa (2000), Long term modulation of low altitude proton radiation belt by the Earth's atmosphere, *Geophysical Research Letters*, *27*(14), 2169–2172, doi:10.1029/1999GL003721.

Newell, P. T. (2004), Maps of precipitation by source region, binned by IMF, with inertial convection streamlines, *Journal of Geophysical Research*, *109*, A10,206, doi:10.1029/2004JA010499.

Newell, P. T., and J. W. Gjerloev (2012), SuperMAG-based partial ring current indices, *Journal of Geophysical Research*, *117*(A5), A05,215, doi:10.1029/2012JA017586.

Oksavik, K. (1998), HighLatitude Boundary Phenomena and Magnetospheriv Processes During the January 9-12 1997 CME Event: NOAA-12, Wind and Groundbased Observations, Ph.D. thesis.

Pedatella, N. M., and K. M. Larson (2010), Routine determination of the plasmapause based on COSMIC GPS total electron content observations of the midlatitude trough, *Journal of Geophysical Research*, *115*(A9), A09,301, doi:10.1029/2010JA015265.

Pinto, O., W. D. Gonzalez, I. R. C. A. Pinto, A. L. C. Gonzales, and O. Mendes (1992), The South Atlantic Magnetic Anomaly : three decades of research, *Journal of Atmospheric and Terrestrial Physics*, *54*(9), 1129–1134.

Priest, E. R. (1995), The Sun and its Magnetohydrodynamics, in *Introduction to Space Physics*, edited by M. G. Kivelson and C. T. Russell, 1 ed., chap. 3, pp. 58–89, Cambridge University Press, New York.

Raben, V. J., D. S. Evans, H. Sauer, S. Sahm, and M. Huynh (1995), TIROS/NOAA Satellite Space Environment Monitor Data Archive Documentation: 1995 Update, *Tech. Rep. February*, National Oceanic and Atmospheric Administration.

Rangarajan, G. K., and T. Iyemori (1997), Time variations of geomagnetic activity indices Kp and Ap: an update, *Annales Geophysicae*, *15*(10), 1271–1290.

Russell, C. T. (1986), Solar Wind Control of Magnetospheric Configuration, in *Solar Wind-Magnetosphere Coupling*, pp. 209–231.

Russell, C. T. (1993a), Magnetic Fields of the Terrestrial Planets, *Journal of Geophysical Research*, *98*, 18,681–18,695.

Russell, C. T. (1993b), Planetary magnetospheres, *Rep. Prog. Phys*, *56*, 687–732.

Ruzmaikin, A. (2001), Origin of sunspots., *Space Science Reviews*, *95*, 43–53.

Schrijver, C. J. (2009), Driving major solar flares and eruptions: A review, *Advances in Space Research*, *43*(5), 739–755, doi:10.1016/j.asr.2008.11.004.

Singh, a. K., S. Mishra, and S. K. Dohare (2010), Role of Earth's plasmasphere in coupling of upper atmosphere, *Journal of Physics: Conference Series*, *208*, 012,070, doi:10.1088/1742-6596/208/1/012070.

Solanki, S. K. (2003), Sunspots: An overview, *The Astronomy and Astrophysics Review*, *1769*, 153–286.

Søraas, F., K. Aarsnes, K. Oksavik, and D. S. Evans (2002), Ring current intensity estimated from low-altitude proton observations, *Journal of Geophysical Research*, *107*, 1–10.

Søraas, F., K. Oksavik, K. Aarsnes, D. S. Evans, and M. S. Greer (2003), Storm time equatorial belt – an "image" of RC behavior, *Geophysical Research Letters*, *30*(2), 22–25, doi:10.1029/2002GL015636.

Stern, D. P. (1984), Energetics of the magnetosphere, *Space Science Reviews*, *39*(1), 193–213, doi:10.1007/BF00173674.

Stix, M. (2002), Sunspots: What is interesting?, *Astronomische Nachrichten*, *323*, 178–185.

Stone, E. C., A. M. Frandsen, R. A. Mewaldt, E. R. Christian, D. Margolies, J. F. Ormes, and F. Snow (1998), The Advanced Composition Explorer, *Space Science Reviews*, *86*(1-4), 1–22, doi:10.1023/A:1005082526237.

Tsurutani, B. T., et al. (2006), Corotating solar wind streams and recurrent geomagnetic activity: A review, *Journal of Geophysical Research*, *111*(A7), A07S01, doi:10.1029/2005JA011273.

Tverskaya, L. V. (2010), Dynamics of the Earth's radiation belts, *Moscow University Physics Bulletin*, *65*(4), 246–251, doi:10.3103/S0027134910040028.

Tverskoy, B. A. (1971), Dynamics of the Radiation Belts of the Earth, *Tech. Rep. June*, NASA, Washington D.C.

Van Allen, J. A. (1966), Some General Aspects of Geomagnetic Trapped Radiation, in *Radiation Trapped in the Earth's Magnetic Field*, edited by B. M. McCormac, pp. 65–75, D. Reidel Publishing Company, Dordecht - Holland.

Vette, J. I. (1970), Summary of Particle Populations in the Magnetosphere, in *Particles and Fields in the Magnetosphere*, edited by B. M. McCormac, pp. 309–308, D. Reidel Publishing Company, Dordecht - Holland.

Waynick, A. H. (1974), Fifty years of the ionosphere. The early years-Experimental, *Journal of Atmospheric and Terrestrial Physics*, *36*, 2105–2111.

Webb, D. (2000), Coronal mass ejections: origins, evolution, and role in space weather, *IEEE Transactions on Plasma Science*, *28*(6), 1795–1806, doi:10.1109/27.902209.

Wüest, M., D. S. Evans, and R. V. S. Eds (2007), *Calibration of Particle Instruments in Space Physics*, ESA Publications Division.

Yoshimura, H. (2000), Mechanism of Cyclically Polarity Reversing Solar Magnetic Cycle as a Cosmic Dynamo, *J. Astrophys. Astr.*, *21*, 365–371.

Zou, H., Q. G. Zong, G. K. Parks, Z. Y. Pu, H. F. Chen, and L. Xie (2011), Response of high-energy protons of the inner radiation belt to large magnetic storms, *Journal of Geophysical Research*, *116*, doi:10.1029/2011JA016733.